Breaking Waves on Beaches

Paul Anthony Quinn

Doctor of Philosophy

The University of Edinburgh

1995

Abstract

A comprehensive experimental study has been carried out to measure the velocity field of waves breaking on two types of beach. The measurement technique of Particle Image Velocimetry (PIV) has been used throughout to measure the full-field, instantaneous velocity distributions. This technique is described in some detail with particular attention paid to the errors inherent when using PIV in this application. The first type of beach studied has a mild slope, typical of sandy beaches. PIV measurements have been carried out on 1:30 and 1:100 plane sloping beaches with monochromatic waves. The measured internal kinematics are compared to those predicted by the Boussinesq- and Serre-type wave models, with some good agreement. However, there are some significant differences in the near-surface region of the wave crest which tend to increase as the waves propagate up the beach. In addition to these theoretical comparisons, the Integral Properties of the waves on the 1:30 slope are calculated from the PIV measurements. The second type of beach examined is typical of a shingle beach. In addition to being steeper than the previous case, these beaches are also profiled, representing the shape of the beach formed under storm conditions. Two profiles have been modelled and three different monochromatic waves have been measured on each. The wave breaking processes are described and velocity measurements from each wave on both beaches are shown. Furthermore, a near-bed velocity comparison between the three waves at various positions along each beach has also been carried out in order to explain any potential on-shore and off-shore sediment motion.

Declaration

This thesis has been composed by myself and, except where stated, the work contained is my own.

Paul Quinn

Acknowledgments

This project was funded jointly by the Science and Engineering Research Council (SERC) under Grant No. GR/F/67945 and by the commission of the European Communities Directorate General for Science, Research and Development under contract Nos. MAST 0035C & EC MAST-II OCT 92 0027; their support is greatly appreciated.

I owe a great debt of thanks to my supervisors, Prof. Clive Greated & Dr. William Easson, for not only did they have enough faith in me to give me the job in the first place, but they have provided excellent support and advice throughout. Their understanding and approachable manner has been particularly appreciated.

I thank Prof. John Chaplin of City University and Gert Klopman of Delft Hydraulics for allowing their stream-function and Rienecker-Fenton models, respectively, to be used by this group. I thank Michele Drago of Snamprogetti SpA., Italy for providing the Boussinesq and Serre model comparisons shown in Section 4.2.3. Thanks must also go Marco Petti of The University of Florence for his help in conducting the experiments on the 1:100 beach and making my stays in Florence so enjoyable.

My colleagues and friends in the department have made my time in the Fluids Group most enjoyable. Particular thanks go to Tom Bruce and David Skyner, who made me feel very welcome when I first started and whose continuing advice and friendship I value very highly. I thank Frank Morris not only for his technical help around the department but mainly for putting up with me on two trips to Florence. I also offer my thanks to Jim King and the rest of the technicians for making the PIV illumination system, laser beam enclosure apparatus and the beaches.

Outside the department my friends, in particular, Richard Congreve, Louise McLennan, Sam Murrani & Mike Evans, have helped keep body and soul together and remind me that there is life outside the lab; I thank them very much.

I thank my parents for the financial support of my education (amongst many other things); if this thesis marks the end of my formal education, then it's the most expensive book they've ever bought: and its got a lousy plot. Seriously, many, many thanks for everything!

My greatest debt of gratitude goes to Theresa, my wife. As my PhD course was part-time, the vast majority of this thesis has been written in the evenings and at weekends. Her patience, understanding and support while writing-up has been exceptional.

Contents

Chapter 1

Introduction

1.1 General Background

Modern coastal engineering has now attained a greater profile throughout the world with an increasing awareness of environmental issues. The broadcasting on television news, year in and year out, of the devastating effect storms have on coastal towns and cities around the world has brought new public awareness to the problem. There is now a very strong worldwide research community dealing with these problems, with field and laboratory experiments as well as numerous numerical models derived with greater complexity and speed as computer technology increases.

The first thought of most people when you mention beaches is of their holidays. They often fail to recognise the importance of the beach as the first line of defence to the sea. Whilst recreational reasons are important to maintaining beaches, indeed for many parts of the world it provides the main source of income to the area through tourism, it is only one of many reasons to protect coastlines and prevent, where possible, erosion. The disposal of waste and the use of sea-water as a cooling medium for nuclear power stations through outflow pipes also causes concern; the sea kinematics in coastal areas being important for determining exactly where the effluent will end up, with effects on local wildlife, and possible pollution of a beach

used for human recreation. The importance of coastal engineering was ironically highlighted at the 23rd International Conference on Coastal Engineering in Venice, Italy, where on the first day of the conference the city was flooded. Figure 1.1 shows a photograph of St. Mark's Square on that day.

Figure 1.1: St. Mark's Square, Venice, 5th Oct. 1992.

1.2 Aim of Present Study

The general stimulus for this work is the ongoing requirement for detailed velocity measurements on all types of beach. Particle Image Velocimetry (PIV) is the only measurement system capable of providing a spatial velocity distribution at an instant; all other techniques give temporal distributions at a point. With these latter techniques, in order to build up a picture of the whole flow field, an experiment has to be performed many times with the measuring probe in an array of positions. This process is subject to error and turbulent phenomena

cannot be described accurately. Basco (1985) said *"A general understanding of the mechanisms and processes governing the mean flow field just after breaking remains one of the outstanding unsolved problems in fluid mechanics."* If one is to try and remedy this situation an accurate knowledge of the internal wave kinematics is required. In fact, the general hydrodynamics of waves approaching breaking on a beach is still not fully understood.

There is an increasing requirement for accurate morphodynamic models by coastal engineers for local authority or national government sponsored projects. Coastal engineering projects, eg. beach nourishment or sea-wall construction, are on such a large scale that mistakes are very expensive. At the present time there is no universally applicable model, essentially because individual elements to its design are not adequately understood. Neither wave nor sediment transport models have reached a stage where they can be used reliably in all but a handful of situations. It is the purpose of this project to provide accurate velocity data, using PIV, from two types of beach slope, in order to provide a sound basis for the validation of existing numerical wave models or the establishment of new ones.

The first beach type considered in this study, is typical of a sandy beach, ie. having a mild slope. There are a number of theoretical models for this type beach for two reasons; firstly the large number of sandy beaches around the world provides a practical stimulus and secondly, because of its relatively close approximation to waves propagating in a constant depth of water without any reflected wave components - a situation which is better understood. The aim of this study, with relation to mildly sloping beaches, is two-fold; firstly to provide detailed velocity data and compare the measured internal wave kinematics with values predicted by the Boussinesq- and Serre-type models and secondly to calculate the so called "Integral Properties", described in sections 1.3 & 4.5.3, from the spatial velocity distributions generated by PIV.

The second beach type considered is typical of a shingle beach. These have a steeper mean slope than sandy beaches due to the fact that they consist of larger diameter material; the increased friction between individual beach particles allows

a much steeper slope to be tolerated. This part of the study follows on from experiments carried out by Powell (1988) to measure the dynamic response of shingle beaches to wave attack in simulated storm conditions. Two of the resulting profiles have been modelled for velocity measurements in this study. The object of this part of the study is, once again, to provide accurate velocity data for waves breaking on this type of beach and examine the internal kinematics in order to explain the sediment movement which generated the particular beach profile.

1.3 Terminology and Definitions

There are several terms and definitions commonly used in coastal engineering which should be described before proceeding any further. These are mainly described in Basco (1985), Battjes (1988), Peregrine (1983) and Svendsen & Jonsson (1980).

Dealing first with the basic wave definitions, as shown in figure 1.2. Here the wave crest and trough are labelled, with the difference between them being the wave height, H. The elevation, η, is the difference between the height of the surface at a point and the Mean Water Level (MWL). The Still Water Level (SWL) is the height of the water when still, and this is not necessarily the same as the MWL.

If we consider the symmetrical wave in figure 1.2 approaching a uniformly sloping beach; as the wave runs into decreasing water depth it slows, shortens and steepens. This process is termed *shoaling*. The wave profile also adopts horizontal and vertical asymmetries during shoaling, as shown in figure 1.3.

As the wave continues to propagate towards the shoreline these asymmetries grow and the front face of the wave becomes increasingly steep. The breaking point is defined to be the point where the front face of the wave becomes vertical. In spilling breakers this is normally the point of maximum wave height, but this is not necessarily the case for plunging breakers. There are four distinct types

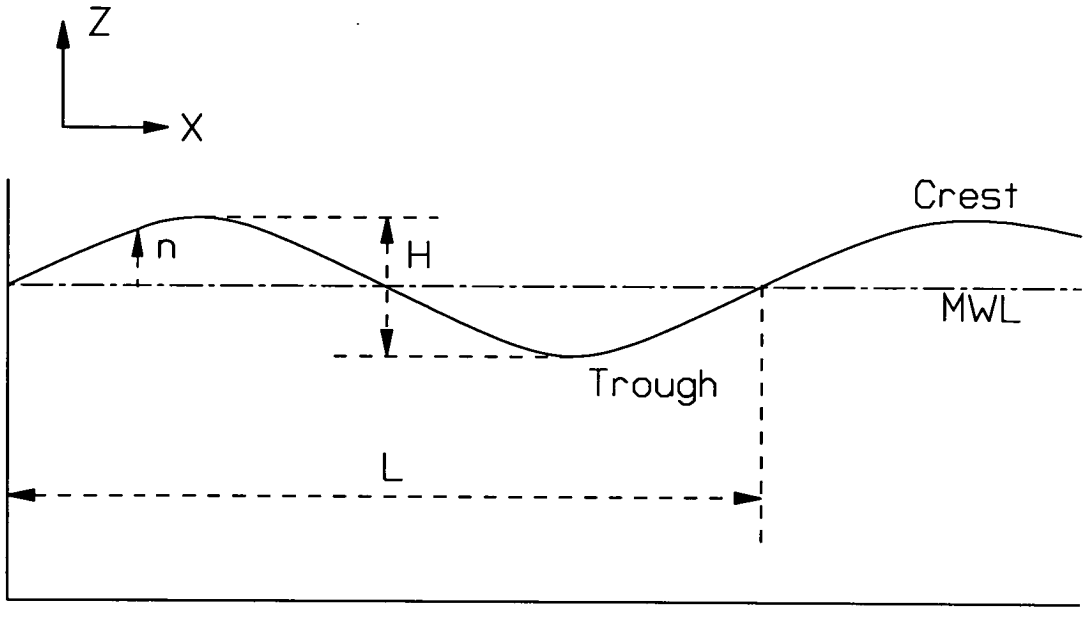

Figure 1.2: Definition diagram for wave parameters

of breaking wave, proposed by Galvin (1968, 1972), mainly based on physical appearance, they are:

1. *Spilling Breakers:* White water appears at the wave crest and spills down the front face, sometimes preceded by the projection of a small jet.

2. *Plunging Breakers:* Most of the wave's front overturns and a prominent jet falls near the base of the wave, causing a large splash, the so-called *splash-up.*

3. *Surging Breakers:* These are slightly turbulent standing waves against the beach face with turbulence generated from the bottom boundary shear, which is a function of bottom friction.

4. *Collapsing Breakers:* These are similar to plunging breakers except that the jet begins at a lower elevation than the crest.

The type of breaker formed on a beach depends mainly on the beach slope and wave steepness; where the wave steepness is defined to be the ratio of wave height

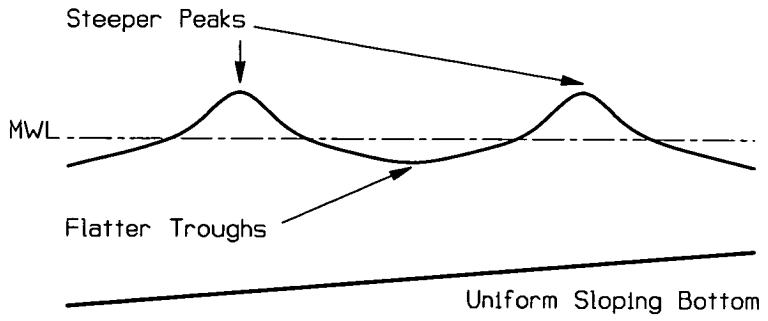

(A) Initial Vertical Asymmetry

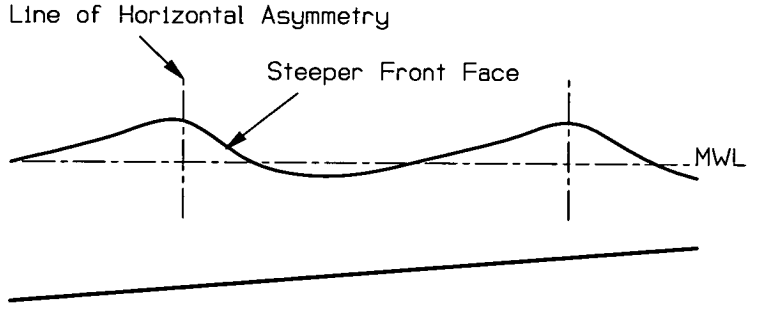

(B) Developing Horizontal Asymmetry

Figure 1.3: Horizontal and vertical asymmetries in shoaling waves

to wavelength, H/L. Battjes (1974) correlated these breaker types with the *surf similarity parameter*, ϵ, as defined in equation 1.1

$$\epsilon = \frac{\tan \alpha}{\sqrt{H/L_o}} \tag{1.1}$$

Where α is the slope of the beach and the subscript $_o$ denotes the deep water value. In general, on smooth impermeable slopes spilling breakers occur for $\epsilon < 0.4$. Plunging breakers occur when $0.4 < \epsilon < 2.0$. Above $\epsilon = 2.0$ surging breakers are evident. So for steep waves on a shallow sloping beach spilling breakers are formed and for flatter waves on a steep slope surging breakers are formed. Plunging breakers being the intermediate case.

The coastal region is also split up into different zones, the most commonly accepted

classification is that of Svendsen et al. (1978), subsequently used by Stive (1980) and Basco (1985) and shown in figure 1.4.

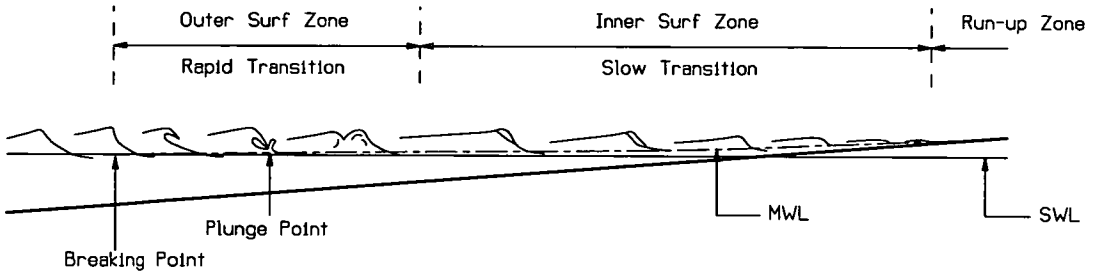

Figure 1.4: Definition diagram of the surf zone, following Svendsen et al. (1978)

The outer surf zone starts from the break point and finishes when the initial rapid transition in wave shape has finished, forming a propagating bore (Peregrine & Svendsen, 1978). The inner surf zone extends over the region where the wave profile is quasi-steady. As the bore approaches the water line it collapses and the motion continues in the form of a thin sheet of water that rushes up the slope to the point of maximum run-up, and then back again, the so-called *swash* (Battjes, 1988). The reduction of wave-height in the inner surf zone causes a rather large rise in the mean sea level, this is termed the *set-up*. Consequently the larger the incoming wave the larger the set-up. If one considers an irregular wave train breaking on a beach the mean water level will vary with a period much greater than the wave periods, this slow oscillation of the MWL is termed *surf beats* (Roelvink et al. (1992), Roelvink (1993)). Guza & Thornton, (1981) have measured wave set-up on a natural beach finding that the set-up at the shoreline was 0.17 times the significant wave height in deep water. The significant wave height H_s is the average height of the highest 1/3 of all the waves in a given spectrum. Adopting the approach of eg. Draper (1963) and Tucker (1963) one can define the root-mean-squared wave height, H_r, as the standard deviation of the wave elevation, σ_η, or the square root of the zeroth spectral moment, $\sqrt{m_o}$, as shown in equation 1.2. [1]

[1]After the experiments carried out on profiled beaches, discussed in detail in Chapter 5, the author was made aware of an alternative, and perhaps more widely used, definition of H_{rms}, ie. $H_{rms} = 2\sqrt{2}\sigma_\eta$. This has the effect of equating H_s with H.

$$H_r \equiv \sigma_\eta \equiv \sqrt{m_o} \tag{1.2}$$

If one adopts the assumption that the wave heights within the spectrum have a Rayleigh distribution (see, eg. Sarpkaya & Isaacson (1981)) then it can be shown that $H_s = 4\sigma_\eta$, hence the relations given in equation 1.3.

$$H_s = 4\sigma_\eta = 4\sqrt{m_o} = 4H_r \qquad\qquad H = \sqrt{2}H_r \tag{1.3}$$

In the experiments presented in this thesis only regular waves have been used and consequently there is no surf beat phenomenon. Outside the surf zone there is a small depression of the MWL, this is termed the *set-down*. One should deal with the wave set-up and set-down in some detail, this is because they both occur due to changes in the so-called *radiation stress*. The concept of the radiation stress was introduced in series of papers by Longuet-Higgins & Stewart (1960,1961,1962 & 1964) as the excess flux of momentum due to the waves, and has become one of the most important parameters in breaking wave dynamics. In determining the sediment concentration profile for the local sediment transport rate Dally & Dean (1984) said that *"The local gradient in the onshore radiation stress $\partial S_{xx}/\partial x$ appears to be the most important parameter in the problem because it drives the on/off-shore mean currents, and it is an indicator of the amount of sand placed in suspension by breaking induced turbulence."* Svendsen and Jonsson (1980) give a simple mathematical introduction to the radiation stress. With reference to figure 1.5 if one considers the mean momentum (M) and total pressure (P) forces over the depth (h) from MWL to the bottom, horizontal equilibrium yields equation 1.4

$$\frac{d(M+P)}{dx} + \rho g h \tan\alpha = 0 \tag{1.4}$$

where α is the uniform slope of the beach. Adopting an undisturbed depth (D), say the Still Water Level (SWL), from which the total height (h) is now comprised

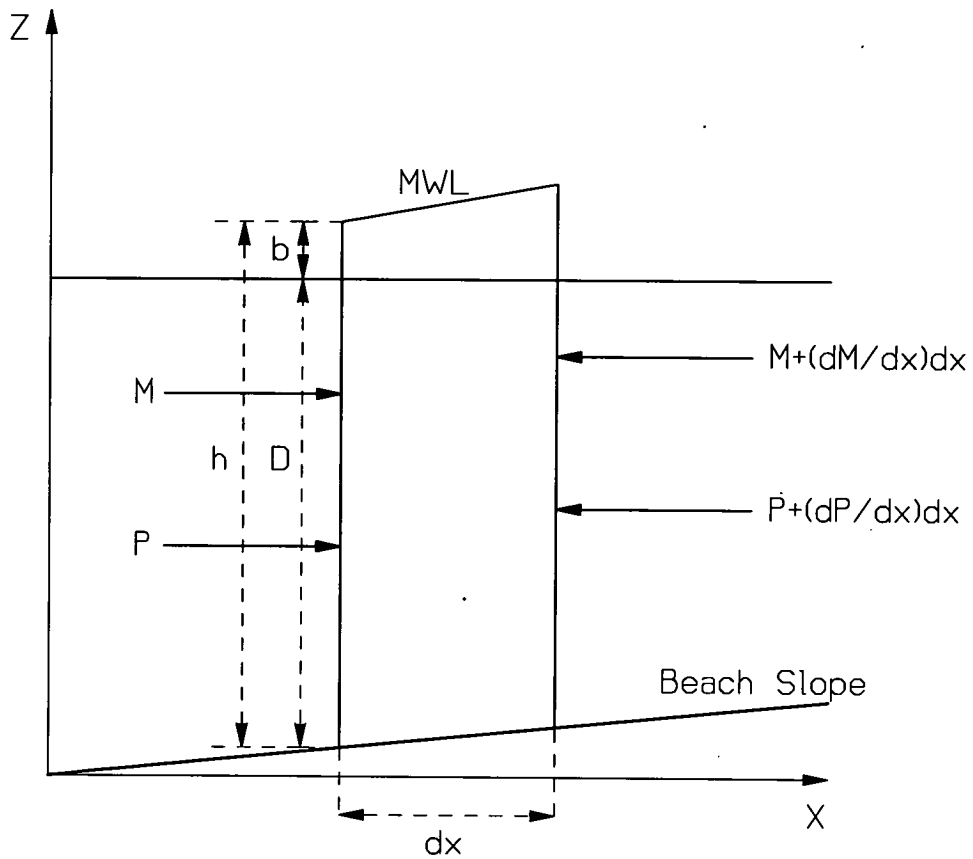

Figure 1.5: Forces with components perpendicular to the shoreline, following Svendsen & Jonsson (1980)

of the undisturbed depth (D) plus the elevation to MWL (b), the excess normal stress (σ_{xx}) is defined by equation 1.5.

$$\sigma_{xx} \equiv M + P - \frac{1}{2}\rho g h^2 \tag{1.5}$$

Replacing h with $D+b$ and $\tan\alpha$ with $-dD/dx$ in equation 1.4, yields equation 1.6,

$$\frac{dS_{xx}}{dx} = -\rho g h \frac{db}{dx} \tag{1.6}$$

because for normal incidence (wave fronts parallel to the bottom contours) σ_{xx} equals the radiation stress S_{xx}. From equation 1.6 one can see the dependence

on the elevation of the MWL and the hydrostatic pressure. The radiation stress increases outside the surf zone when a wave approaches the coast, but then must decrease after breaking (assuming uniform bed slope), giving the characteristic set-down outside the surf zone, and set-up inside the surf zone (Stive & Wind, 1982). The set-down tends to be small (about 3% of the local water depth h), and fairly unimportant, however the wave set-up can be as large as $\sim$ 30% of the local water depth, and consequently of more importance. In general the set-up is approximately one order of magnitude greater than the set-down.

The further development of the radiation stress is dealt with in some detail in section 4.5.3 where it is calculated for PIV experiments on shallow beaches.

1.4 Literature Review

Perhaps one of the most interesting aspects of fluid dynamics is that it encompasses a large number of different disciplines, including Mathematics, Physics and Engineering. Consequently there are a large number of publications in the field.

Dealing now with coastal engineering, Svendsen and Jonsson's (1980) book gives an excellent first introduction. Most of the definitions mentioned in section 1.3 are obtained from this book and it sets out in a clear way many of the fundamental points of coastal hydrodynamics. There are essentially two different aspects to coastal engineering research; hydrodynamics and morphodynamics, concerned with wave and/or current motion and beach or coast profile evolution respectively. These are of course interconnected, with both the beach topography and incident wave climate having an effect on each other, a factor which is demonstrated in this study. However, these two aspects are now considered separately.

One can further split hydrodynamics into two regions namely waves and currents. It is only waves that are considered in this study. One of the reasons for ignoring currents is that the experiments were carried out in a narrow wave flume, where

the wave motion is assumed to be two-dimensional, and the waves approach the beach normally. If the waves approached the beach from an angle a long-shore current is created which results in a horizontal circulation with water turning off-shore in what are termed *rip-currents*. These have a substantial effect on the local sea-bed, especially on sandy beaches, where the rip-current carves a channel for the returning water. Rip-currents also occur when waves approach the beach from a perpendicular direction, however the horizontal scale of their separation is large when one considers experiments in a relatively narrow wave flume. Cross-shore currents can be divided into three categories, namely short-period wave driven currents, tidal and wind driven currents. The latter two are long period effects and have little effect on individual waves. In the surf zone there is a net flow offshore near the bed, termed the *undertow*, which is a product of the wave action, and as such is considered in this study; see Hansen & Svendsen (1984) for a theoretical and experimental description of undertow. Longuet-Higgins (1983) describes theoretically and experimentally how the set-up helps to drive the undertow and proposes that the convergence of this current with the near-bed, on-shore directed current outside the breaker line, helps bar formation of the beach profile. Roelvink & Stive (1989) and Dean et al. (1992) also discuss bar generating processes. There have been a number of publications on currents and wave-current interaction, mainly for deep water scenarios, notably Kemp & Simons (1983), Swan (1990 & 1992), Thomas (1990) and Skyner & Easson (1992). Sakai et al. (1988) performed a series of experiments to measure the wave height of waves travelling onto a uniformly sloping beach in the presence of an opposing current to establish a wave breaking criterion for this case. Simons et al (1992) have performed a series of experiments with waves and currents crossing at right angles, and Hamm (1992) deals with waves travelling over a rip-current on a 1:30 sloping beach.

Waves can be split into two categories, deep water and shallow water waves. It is shallow water waves which are considered in this thesis. There are several review papers, notably Peregrine (1983), Basco (1985) and Battjes (1988) which give a good introduction to various aspects of wave motion in coastal regions

and have extensive reference sections. Dingemans (1994b) gives a comprehensive account of water wave propagation, paying particular attention to the Mild-Slope, Boussinesq-type and Korteweg-de Vries (KdV) equations. Dally et al. (1985) considers the wave height variation across the surf zone, this being important for considering the wave energy flux due to the rapid decrease in potential energy with reduction in wave height as the waves break. Thornton and Guza (1983) also deal with wave height transformation in the surf zone in a field study.

The most accurate velocity measurements made before PIV, used the technique of Laser Doppler Anemometry (LDA). This approach measures the temporal variation of the velocity at a point, with the inherent problems of wave repeatability already mentioned in section 1.2. Stive (1980), Mizuguchi (1986) and Griffiths et al. (1992) provide good examples of this type of experiment on plane sloping beaches. Although a relatively new technique, PIV has already established itself as a powerful fluid flow measuring system. Adrian (1991) gives a very good overview of the technique in various flow regimes. There are numerous papers dealing with water wave dynamics. Gray & Greated (1988) and Skyner et al. (1990) consider deep water breaking waves, and papers by Quinn et al. (1993), Powell et al. (1992) and by Greated et al. (1992a) deal with waves breaking on beaches. Greated et al. (1992b) gives a brief review of the technique as applied to coastal engineering processes.

The development of numerous numerical models of increasing complexity requires high quality experimental results for verification. PIV experimental results have been compared to a fully non-linear, time-stepping model developed by Dold & Peregrine (1986) for deep water breaking waves and have shown remarkable agreement (Skyner et al., 1990). Results from the experiments carried out on a 1:30 plane sloping beach, presented later, have been used in a comparison with Boussinesq- and Serre-type models carried out by Brocchini et al. (1992) with good agreement.

A number of numerical models have been developed; some of the more promising approaches have been examined by Klopman (1988). An extensive paper by Dean

& Perlin (1986) intercompares many wave theories with laboratory and field experimental data, but limits itself to near bottom kinematics. The first example of a Boundary Element system for computations of overturning waves was developed by Longuet-Higgins & Cokelet (1976) and several programs of this type have subsequently been developed, notably Vinge & Brevig (1981) and Dold & Peregrine (1984). Reinecker & Fenton (1981) developed a numerical model for steady water waves using a Fourier approximation; this has the benefit of making no analytical approximations and results, even for high waves, compare very well. Analytical methods, eg Stokes' expansions (Schwartz, 1974 and Cokelet, 1977) , and cnoidal (Fenton, 1979), only provide solutions in a limited domain of application, and still do not compare very well with experiment (Wang & Le Mehaute, 1980). There are several problems which have not been overcome in dealing numerically with waves on beaches. No theory can deal explicitly with the effect of backwash from the previous breaking wave. The boundary integral approach works well for singular breaking waves up to the point when the spout of the breaker touches the trough in front. Here the calculations break down due to the boundary, at the free surface, being broken, so for waves on beaches one can only look at cases where the waves before the incoming plunging breaker do not break. As the mean shingle beach slope is so steep ($\sim 1:7$) when compared to that of sandy beaches ($\sim 1:30$), the backwash component is very strong. This means that comparison with wave theories which ignore backwash is of little value. The theoretical aspects of this work are looked at in greater detail, in sections 4.5.3 & 4.2.2, when the integral properties for waves on shallow slopes are calculated, along with a comparison with Boussinesq- and Serre-type models.

It is the understanding of morphodynamics which is the underlying goal for coastal engineering, i.e. to accurately predict beach profile evolution due to erosion or accretion given the beach material characteristics and the local hydrodynamics. This situation is still a long way off, keeping the sea where you want the sea to be and the land where you want the land to be is notoriously difficult; one might, in a rather tongue-in-cheek manner, term this the Canute principle. At present the understanding of the separate areas of hydrodynamics and sediment transport is

not advanced enough to accurately deal with their interaction. The accuracy of PIV data should improve the knowledge of the hydrodynamics of waves on beaches and this should provide a better insight into sediment suspension and transport. An intercomparison of existing coastal profile models is given in Hedegaard et al. (1992). The two companion papers Southgate & Nairn (1993) and Nairn & Southgate (1993) deal with beach profile modelling, the former paper being involved with wave and current modelling and the latter concerning the sediment transport and beach profile evolution. Stive et al. (1992) looked at this problem with respect to shore nourishment, a common process in replenishing beaches affected by erosion. However, the size of material and where it is placed has a large effect on its success. This is generally an expensive engineering program and one has to make sure that the nourishment is not washed away in the next big storm. There are numerous papers dealing with different aspects of sediment transport. In the 23rd International Conference on Coastal engineering in 1992 there were 39 papers presented on the subject, notably Basco et al., Creed et al., Dean et al., Pedersen et al., Villaret & Latteux and van Rijn & Kroon.

Chapter 2

Particle Image Velocimetry (PIV)

2.1 Introduction

Although there are a number of institutions around the world who now use PIV as a matter of course, it is still relatively new when compared to Laser Doppler Anemometry (LDA), and as such warrants detailed description. This is given in sections 2.2 & 2.3. However, a brief introduction to the processes involved is considered useful.

PIV is a two-stage process exploiting fairly simple processes. The first stage is the photographic recording of the seeded flow field which is illuminated in a pulsatile manner. In this way multiple images of each of the seeding particles are recorded on the film. The second stage is the analysis of the PIV negative. Here a low-power Helium-Neon laser probes the negative point-by point across the imaged flow field. The multiple images of the seeding particles cause interference forming Young's fringes in the focal plane of a lens. The separation of these fringes is inversely proportional to the separation of the particles, and their orientation is perpendicular to the orientation of the particles. The measured displacement of the multiple images of the seeding particles yields the average velocity at that point, as the photographic magnification and the time interval between illumination pulses is known.

Although PIV is a relatively new technique it is nevertheless well documented, and has been applied in numerous fields. A good initial account is given in Adrian (1991) and Gray (1992). The book titled "*Flow Visualization and Image Analysis*" (1993), edited by Nieuwstadt, contains contributions from most of the main institutions working with PIV and associated flow measurement techniques. It covers both advances in the technique itself and many practical applications. Hydrodynamic applications have already been cited in section 1.4.

2.2 PIV Equipment

2.2.1 PIV Illumination System

The illumination of the flow in all of these experiments was provided by the scanning beam method. This has proved to be the best system for fluid flows of this size and velocity (Gray et al., 1991). The dependence on the size and typical velocity of a flow field is such that the combination of magnification and illumination period should cause the separation of the multiple images on the film to be between 30 and 300 μm. The scanning beam method has been used to measure flows up to 12.5 ms^{-1} in particle jets (McCluskey, 1992a). A diagram of the scanning beam illumination system developed and used for this study is shown in figure 2.1.

The beam from a continuous wave (CW) 15W Argon Ion laser enters the system at the bottom left of the box. A high-quality beam-steering mirror reflects the beam up through an achromatic telescope arrangement, collimating the beam, to hit the eight sided rotating mirror. This mirror, whose rotation speed can be adjusted very accurately in the range 12 - 250 rps, scans the laser beam along the parabolic mirror. The parabolic mirror reflects the beam up into the flow field in a vertical, collimated *pseudo* light-sheet. The parabolic mirror is constructed from a machined plate of Aluminium, 20mm thick. The reflecting surface is made by optically coating a thin strip of perspex and carefully sticking this to the parabolic

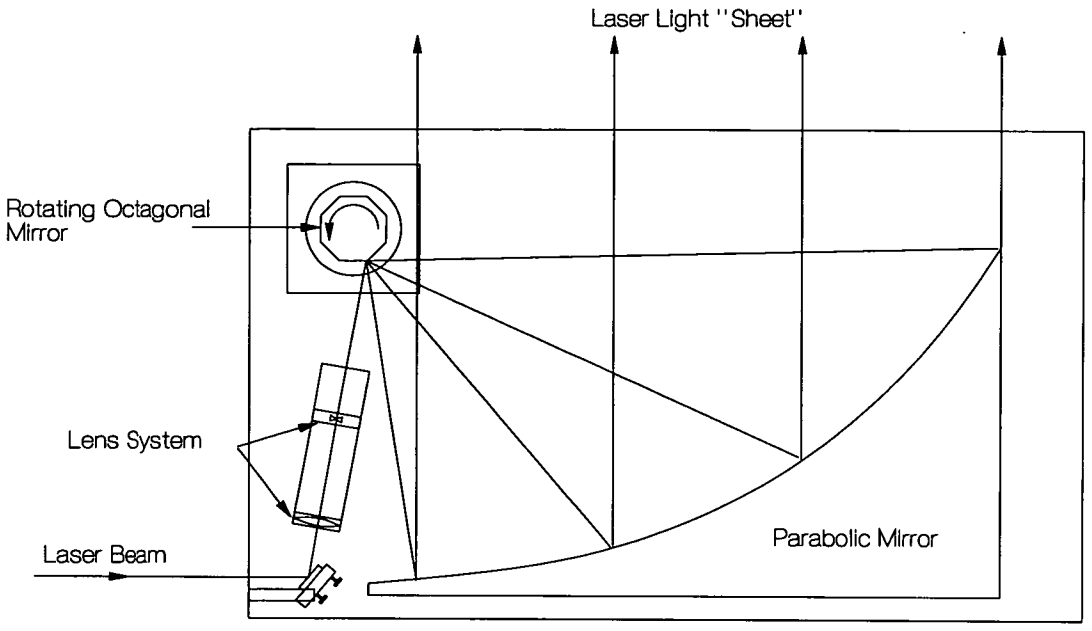

Figure 2.1: The Scanning Beam Illumination System.

face of the Aluminium plate, using double-sided adhesive tape.

The telescope arrangement uses achromatic lenses because the beam from the Argon Ion laser has nine wavelengths, consequently achromatic lenses can focus the beam much better than conventional lenses. The multiple wavelengths are formed by transitions from several excited states of the singly ionised Argon atom (Yariv, 1985): the most predominant one has a wavelength of 488 nm . Although it is possible to select a particular wavelength output, with an etalon for example, this is not desirable for this application because of the corresponding power reduction.

It is possible, and probably more common, to make a telescope arrangement with two convex lenses, as shown in figure 2.2A. However, this has two drawbacks, namely the quite large physical separation of the lenses (equal to f_1+f_2) and the fact that the beam converges to its minimum beam waist at the focus of the first lens. The beam at this point is at its most intense and consequently at its most dangerous. A further consequence of this second point, although not applying to this power of laser, is that the power may be so large at this point as to ionise

the air. This was observed for pulsed Neodymium:YAG (Yttrium Aluminium Garnet) lasers with a power of 200mJ/pulse (McCluskey, 1992b). To prevent this happening and to reduce the space between the two lenses for the same magnification, the second lens should be concave. This gives the beam diagram shown in figure 2.2B.

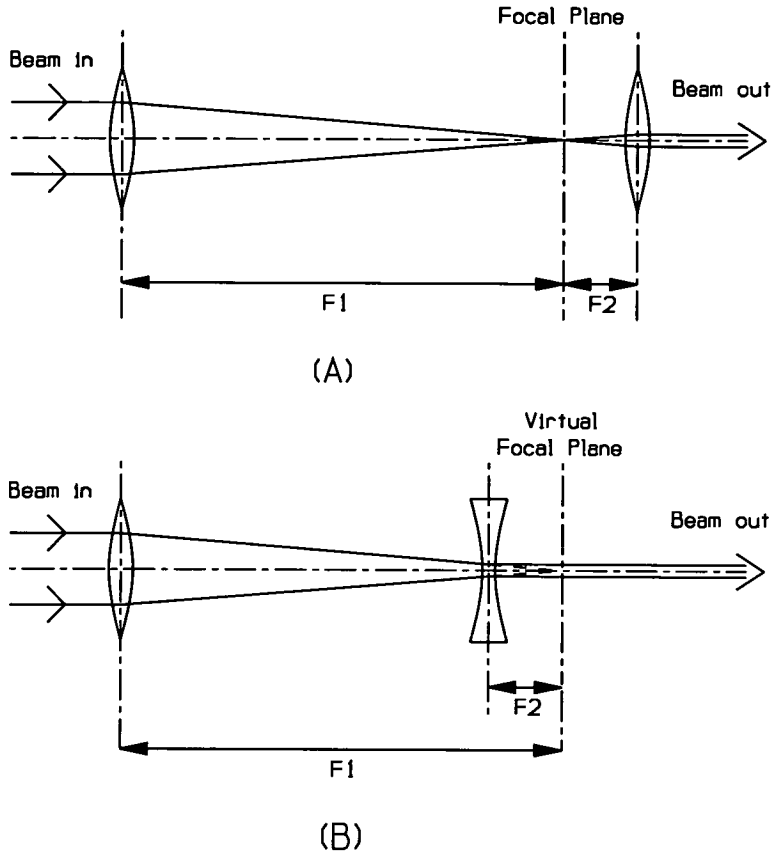

Figure 2.2: Telescope arrangements

The individual optical components are mounted on accurately turned spacers from the side walls, which are made from 8mm Aluminium sheet, this holds all the components correctly in the optical axis. All the component holders are made of aluminium and, along with the side plates, are black anodised to reduce dangerous laser reflections. Laser safety is an important factor when using a 15W laser, or any other Class 4 laser. Several steps have been taken to ensure the laser beam is enclosed all along its pathlength so that no accidental exposure occurs. These are described in section 3.2.2.

2.2.2 PIV Analysis

The PIV analysis system at The University of Edinburgh was developed initially by Callum Gray (Gray & Greated, 1988) and subsequently updated by David Skyner and Tom Bruce. It employs the Young's fringe technique where the autocorrelation function, $\hat{\nu}$, over a small interrogation area on the PIV negative, is calculated. This is now described in section 2.2.3.

2.2.3 Autocorrelation Function Calculation

Consider the simple optical system shown in figure 2.3. In the framework of the PIV analysis system we will consider the object to be a small interrogation area of the negative. This is coherently illuminated by a laser source and the function $f(x, y)$ is the two dimensional amplitude distribution of the transmitted light field. The image is formed in the focal plane of the lens. The lens performs a Fourier transform of the amplitude distribution, forming a complex image amplitude distribution, $F(u, v)$, where u and v are spatial frequencies. However, it is the modulus squared, ie. the *intensity* of this distribution which can be detected. In this case a CCD (Charge-Coupled Device) camera is located in the image plane and the digitised intensity distribution, ie. $|F(u, v)|^2$, is passed to a computer.

Turning now to a general mathematical description of correlation (Klein & Furtak, 1986) we can say that if correlation is the degree to which two functions "match-up" as they are moved relative to each other, then, for the general case of two complex functions (f_1 & f_2), we can define the *cross correlation* as

$$f_1 \otimes f_2 \equiv \int_{-\infty}^{\infty} f_1(x') f_2^*(x' - x) dx' \tag{2.7}$$

Substituting $x'' = x' - x$ we get

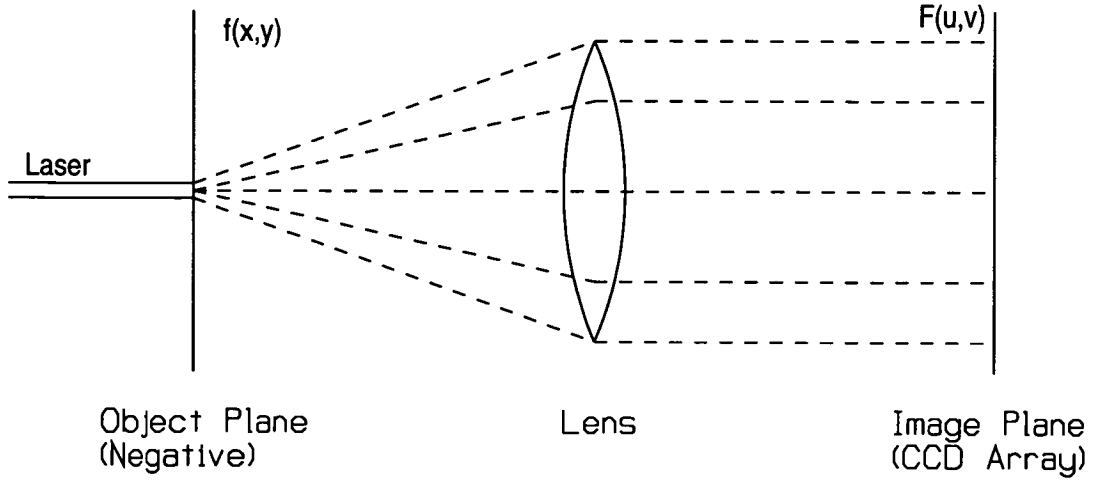

Figure 2.3: PIV Analysis System imaging set up

$$f_1 \otimes f_2 \equiv \int_{-\infty}^{\infty} f_1(x + x'') f_2^*(x'') dx'' \tag{2.8}$$

In two dimensions the cross correlation from equation 2.7 becomes

$$f_1 \otimes f_2 \equiv \int_{-\infty}^{\infty} \int_{-\infty}^{\infty} f_1(x', y') f_2^*(x' - x, y' - y) dx' dy' \tag{2.9}$$

When f_1 & f_2 are the same function ($f_1 = f_2 = f$) then we have the *autocorrelation* integral, denoted thus

$$\hat{\nu} \equiv f \otimes f \tag{2.10}$$

The Fourier transform of $\hat{\nu}$ can now be evaluated. From equation 2.8 we get

$$\begin{aligned} \mathcal{F}[f_1 \otimes f_2] &= \int_{-\infty}^{\infty} \int_{-\infty}^{\infty} f_1(x + x'') f_2^*(x'') dx'' e^{-\imath 2\pi u x} dx \\ &= \int_{-\infty}^{\infty} [\int_{-\infty}^{\infty} f_1(x + x'') e^{-\imath 2\pi u x} dx] f_2^*(x'') dx'' \end{aligned} \tag{2.11}$$

$$
\begin{aligned}
&= \int_{-\infty}^{\infty} e^{\imath 2\pi u x''} F_1(u) f_2^*(x'') dx'' \\
&= F_1(u)[\int_{-\infty}^{\infty} f_2(x'') e^{-\imath 2\pi u x''} dx'']^* \\
&= F_1(u) F_2^*(u) \qquad (2.12)
\end{aligned}
$$

where * denotes the complex conjugate. Returning to the special case of autocorrelation we have

$$\mathcal{F}[\hat{\nu}] = \mathcal{F}[f \otimes f] = |F(u)|^2 \qquad (2.13)$$

Taking the inverse Fourier Transform gives

$$\hat{\nu} = \mathcal{F}^{-1}(|F(u)|^2) \qquad (2.14)$$

The relationship shown in equation 2.13 is called the *Wiener-Khintchine theorem.*

Considering the PIV analysis system once again we can see from equation 2.14 that the autocorrelation function $\hat{\nu}$ over a small interrogation area is simply the inverse Fourier transform of the intensity distribution $|F(u)|^2$ which was passed to the computer from the CCD camera. This is carried out numerically using a fast Fourier transform (FFT) routine.

2.2.4 The PIV Analysis System

The layout of the current system is shown in figure 2.4.

The beam of a low power Helium-Neon laser passes through a spatial filter to remove high-frequency noise from the Gaussian beam profile. This is then collimated into a 1mm diameter beam, which hits the developed PIV negative mounted on a computer driven micro-translator. The intensity distribution of the Young's

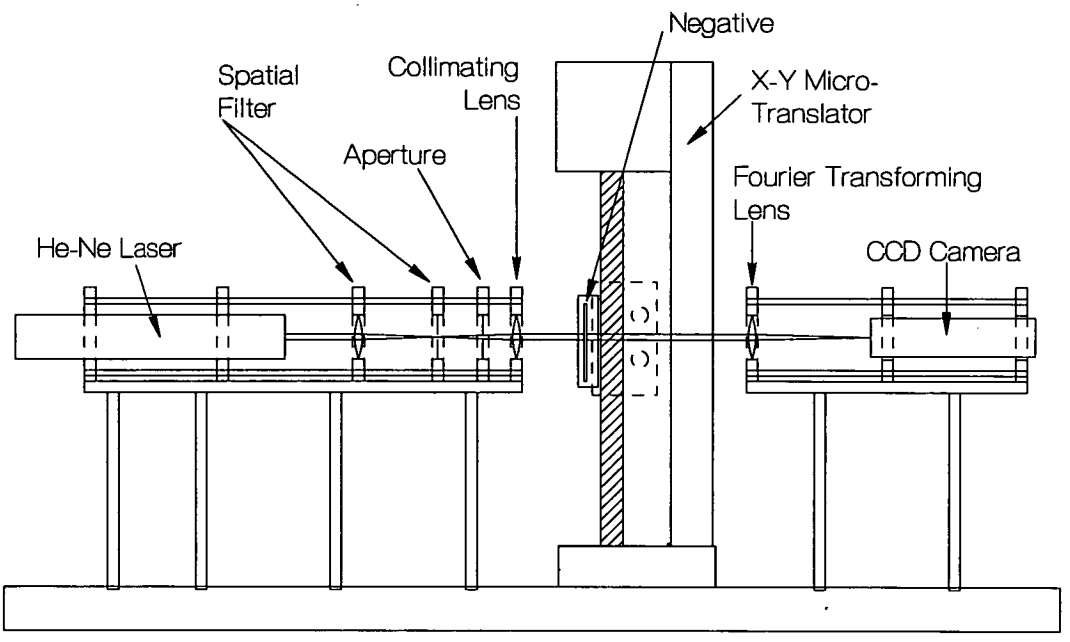

Figure 2.4: The automated PIV Young's fringe analysis system.

fringes is formed on the CCD array of a CCD video camera. The digitised image is passed to a PC (personal computer) via a framegrabber, and the autocorrelation function is calculated, as described in section 2.2.3. The peaks representing the most correlated image pairs are detected, the self correlation peak having been removed, and their separation and orientation are recorded. The computer moves the negative onto the next interrogation position where the process is repeated until the whole flow field is analysed. In this way the average particle displacement per interrogation area is calculated for the entire negative. When this is coupled with the accurate knowledge of the illumination pulse interval and the photographic magnification, the velocity field for the flow is obtained. The analysis time per point is about 2s, when the high-resolution 64x64 2-D FFT is calculated on a 486DX PC, operating at 33 MHz.

There have been attempts to perform the second Fourier transform optically, thereby cutting out the calculation time for a mathematical FFT. Moraitis (1988) gives quite a good overview of initial attempts and the various approaches used. Jakobsen et al. (1992) have achieved excellent results using an optically addressed

Spatial Light Modulator (SLM).

2.3 PIV Methods

2.3.1 PIV Photography of the Flow

The first stage in PIV is the photographic recording of the illuminated flow field. There are a number of criteria to be evaluated if optimal results are to be obtained. For the time being we shall consider the case of the wave tank without a beach profile installed. The scanning beam illumination system is located beneath the wave tank and illuminates a 1m long section of the flow, only 2 - 3mm thick. A camera is mounted in front of the flow field on a tripod, as shown diagrammatically in figure 2.5.

In these experiments a 15W Argon ion laser is the light source. This powerful laser is required for two reasons. Firstly, only a thin sheet, approximating the 2-D limit, in the flow is required. This is best obtained with a laser source. Secondly, as it is the side scattered light off very small seeding particles, illuminated for very short times, that is recorded, a very powerful source is required.

The main parameters to be optimised for the best results are the magnification of the imaged flow field and the scan period of the laser beam. These factors are selected to ensure that the separation of the multiple images of the seeding particles are far enough apart at the lowest velocity to be resolvable, but not too far apart at the highest velocity that the multiple images fall outside the interrogation area of the analysing laser beam. This effect is shown in figure 2.6.

It has been found that the minimum resolvable particle separation on the film is 30 μm, for particles of about 7 μm on the film, the maximum being 300 μm; an effective resolvable dynamic range of 10. In calculating initial values for both the

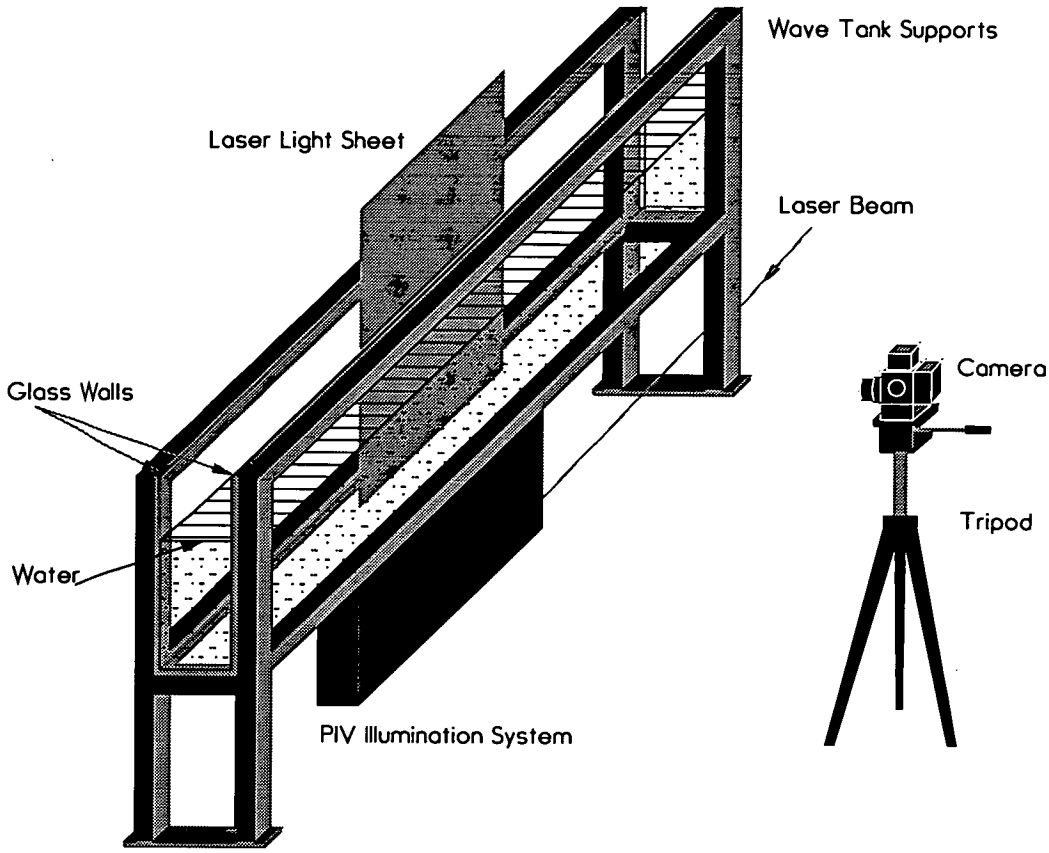

Figure 2.5: The apparatus set-up for PIV photographs

magnitude and scan period, it is advantageous to have an approximate knowledge of the maximum velocity likely in the flow field. This estimate need only be quite rough as a test film is always taken to fine tune these parameters. In the experiments performed in this study the maximum velocity was estimated by manually timing the progress of the crest of the wave across one 3m zone of the wave tank. The velocity data in the analysis system is calculated using equation 2.15,

$$\vec{V} = \frac{CM}{T}\vec{D} \tag{2.15}$$

where M is the magnification, T the scan period and $\vec{D}$ the displacement as measured on the analysis system. C is a system specific constant for converting the displacement measured on the analysis system from the CCD camera pixel units, to metres. As the magnification is usually governed by the size of the flow

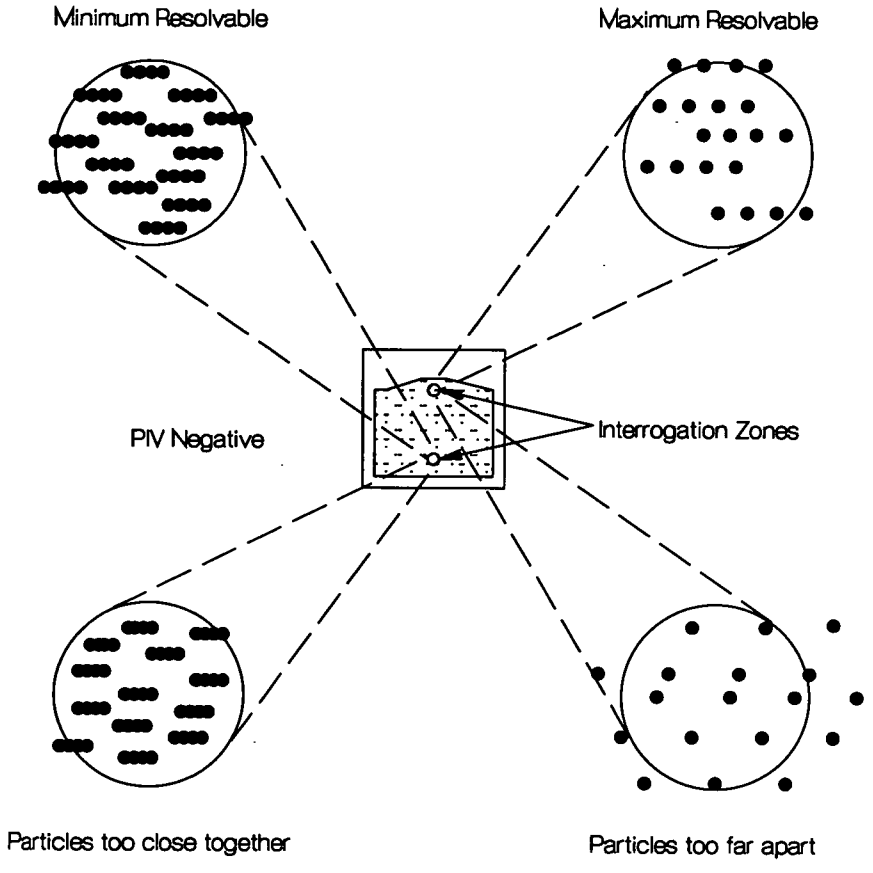

Figure 2.6: Maximum and minimum particle separations

to be measured, it is the scan time which is usually adjusted. However, this often has a limited range and if the estimate of the period calculated from equation 2.15 is outside this range, then the magnification may have to be compromised in order to optimise the dynamic range resolvable.

A further consideration is seeding particle size. The seeding should be small enough to follow the flow, with little or no relative motion to it, but large enough to be resolved on the film. Also one should remember that the larger the particle, the more light it scatters. In all of these experiments, Conifer pollen was used as the seeding material, this is approximately 70 μm in diameter, scatters light very evenly and is very nearly neutrally buoyant in water.

The camera is now mounted on a tripod and placed in the correct position as

determined by the chosen magnification. Location of the camera is important; a careful alignment technique is employed to ensure the camera is horizontal and perpendicular to the wave tank. The camera is raised on the tripod until the cross-hairs in the viewfinder intersect with the water surface. The camera is then rotated until it is perpendicular to the wave tank. This is achieved by aligning the camera with its reflection in the glass wall of the tank. The camera is then tilted to align the horizontal cross-hairs in the viewfinder with the water surface. With the camera now leveled, it is lowered 0.2m and centered on a location mark on the tank wall, again the camera is adjusted to be perpendicular using the reflection technique just mentioned. There are small cross shaped location marks every 0.2m along the tank at the water level and at a depth of 0.2m. These marks are very important as they are the only way of ensuring that you can match the position of the measured flow field back to the original. If no registration marks are recorded the estimate of exactly where in the flow a measured velocity occurred is prone to high levels of inaccuracy. This point will be mentioned further when an analysis of the sources of error is carried out in section 2.4. The reason the camera is lowered from the still water line is to ensure a clear view of the underside of the water surface, where the illumination sheet intercepts it in the middle of the tank, is maintained for the whole cycle of the wave including the trough.

The next step is to select the camera shutter speed and lens aperture. The shutter speed should be short enough that the flow field does not significantly change in that time span, but long enough to allow at least two, but preferably four or more, scans of the laser beam. If the shutter speed was too low to assume the flow field did not change, then the scan rate would have to be increased with a corresponding change in magnification. The shutter speed of a camera is selected in discrete steps, whereas the scan time can be varied continuously. This means that a non-integer number of scans is more than likely. This does not pose a problem because with the scanning beam system a non-integer number of scans means that one part of the flow will have N multiple images and another part will have N-1. As long as N-1 is greater than two, then fringes will still be obtained in this region.

The aperture of the lens is set with several parameters in mind. In general, the smaller the aperture the greater the depth of field, δz, (see equation 2.16) and the smaller the lens distortion. However, a small aperture vastly reduces the amount of light entering the lens. A second reason for a wider aperture is the increased resolution of small particles due to the diffraction limit of the lens. The diameter of the image is determined by the diameter of the object, ie. the seeding particle, the magnification and the point response function of the lens. If the lens is diffraction limited then the point response function will be an Airy distribution whose diameter is given in equation 2.17 (Adrian, 1991)

$$\delta z = 4(1 + M^{-1})^2 f^2 \lambda \tag{2.16}$$

$$d = 2.44(1 + M)f\lambda \tag{2.17}$$

where M is the magnification, f is the f-number of the lens (defined as the ratio of the focal length:aperture diameter) and λ is the wavelength. If we substitute in typical values for these variables, ie. $M = 0.1$, $f = 4$ & $\lambda = 488$ nm we find (from equation 2.17) the minimum particle size is $\sim 5.3\mu$m. As the conifer pollen we are using as a seeding material is typically 70μm in diameter, it is easily resolved. Although increasing the aperture increases the effect of lens aberrations, this is a very small effect for a good quality lens. Tests have been carried out (Gray, 1989) and setting the aperture one stop down from its maximum appears to be the best compromise; in this case f4.

The film used, like all the photographic equipment, is of the highest quality. Kodak T-Max 400 ISO was used for these experiments in the 120 format. The camera is a Hasselblad 500 EL/M fitted with a flat field 80mm Carl Zeiss lens. The high quality of this equipment is required to reduce errors to a minimum. This is fully discussed in section 2.4.

Focusing the camera on the light sheet is not as straight forward as one might

think. In practise, three focus positions, one either side of the apparent correct focus position, are tried on the first test film. In addition to the focus position being tested, the magnification of the set-up is recorded by photographing a regular grid placed in the light sheet in the wave tank. The magnification, for use in equation 2.15, is measured on the developed negative using a travelling microscope. In this procedure four lines of ten grid cells are measured and the average grid cell dimension is calculated.

A further practical requirement for taking PIV photographs is that the laboratory has to be blacked out. This may be difficult in a large facility where a number of people work, or which has large or inaccessible windows. The laboratory used in this study was specially designed for total blackout.

The exposed film has to be developed before the analysis phase. This is done in the standard way, using Kodak T-Max developer and Amfix fixer. Push processing was occasionally required when the laser power dropped, as happens from time to time, for various reasons such as the end mirrors of the laser cavity needing cleaning.

2.3.2 PIV Negative Analysis Procedure

As mentioned in section 2.1 the analysis system employs the Young's fringe method. The system at Edinburgh has been developed to a stage of a commercial package and as such is now used by the whole group as an easy to use, but very powerful tool. Refer back to figure 2.4 for a diagram of the optical part of the system, and to section 2.2.2 for a description of the system. In this section the actual procedure for analysing a PIV negative and the initial processing of the raw data will be described.

Dealing first with the analysis procedure: the PIV negative is loaded into the perspex holder of the apparatus. Care is taken to ensure that the film is horizontal in the holder. In practice this means the negative is placed on its side so that

the straight edge of the film rests on the accurately machined edge of the holder. It is at this stage that the purpose of the reference crosses on the tank, first mentioned in section 2.3.1, becomes apparent. These crosses are the only sure way of obtaining accurate position information. The laser beam of the analysis system is located on the reference mark in the centre of the negative, for which an absolute x- and y- coordinate is known. Analysis is then carried out relative to this point thus ensuring the positional integrity of the velocity data. The reference mark coordinates, magnification and scan time can be input into the system so that the displacements measured are output in SI units. Analysis is carried out on a regular, rectangular grid of points, usually $\sim$ 1mm apart on the film.

There is one major factor still to be dealt with. The analysis system measures the displacement of the particles on the film by finding the most correlated particle separation. This results in two peaks in the autocorrelation plane, produced by the optical and numerical Fourier transforms, described in section 2.2.3. However, the most correlated particle separation is that of zero displacement, corresponding to self correlation. This is of no use and is so big that it swamps the desired signal peaks, and so has to be removed. This is done in a combination of ways; the first, and most straightforward, is to set the height of the autocorrelation peak within a small radius of the origin to zero. The radius must be set carefully to ensure that the Gaussian self-correlation peak is entirely removed, otherwise the edges, caused by the incorrect cut-off of this peak, may be larger than the displacement peaks and would therefore be incorrectly detected. This is shown in figure 2.7.

The second way of removing the self-correlation peak is to record the halo function of the diffraction pattern caused by the size of the individual particle images. The halo is recorded by taking a series of 40 fringe patterns with the PIV negative randomly orientated for each pattern. This is subtracted from the autocorrelation plane before the peak location routine is run. Unlike the first approach, this procedure does not blindly set everything within a specified radius of the centre to zero. This is beneficial when there are areas of low velocity magnitude in the flow; because the signal peaks formed in these areas may overlap the edges of the self-correlation peak. Subtraction of the halo function leaves the signal peaks

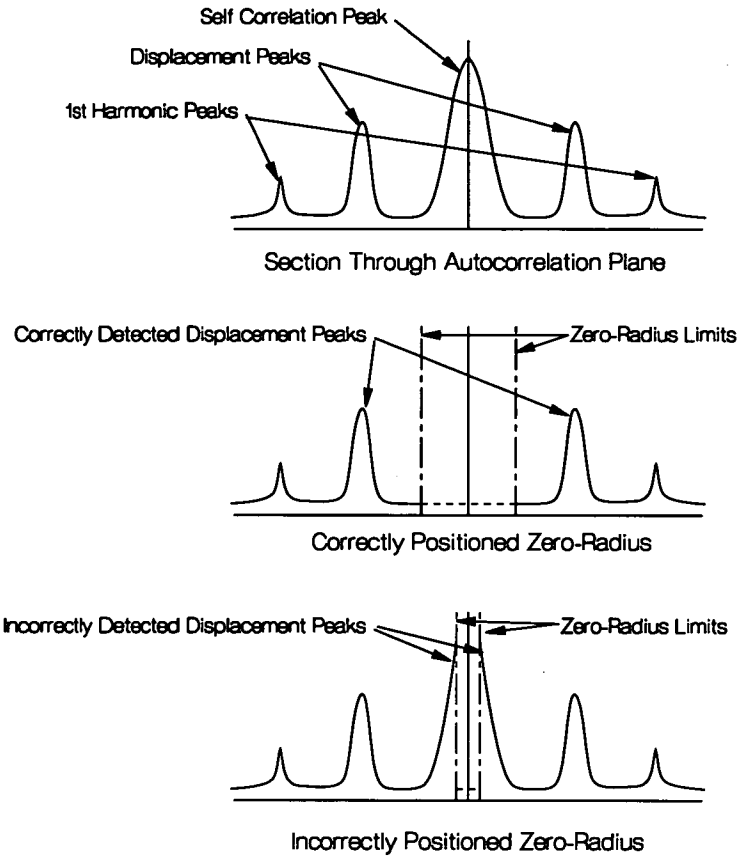

Figure 2.7: Zero-radius selection

exposed and resolvable, whereas they would be set to zero with the previous method (Gray, 1989).

These two functions are only important if the dynamic range of the flow is quite large and incorporates near zero velocities. This was the case for some areas of the flows encountered in this study. The technique of image shifting superimposes a known shift velocity on the flow, which is large enough to ensure that the maximum velocity opposing the shift velocity is still big enough to be comfortably resolved. Examples of results from hydrodynamic experiments using an image shifting system include Bruce & Easson (1992) and Morrison & Greated (1992). Such a system was not available for this study and consequently has not been used, however, it is recommended that in future projects of this sort image shifting is incorporated.

Once the zero radius has been set and the halo recorded, if necessary, the analysis can proceed automatically. The analysis rig steps through the specified grid at a rate of 1 point every 2 seconds. There is a facility to mount up to four 120 negatives in the holder which can then be analysed automatically, allowing the system to be run with minimum human intervention.

The final phase of analysis is the initial processing of the raw data. A program, written by David Skyner and Tom Bruce, allows the user to edit the data file to remove spurious vectors from areas above the water surface or below the beach, or any vectors which are obviously wrong when compared with the surrounding flow. An example of the raw data obtained from the analysis of one negative is shown in figure 2.8

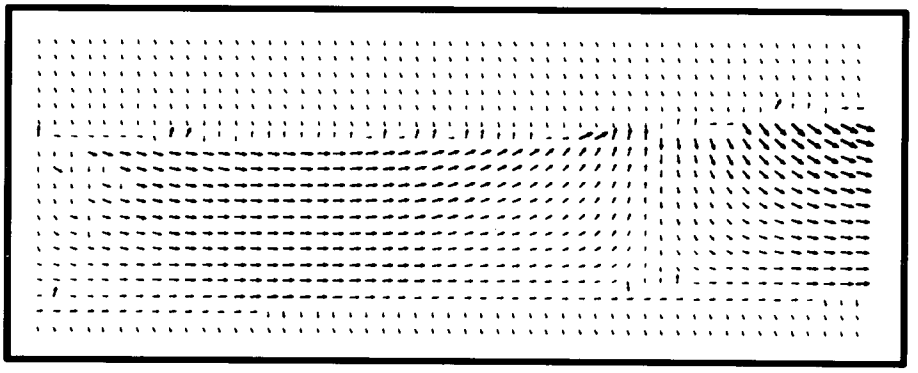

Figure 2.8: The raw data produced by the automated PIV analysis system

A second inherent problem in this type of PIV analysis is also evident in figure 2.8, that is there is a 180° directional ambiguity in the possible orientation of the velocity vectors. This is due to the fact that the system cannot tell which of the multiple images was the first or the last. This can be seen in the figure from the obvious discontinuity of two sections of the flow. At the analysis stage a preferred alignment of the vectors can be selected, in this case to the right, in order to make post-processing easier because one can reverse the direction of a block of vectors, rather than have to individually reverse 50% of the vectors randomly placed throughout the flow field. This directional ambiguity does not really pose a problem in this particular application, because one knows *a priori* the direction

of the velocity vectors under the crest of the wave. They must be aligned with the direction of propagation of the wave. All the other vectors can then be aligned by continuity. Although this was done manually, it did not introduce operator bias.

There are many instances when the direction of the flow is not known, in highly turbulent flows for example. In these cases image shifting once again solves the problem. If one calculates the shift velocity to be greater than the maximum velocity opposing the direction of the flow, then all the vectors in the flow must point in the same direction as the shift velocity. Subtraction of this shift velocity at the post-processing stage reveals the true structure of the flow. Once again refer to Bruce & Easson (1992) and Morisson & Greated (1992) for examples of flow measurements using image shifting. A similar outcome is obtained when one has a flow where the mean velocity is large and mostly unidirectional, but the turbulent structure within that flow is of interest. In this case the mean velocity is subtracted to reveal the turbulent structure. McCluskey et al. (1993) performed some experiments in a small scale wind tunnel to measure the turbulence of air flow past a grid.

Once the spurious vectors have been removed and the direction of the vectors checked, one is left with a detailed and accurate record of the velocity distribution of the flow.

2.4 Inherent errors in the PIV technique

2.4.1 Introduction

If PIV is to be a useful tool for measuring fluid flow then an estimate of the errors inherent in the technique must be made. Work has been carried out on this topic, initially by Gray (1989) and subsequently by Quinn et al. (1993) for the current application. Keane & Adrian (1990, 1991) describe the optimisation of the various parameters of the technique in some detail.

In the following sections the principle uncertainties involved in different aspects of the PIV process are considered. As the majority of this work was performed by a combination of the authors in Quinn et al. (1993), only those sections appropriate to the measurement of waves on beaches will be described. However, knowledge of the dependency of various parameters is essential for the understanding of the technique and so all points will be at least outlined. A summary of all the error contributions is given at the end of the section.

2.4.2 Error Analysis

Considering equation 2.15 for the calculation of the velocity from the measured displacement of the particle images, there are three empirical constants. These are the analysis system calibration factor, C, the photographic magnification, M and the illumination scan time, T. They can be measured directly and uncertainties assigned accurately. These errors can be made to be small; down to within 0.1% of their associated value.

The main source of error in the velocity comes from the measurement of the displacement, $\vec{D}$. The uncertainties associated with $\vec{D}$ arise from both the photographic recording of the flow and the subsequent analysis of the developed negative. These are now dealt with separately in detail.

Uncertainties in the Photographic Recording of the Flow

Sources of errors inherent in this phase of PIV fall into two categories: the assumption that the seeding particles faithfully follow the fluid motion; and the characteristics of the optical recording system. The effect of the former is minimised by appropriate choice of seeding particle.

The characteristics of the optical recording system will be system specific, depending on the configuration and components used, and factors such as optical

distortion of the imaged flow, 3-D velocity components in the flow, limited resolution etc. These will combine to provide a net error in the recorded flow. These errors can be divided into systematic and random errors.

- **Systematic Errors**
  - *Distortion of image flow field due to:*
    * Geometric distortion by the camera lens.
    * Refractive index changes between the measurement zone and the camera.
    * Perspective.
    * Out-of-plane velocity components.
- **Random Errors**
  - *Distortion of particle images due to:*
    * Grain noise.
    * Adjacency.
    * Shrinkage.

The effects of the systematic errors do not change between measurements and, in principle, their effects can be measured and accounted for in the final measurements. Some of these errors can be minimised by the choice of high quality photographic equipment and materials.

An estimate of the individual effect of the various random errors cannot be made, but their overall effect can be evaluated by making a set of artificially produced PIV negatives to be analysed. This is dealt with in more detail later, when considering the analysis system calibration.

Limitations of the Analysis Method

The Young's fringe analysis system measures the mean particle displacement within a small localised region of the developed negative. This is achieved by taking the autocorrelation of the amplitude transmission distribution across the local region of film, by means of optical and computational Fourier Transforms. There are several sources of error arising from this process:

1. The limited quality of the Fourier transforming lens will introduce some distortion to the resulting power spectrum. In addition to this, noise will be introduced by the refractive index and film thickness variations across the negative.

2. Quantisation errors associated with the digitised power spectrum data, and rounding errors in the numerical calculation of the autocorrelation function.

3. The influence of random correlation noise in determining the centroid of the signal peak.

4. The effect of the discrete and random sampling of an effectively continuous flow by the randomly distributed particles.

The first and second points are functions of the quality of the components and their influence can be minimised by appropriate choice of equipment. The third and fourth points are more fundamental in nature and are due to the manner in which the flow velocity information is represented on, and measured from, the recording medium. These last two points have been addressed by means of a Monte Carlo simulation of the PIV process, described in detail by Gray (1989). The study took into account variations of the parameters involved in PIV, primarily the seeding concentration and velocity gradients across the probe region. A more extensive study, using similar simulations along with an analytic treatment, has been carried out by Keane and Adrian (1990, 1991).

Seeding concentration levels and velocity gradients have a variable error contribution across the PIV negative, these two points are now dealt with individually.

It was found (Gray, 1989) that there was a rapid decrease in error as the seeding concentration varied from 3 to 10 particle pairs per interrogation region, but beyond that there would be little significant reduction in errors. This result is similar to that found by Keane and Adrian (1990, 1991).

The larger the particle displacement the higher the chance of the multiple particle images falling outside the interrogation region. The effect of this is to artificially reduce the seeding density, and introduce a bias to selecting smaller displacements. This is an important effect and causes an error which varies with displacement gradient across the interrogation region. Keane and Adrian (1990, 1991) found the systematic bias to introduce errors varying linearly with displacement gradient. The error, relative to the maximum velocity, varies from 0-5% over a range of gradients from 0.00-0.08. Here we define the displacement gradient to be the change in displacement across the whole interrogation area. The definition favoured by Keane and Adrian (1990, 1991) is half of this.

The effect of a large velocity gradient across the interrogation area is to spread the displacement peak in the autocorrelation plane over a larger area, hence reducing its height. This increases the random error associated with the velocity measurements. In addition, the probability of a random correlation peak being selected also increases, introducing an upper limit to the velocity gradient in the flow which will still yield correct velocity measurements. This problem manifests itself by producing vectors of random magnitude and orientation which have no continuity with any of the surrounding vectors, and are easily identified and removed.

Analysis System Calibration

The influence of the random errors mentioned in section 2.4.2, combined with the sources of errors in the analysis phase, can be estimated by making a series of artificially generated PIV negatives. These can be formed most conveniently by accurately plotting a random pattern of groups of N dots where the dot size and the spacing within the groups are specified. Photographing the printed output produces a transparency with a known particle displacement. The whole negative is analysed to obtain an estimate of the variation from this known displacement.

A series of negatives with different particle displacements were analysed and the relationship with the measured displacements was linear. The calibration constant was found with an uncertainty of only 0.1%.

2.4.3 Uncertainties Arising in Water Wave Measurements

Equipment Selection

To minimise the effect of errors high quality photographic equipment is used. The camera used was a Hasselblad 500 EL/M fitted with a Carl Zeiss 80mm, f 2.8 flat field lens.

Photographic Distortion

The distortion due to the camera lens can be measured by photographing a regular grid. At the corners of the developed negative the distortion was found to be at worst 1.5%. The effect of the lens distortion and the refraction at the tank walls conveniently oppose each other, so that there is a combined distortion which is almost exactly constant with variation in image height. The variation from the mean has a standard deviation of only 0.3%.

One must remember that these errors due to distortion and refraction have their maximum values at the edges of the field of view, and typically the area of interest is placed at the centre of the field of view where these, already small, errors are further diminished.

Scanning Beam System Errors

There is a possibility of a small uncertainty in the illumination interval with the scanning beam system, due to subsequent illuminations of a given particle being at different positions in the measurement zone, and hence different phases of the scan cycle. If the averaging areas for each PIV interrogation are small compared to the total *sheet* length, then these errors are very small (Gray et al., 1991). In this particular application the error is always less than 0.25%.

A further problem which is more likely to arise with the scanning beam system than with beam expansion is the flatness of the resulting *sheet*. Variations from a plane result in the effective magnification being different in different regions. Typically the *sheet* is flat to within $\pm$3mm, which results in a .3% error if the camera is positioned 1m away. The effective thickness of the *sheet* is about 2mm which gives a random magnification error of 0.1%.

Seeding

In the water wave studies carried out at Edinburgh, conifer pollen has been found to be the most successful seeding material. This is $\sim$ 70μm in diameter and, when wet, has approximately the same density as the water, having a very small tendency to float, with typical rise velocities of the order of 0.25mms^{-1}. As typical flow velocities for laboratory waves are around 1ms^{-1}, this represents an error of about 0.025%. As the maximum accelerations in water waves are of the order g, the acceleration due to gravity, the relative motion of the water and the particles will not deviate significantly from the stated error.

Out-of-plane Motions

Out-of-plane motion can produce errors in the region of about 20% if that motion is of the same order as the in-plane motion, (Sinha, 1988). However, in the application to measuring water wave velocities in a 2-D wave flume the 3-D component is minimal, assuming cross-waves are not generated; thereby reducing the error to a negligible amount. This factor was verified by exposing the negative for a complete cycle of a sine wave. The resulting circular traces on the negative indicated little, if any, out-of-plane movement. Care must be taken to reconsider these assumptions when, for example, measurements are made of the turbulent flow field following wave breaking.

2.4.4 PIV Errors for Waves on Beaches

Having addressed the considerations general to the measurement of water wave kinematics with PIV, this section focuses on the particular application of waves breaking on sloping beaches.

There are several problems which have arisen during these experiments, these subdivide into those associated with PIV, with illumination cost, and the flow field being studied. They can be summarised as follows:

1. Areas of high velocity variation in small water depths.
2. Water aeration due to breaking waves.
3. Dynamic range limitations.
4. Attenuation of the laser beam through the water below the beach.
5. Contrast.
6. Light losses at optical components.

7. Wave repeatability for intercomparison of different wave phases.

8. Deformation of the transparent plastic under wave attack.

These aspects are now dealt with in some detail.

Velocity Gradients.

It is possible to make an assessment of the systematic and random errors due to velocity gradients in the waves measured, given the general dependencies discussed in section 2.4.2. Figure 2.9 plots an overall probability distribution for the velocity gradients present in twelve representative flow fields measured in the study. By reference to the systematic errors discussed in section 2.4.2, the expected systematic biasing and random variation of the results can be estimated for the whole data set. The bulk of the distribution is centered around 0.01, with associated errors of about 0.6% and 0.3%, respectively. However, it should be noted that in water waves the main areas of interest normally have the highest velocities and velocity gradients.

A particular velocity gradient probability distribution is plotted in figure 2.10 for one of the waves known to have especially high velocity gradients. In this case the systematic and random errors can be estimated to be about 3.0% and 2.0%, for the extreme displacement gradient of 0.05.

In this type of study the problem of velocity gradients becomes more severe as the water depth becomes smaller, if the photographic magnification remains about the same. The water depth in the backwash in front of an incoming breaking wave is only about 30mm, at our experimental scale. This corresponds to a depth of 3mm on the film, which is only three interrogation intervals. The area just in front of the breaking wave has high accelerations as the velocities change from mainly horizontal in the backwash to strongly vertical in the front face of the breaking wave. These areas of high velocity gradient are, therefore, very difficult to measure accurately.

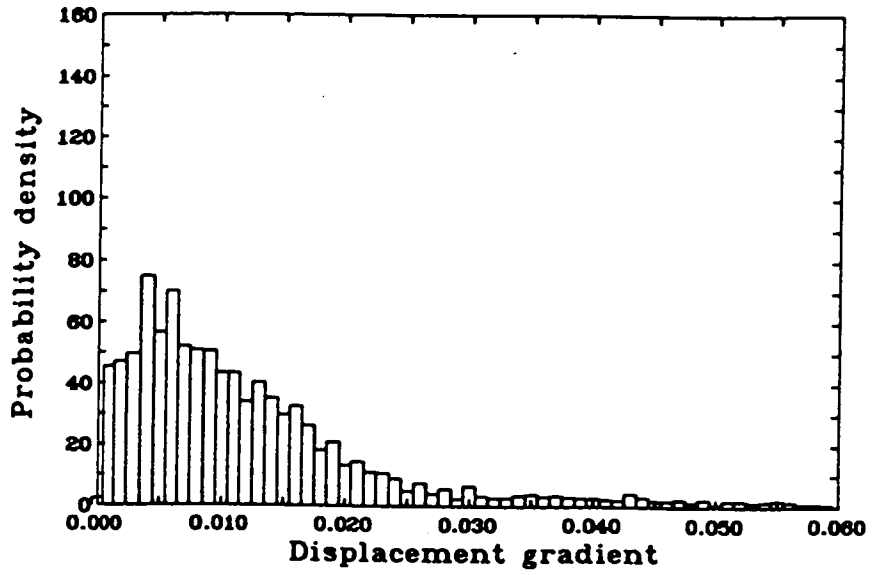

Figure 2.9: Probability distribution of velocity gradient for 12 representative flow fields.

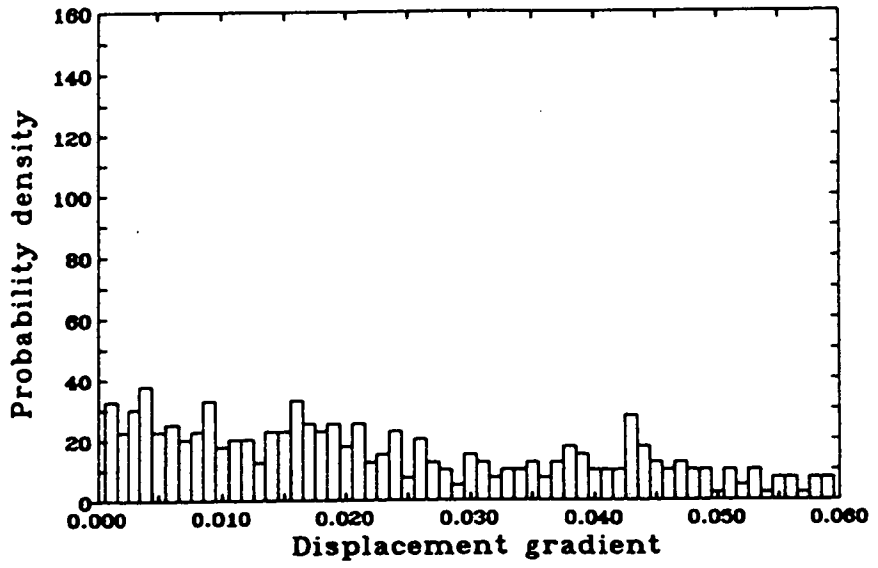

Figure 2.10: Probability distribution of velocity gradient for an extreme flow field

Water Aeration.

The flow in the post breaking zone is highly aerated. The regions of air and white water cause significant signal drop-out. In general, only the areas of the backwash which have relatively constant velocities and where the air bubbles have risen to the surface will give reliable results.

Dynamic Range.

The dynamic range of the PIV system also imposes a limitation on the technique. The system at Edinburgh has a dynamic range of ~ 10. By using image shifting techniques, as described in section 2.3.2, the measurable velocity range could be chosen to include zero velocities, with an accompanying increase in errors if the original maximum velocity was still to be resolved. Image shifting systems are required for measurements where the direction of the flow is not known *a priori*, eg. for turbulence measurements past cylinders or through grids, etc. However, for the application to waves travelling along a wave flume the direction of the velocity vectors is aligned with the propagation direction under the crest of the wave and the direction of other velocities in the flow are determined by continuity. This type of study, therefore, is particularly well suited to the Young's fringe analysis system as the inherent directional ambiguity in taking the autocorrelation does not pose a problem.

Beam Attenuation through water.

The quality of the water greatly affects the attenuation of the laser beam and the contrast of the illuminated seeding particles. It was found that with clean water the beam intensity was reduced by 35% over the whole water depth of 750mm, but this attenuation increased to about 75% when the water quality was poor. This problem necessitates that the path length in water be minimised and the water to be changed regularly if illumination requirements (and therefore costs) are to be

Optical Component	*Reflection Coefficient*
Beam steering Mirror	95%
Beam collimating Lenses	1% & 6%
Rotating Octagonal Mirror	80%
Parabolic Mirror	73%
Tank Wall	20%

Table 2.1: Reflection coefficients for the optical components.

kept as low as possible. This will be an important factor in large facilities where water quality is not good, or the water can not be changed easily. However, the underlying requirement for successful PIV photographs is good contrast between the seeding particles and the background, and it is this contrast which decreases with a reduction in water quality.

Light losses from Laser to Wave Flume.

The photographic recording phase of the PIV process requires a high intensity, collimated light source. This is generally provided by a high power laser; in these experiments a CW 15W Argon ion laser is used. Light losses due to optical components in the beam path must be minimised if laser costs are to be kept down. The reflection coefficients for the optical components in the beam path have been measured by an intensity meter, and are shown in table 2.1.

The light losses due to the rotating mirror, parabolic mirror and the walls of the tank are quite considerable. However, very little can be done to improve these due to their design. The rotating mirror's surface is diamond machined, not optically coated. Any optical coating would tend to dissociate itself from the octagon under high speed rotation. The parabolic mirror is made by optically coating a long, thin strip of perspex and then attaching this to a machined aluminium parabola. Optically coating perspex is not as successful as coating glass, and bending the

perspex into a parabola will cause some small deformation of the reflecting surface. The losses incurred due to the tank walls are due mainly to the thickness of the glass. This thickness cannot be compromised due to mechanical loadings. The losses over the beam path mean that, in this case, the intensity of the beam is reduced from 15W to 4.2W at the bottom of the tank. Assuming good water conditions, the intensity of light falling on the seeding particles at the crest of the wave will be $\sim$ 2.7W. The transmission coefficient of the transparent plastic coating for the beach (see section 3.3) is good when clean. However, as the pollen used as seeding material is slightly less dense than the water, it tends to float, over a period of many hours. The seeding that passes under the beach, therefore tends to coat the underside of it. This greatly reduces the transmission factor of the transparent strip. As the beach is long, cleaning the underside of the strip is difficult. In general, the transparent plastic is replaced frequently: typically, every two or three days.

Wave Repeatability.

In order to obtain velocity measurements all along the beach, the velocity fields of several PIV negatives must be joined together. This can only be done if the wave repeatability is good. The triggering of the camera is computer controlled to record four phases, each separated by $\frac{\pi}{2}$, of each wave at each position. To test the wave repeatability, a fifth phase was recorded. The first and fifth phases should be identical. The maximum horizontal velocity component in each of these two waves differed by only 1.5%.

Deformation of Beach Covering.

The transparent plastic used to cover the gap in the beach necessary for optical access, is overhead projector transparency (in roll form). This is inexpensive, readily available and has good optical properties. It is, however, very flexible - a factor essential for its use on complex beach forms. In the unsupported region that

forms the gap up the middle of the beach the plastic may deform. To minimise this effect it is carefully attached to the beach, with lengths of double sided adhesive tape, maintaining tension across the gap. The deflection should not introduce any significant effect to the laser beam's transmission, as the plastic is very thin, refraction effects appear to be negligible. By examining the wave profiles as they propagate along the beach, there does not seem to be any deformation in the wave front near the middle, suggesting that any deflection of the plastic is small enough not to affect the waves. The observation of how evenly the wave fronts behave while breaking is a good indicator as to how level the beach is across the tank.

2.4.5 Summary of Errors and Uncertainties

The errors and uncertainties identified in the application of PIV to the measurement of wave kinematics on sloping beaches are summarised in table 2.2. The percentage errors given refer to the typical errors relative to the maximum velocity measured in the particular flow field.

2.4.6 Conclusion

The combined systematic and random errors relative to the maximum velocity in the flow, for PIV measurements of water waves varied mainly with particle displacement gradient across a small interrogation region on the negative. With a low displacement gradient of about 1% the combined error was found to vary from 1.2% to 2.0%, depending on the variation of further systematic errors, such as photographic distortion. With an extreme displacement gradient of 5%, the combined error varied from 5% to 6%. These two displacement gradients correspond to typical and extreme cases for the present study of waves on beaches, with the higher gradient occurring at shallower water depths near the breaking point. In addition to the errors associated with the PIV measurements there was an additional wave repeatability error of 1.5% between the first and last recorded

General Area	*Particular Factor*	*Random Error*	*Systematic Error*
Fringe analysis	Analysis calibration factor	0.1%	
Water wave studies	Illumination interval	0.2%	
	Photographic magnification	0.3%	
	Photographic distortion		0.0%-0.3%
	Illumination plane flatness		0.0%-0.3%
	Illumination plane thickness	0.1%	
	Scanning-beam time effect		0.0%-0.2%
	Seeding not following flow		0.1%
Waves on beaches (PIV errors)	Velocity gradients	0.3%-2.0%	0.6%-3.0%
TOTAL (PIV)		0.5%-2.0%	0.7%-3.9%
Waves on beaches (Other errors)	Wave repeatability	1.5%	

Table 2.2: Individual errors for PIV applied to waves on beaches.

phases of the wave. The inherent accuracy of the technique, as has been shown here, is one of its main advantages.

Chapter 3

Experimental Facility and Beach Construction

3.1 Introduction

The experimental facilities developed in Edinburgh over the last few years have been custom built for optical flow measurements. A wave tank, designed by Skyner (1992), was constructed, with the author's help, during the first part of this project. It's base and walls are made from 25mm thick glass to allow complete optical access. The PIV illumination and analysis systems were as described in Chapter 2, with the illumination system and general laser supply optics being designed and installed by the author. A detailed description of the experimental facilities and the construction of the various beach profiles to be used is given in the following two sections.

3.2 Experimental Facility

3.2.1 The Wave Tank

As the main measurement technique to be used in the flume requires photographing the flow field it was desirable to reduce the number of tank supports to a

minimum by maximising the length of the glass sections in between. The largest commercially available glass plate with a thickness of 25mm is just over 3m in length. This meant that the wave tank was built in three 3.25m long sections, making a total length of 9.75m, the internal width of the wave flume is 0.4m and it has a still water level of 0.75m. It is the water depth which is the main parameter governing the thickness of the glass. The thickness was selected based on the fact that the maximum deflection of the glass with the standard water depth should be 0.5mm. In addition to this it was checked that the forces on the glass sections were well within the manufacturers guidelines if the tank was overfilled. The main supporting members of the tank are box section mild steel. These hold accurately adjusted lengths of Aluminium angle which in turn hold the glass in place. A full description of the tank construction is given in Skyner (1992). A sketch of the wave tank is given in figure 3.1. The wave tanks and laser illumination systems have all been made in the workshops of the Physics or Mechanical Engineering departments, from designs of the research personnel.

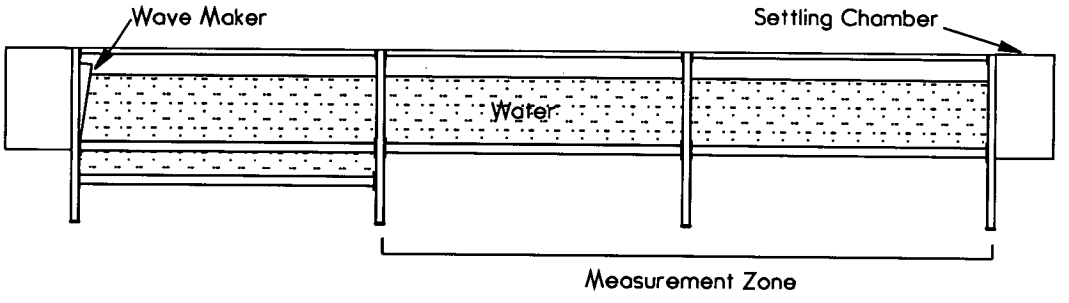

Figure 3.1: The wave tank

As can be seen in figure 3.1 there is a deeper section at the wave maker end. This is to allow the introduction (or extraction) of a current, the settling chamber at the other end being the other current output (or input) point. As no current was used in these experiments this deeper section was blocked off using a ramp from the bottom of the wave maker to the surface of the beach at its foot, thus avoiding a sharp step between the foot of the beach and the base of the tank. The wave maker is a hinged absorbing paddle made by *Edinburgh Designs Ltd* based on an initial design by Salter (1982). It has a force and velocity transducer built in to measure the reflected wave component on the wave maker and subtract this from

the outgoing wave signal. The wave maker is driven by an Acorn Archimedes computer which is also used to provide a trigger signal for the camera shutter, so that the desired phases of the wave are photographed.

3.2.2 PIV Equipment

The two sections furthest away from the wave maker form the measurement zone of the tank. The PIV illumination system, described in Chapter 2, is mounted on rails below this part of the tank to facilitate illumination of any part of the measurement zone. The laser is located in an adjacent laboratory and the beam is deflected by several high quality mirrors to the PIV illumination system. These mirrors are attached to special mounts designed so that the angle of the mirror can be finely and accurately adjusted. For reasons of laser safety the beam is enclosed all along the beam path and each of the beam-steering mirrors (on its mount) was enclosed in an anodised aluminium box specifically designed by the author for the purpose. These boxes allowed access to adjust the mirror mount and also provided a light-tight plate for fastening the 1" Copper tube used to enclose the beam. A telescopic beam enclosure was built and attached to the front of the PIV illumination system to allow movement of the system without exposing the laser beam. Alignment of the rails under the tank was carried out with great care to ensure that they were parallel to the tank, and level so that the laser beam introduced from the wave maker end of the tank would always hit the small deflecting mirror at the entrance to the scanning beam system (see figure 2.1).

The best method of deflecting the beam around the laboratory is currently to use high quality laser mirrors, although enclosing the beam is seldom easy. Copper tubing is used to enclose the beam and as the beam path travels across the floor of the lab, a "sleeping policeman" has been constructed to cover this. Although the optics are well aligned, transfer of the beam from one experimental set-up to another often requires slight adjustment of the beam-steering mirrors. The use of fibre optics to introduce the laser source to the illumination system is the obvious

next step, although there are problems which have to be overcome. The high laser power required for PIV cannot easily be tolerated with mono-mode fibres. In a recent test at Edinburgh a 3.0μm mono-mode fibre melted when 4W of laser power was launched into it (Earnshaw, 1993). The problem with using multi-mode fibres lies in recollimating the emerging beam, an important requirement for PIV.

3.3 Beach Construction

As mentioned in Chapter 1, the main part of this project was to examine the effect of shingle beach profiles on an incoming wave field. An important part of this is the ability to model the beach profiles accurately from the coordinates supplied by HR Wallingford. There is one further requirement placed on beach design as PIV is to be used. This is due to the fact that the laser beam illumination enters the tank through the bottom and consequently has to pass through the beach. For this reason a transparent strip running down the centre of the beach has to be incorporated. The beach is made in two longitudinal halves, separated by a 1cm gap. The gap is then covered with thin transparent plastic. This enables the shape of the beach to be maintained whilst providing the optical access necessary.

3.3.1 Beach Support Structure

As several beach profiles were to be modelled, a common supporting structure was designed. This was based around two pairs of fibre-glass "I" beams approximately 3m long, one pair in each of the two measurement sections of the tank. Fibre-glass was used because of its strength and weight, coupled with the fact that it does not corrode in water. All the metal attachments were made from anodised Aluminium and the fastenings were all stainless steel. The beach was supported in three places; at the foot, mid-point and at the top. The top support rested on rails on the top of the tank and the height of the beach could be varied via a length of screwed rod. This support is shown in figure 3.2.

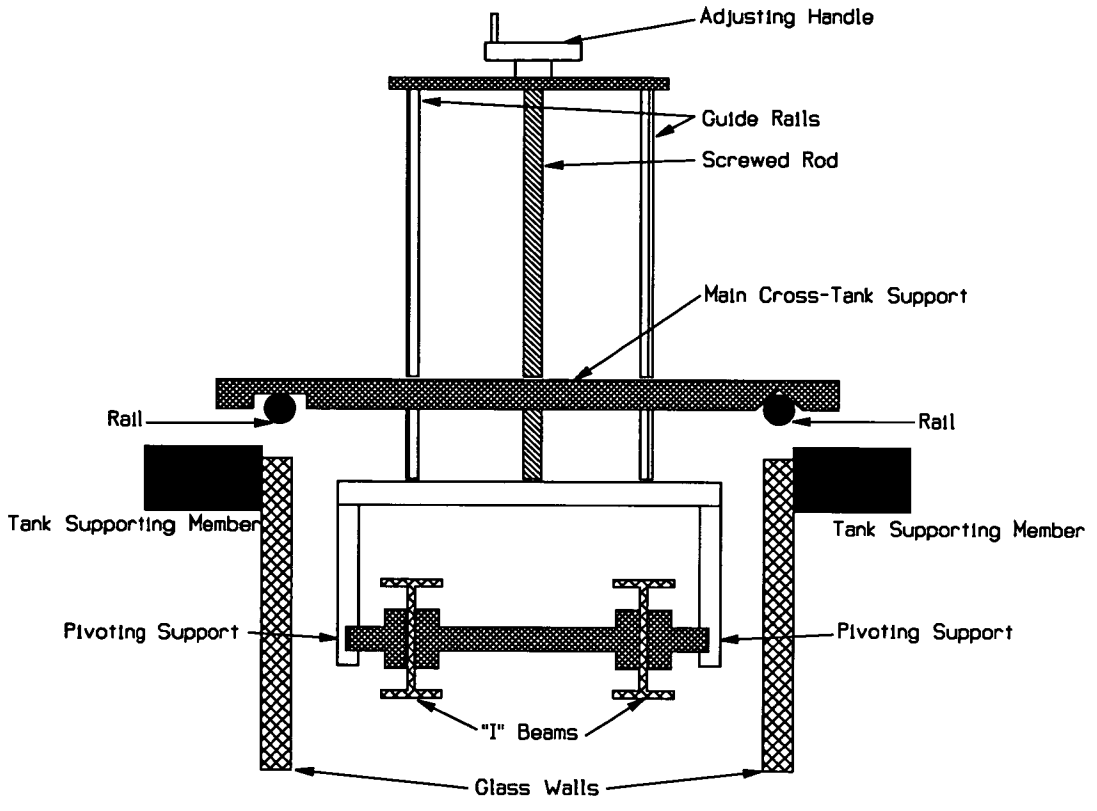

Figure 3.2: The adjustable top support (Vertical Section)

The supports at the foot and mid-point were fitted into "U" channel grooves in the side of the tank, between the panes of glass at the main support members of the tank, as shown in figure 3.3.

All the supports were made of anodised Aluminium. The height of these two supports could be varied continuously over the whole height of the tank. They were held in place by tightening them against the main tank supports. This was achieved by constructing the cross support in five sections, the three middle ones being separated by a length of screwed rod. One of these sections had an anti-clockwise thread cut into it so that if the middle section was turned both the end sections would move out (or in). These three sections were made of 1" diameter Aluminium rod, the two outer ones being where the "I" beams were attached, thus the mid-point support acted as a pivot and the gradient of the beach either side of it could be different.

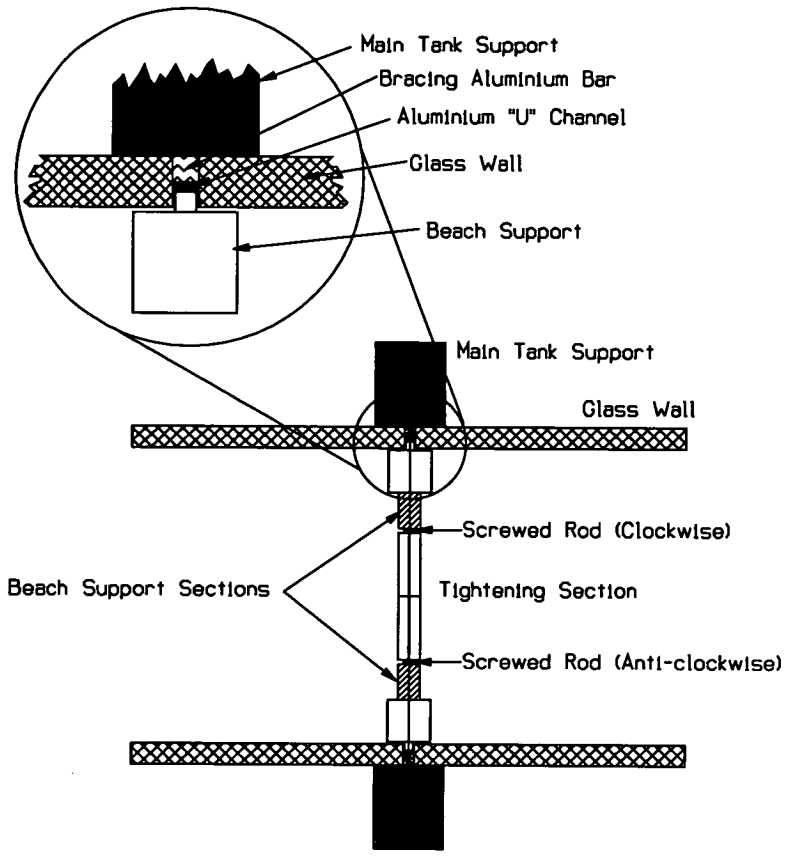

Figure 3.3: A plan view of the beach mid-support in the tank

The support at the foot is held in place in the same way as the mid-point support but it has two Aluminium plates that extend into the tank, each with a slot cut in them, where the "I" beams are attached. This was to accommodate the different horizontal component of length when the beach slope was altered.

Great care was taken to ensure that these supports were installed at the correct height and were horizontal. This was achieved by partially tightening the support in approximately the correct place and then moving it such that one side was at the correct height. The other side was then gently tapped into place until the horizontal, indicated with a spirit level, was reached. The support was then tightened further and the height and level re-checked.

3.3.2 Beach Surface Installation

There were two distinct types of beach modelled in this study, namely plane sloping beaches and profiled beaches. Both of these used the supporting structure described in section 3.3.1, however, the beach surfaces had to be mounted differently. For the plane sloping beaches the surface was mounted directly onto the I beams, being held in place with a series of mounting blocks at 750mm intervals, this is shown in figure 3.4.

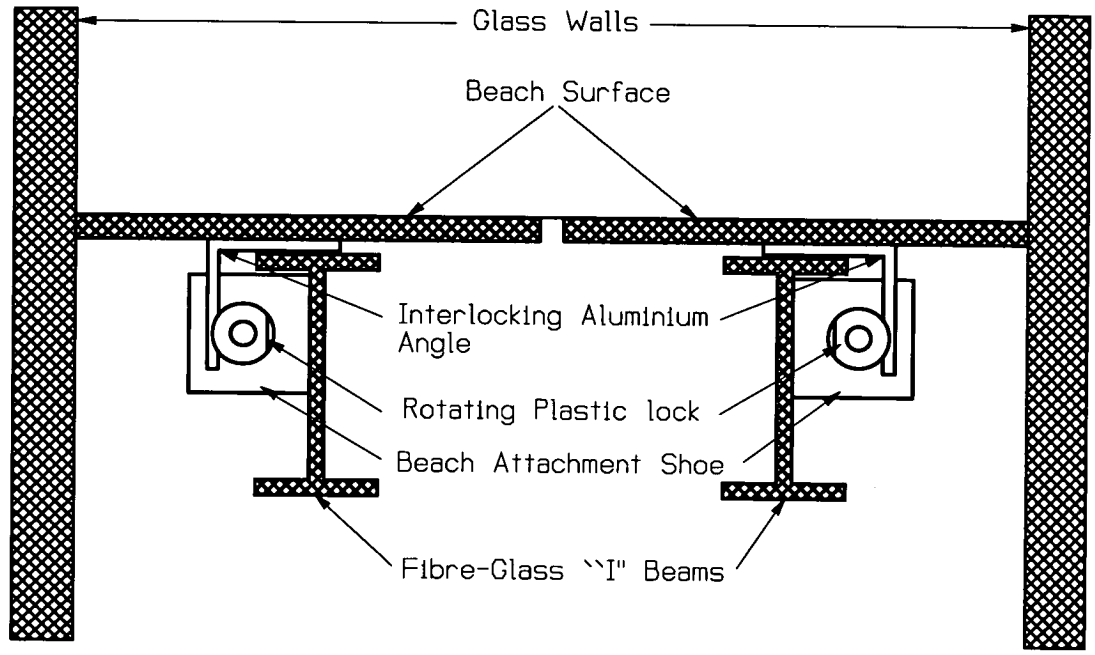

Figure 3.4: A section through the beach showing the attachment blocks

The mounting blocks had a "D"-shaped plastic "lock" which was intended to allow the easy installation or withdrawal of the beach surface. The surface would have small sections of interlocking Aluminium angle attached to the underside which would simply slot into place. A rod connecting the locks on each "I" beam would turn them to hold or release the beach surface. Unfortunately, the tolerances of the machining were too fine and although this worked satisfactorily after manufacture, they would not turn well enough to be used once they had been anodised. For

this reason the beach was screwed down onto the interlocking angle, which was already locked in place.

On the profiled beaches an elaborate adjustable supporting structure was built. It was this structure that was attached to the "I" beams with the mounting blocks shown in figure 3.4. This structure is common to the two beach profiles used for measurements. Individual vertically adjustable supports can be placed at a large number of discrete locations on a length of Aluminium flat bar running the length of each "I" beam. These positions are separated by 4.0cm, however, the height can be continuously adjusted to accommodate the error in horizontal position from that stated in the supplied beach profile coordinates. Once again great care was taken to ensure these individual supports were at the correct height and horizontal. Figures 3.5 A & B show cross-section and side views, respectively, of the profiled beach supporting structure, a photograph of which is shown in figure 3.6.

The beach surface for both the plane and profiled beaches was made from 10mm thick "coplast" plastic sheet. This is flexible enough to follow gentle curves in the beach profile, but rigid enough not to bend under wave motion. In the more complicated profile areas, in and above the swash zone, 3mm thick perspex was used. This was carefully bent into shape with a hot-air gun. Additional support for the beach surface was provided by lengths of anodised Aluminium "T" section which connected the tops of the adjustable supports at the pivot bar shown in figure 3.5.

Photographs of one of the beaches are shown in figures 3.7 & 3.8, where one can also see the scanning laser beam and photographic set-up, in addition to this is a diagram shown in figure 3.9.

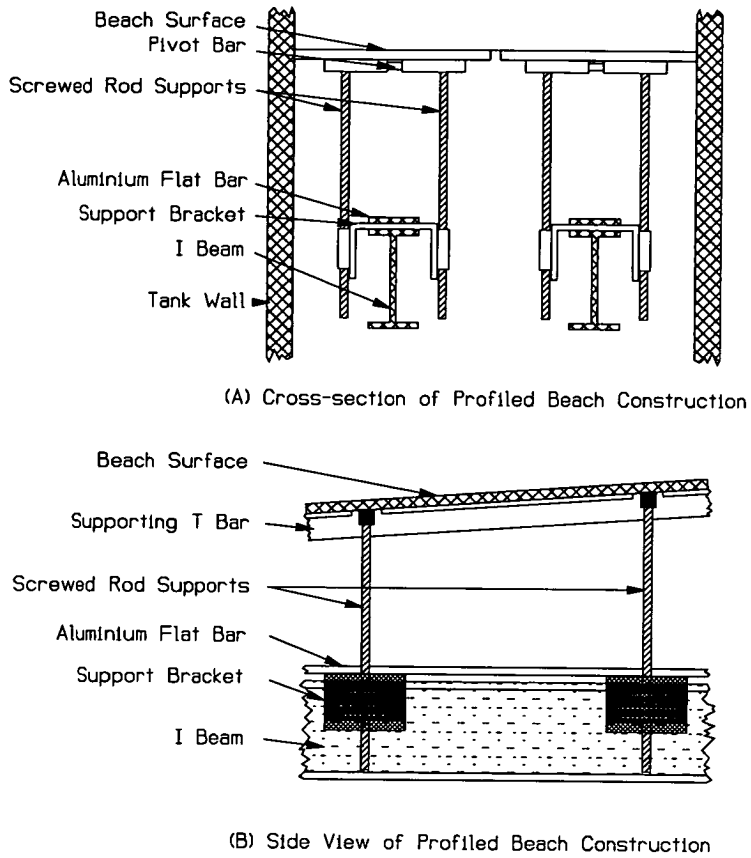

Figure 3.5: The profiled beach supporting structure

3.3.3 Experimental Facilities at The University of Florence

The tank at Edinburgh is only 9.75m long, and this is too short to allow very shallow beaches to be used. In order to make measurements on a 1:100 beach slope the 50m wave flume of Florence University in Italy was used in a collaborative study. Dr. Marco Petti of Florence University had carried out a series of tests with wave gauges to measure the surface profile elevation at different positions along the beach for both regular and irregular waves, however, it was desired to use PIV for velocity measurements of regular waves. The wave tank and the wave gauge layout for the PIV experiments are shown in figure 3.10.

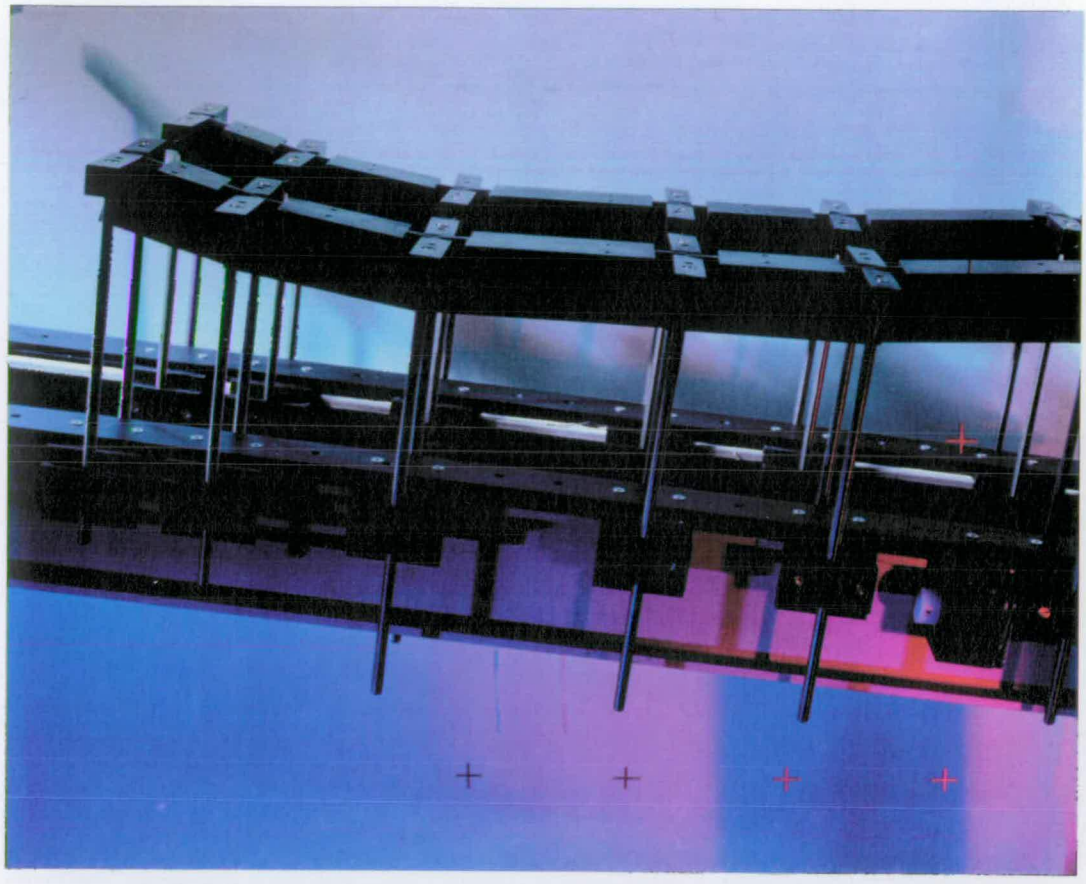

Figure 3.6: The profiled beach structure

In order to perform the PIV experiments, a 15W laser with its associated electronic and cooling systems, and a PIV scanning beam illumination system were taken to Florence. However, the bottom of the wave flume in Florence is not made of glass so the laser beam could not enter the tank in the normal way. To overcome this problem a special 2.4m section of the beach had to be constructed. This PIV beach section is shown diagrammatically in figure 3.11. The beach section had a perspex window along its front side which allowed the laser beam in through the side of the tank, under the beach surface. A 900mm long mirror mounted at 45°, inside the beach section, reflected the laser beam up through a transparent strip in the beach surface into the tank. The PIV beach section was designed by the author and built by the department technicians in Florence.

As there is no PIV analysis system at the University of Florence it was not possible to analyse the results as experiments proceeded. An initial test film was sent to

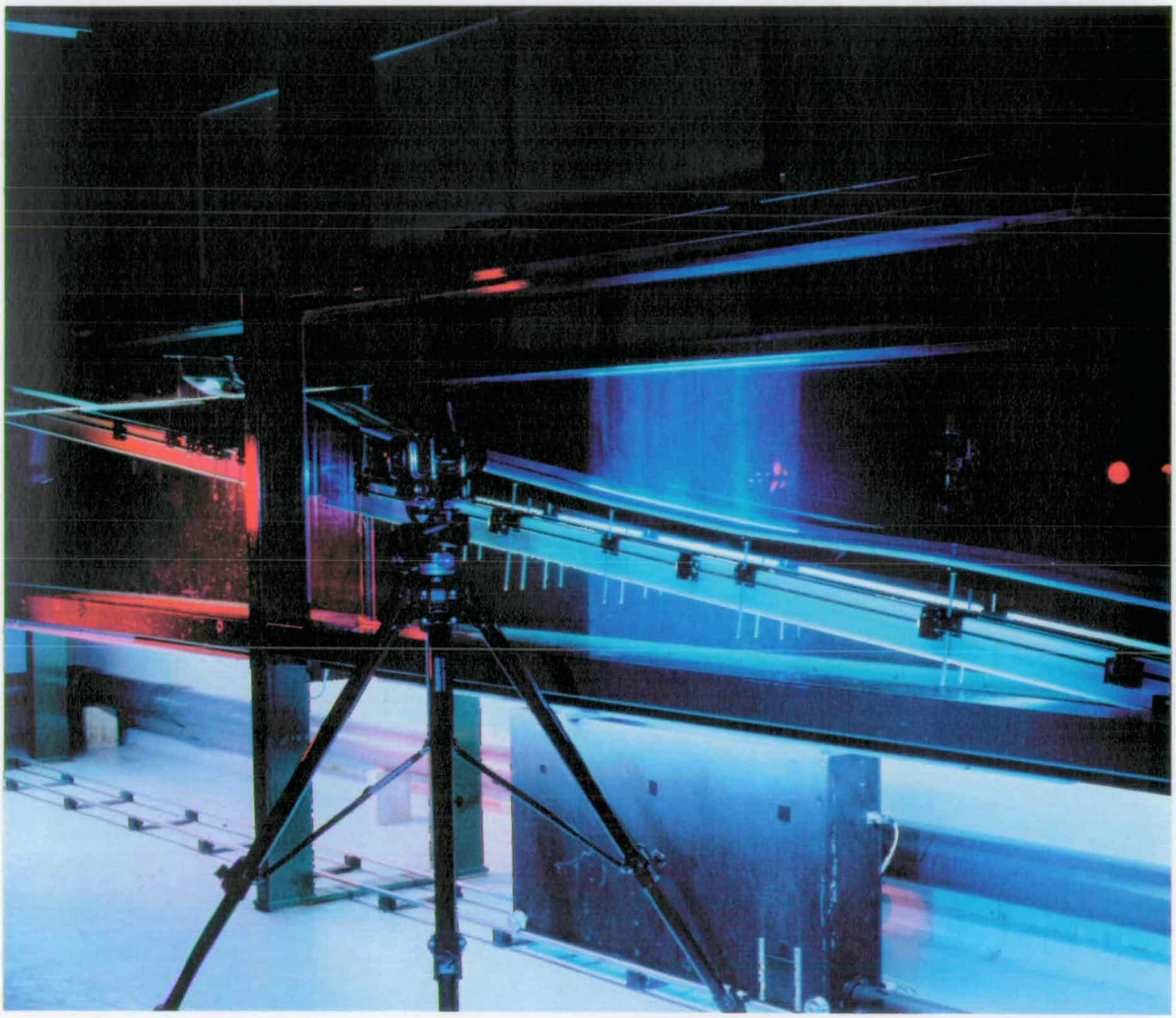

Figure 3.7: A profiled beach

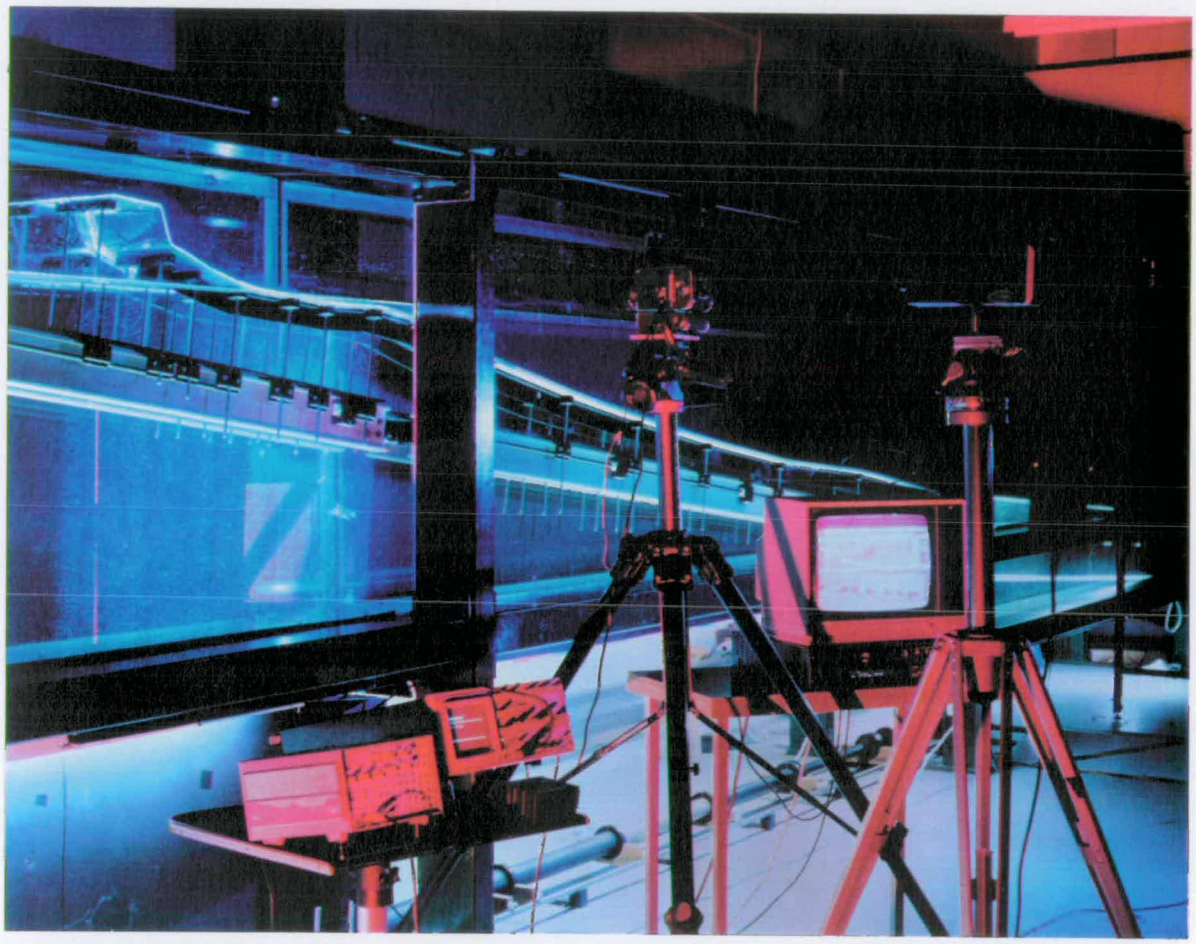

Figure 3.8: A profiled beach

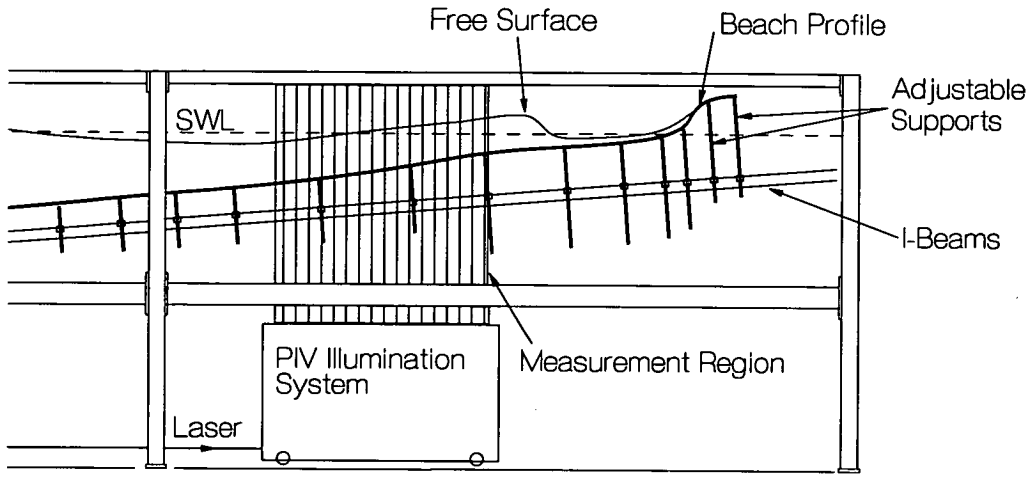

Figure 3.9: The profiled beach

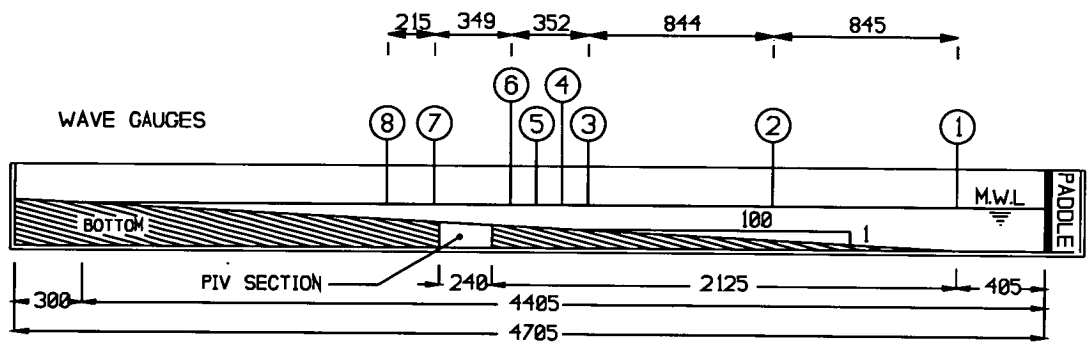

Figure 3.10: The 50m wave flume at Florence University

Edinburgh for analysis to check the quality of the results. However, the formation of Young's fringes by the PIV negatives was checked in Florence on every film by shining a low power Helium-Neon laser through the negative and displaying the transmitted light field on a paper screen. This proved a crude but effective system of ensuring the PIV negatives would be analysable on return to Edinburgh.

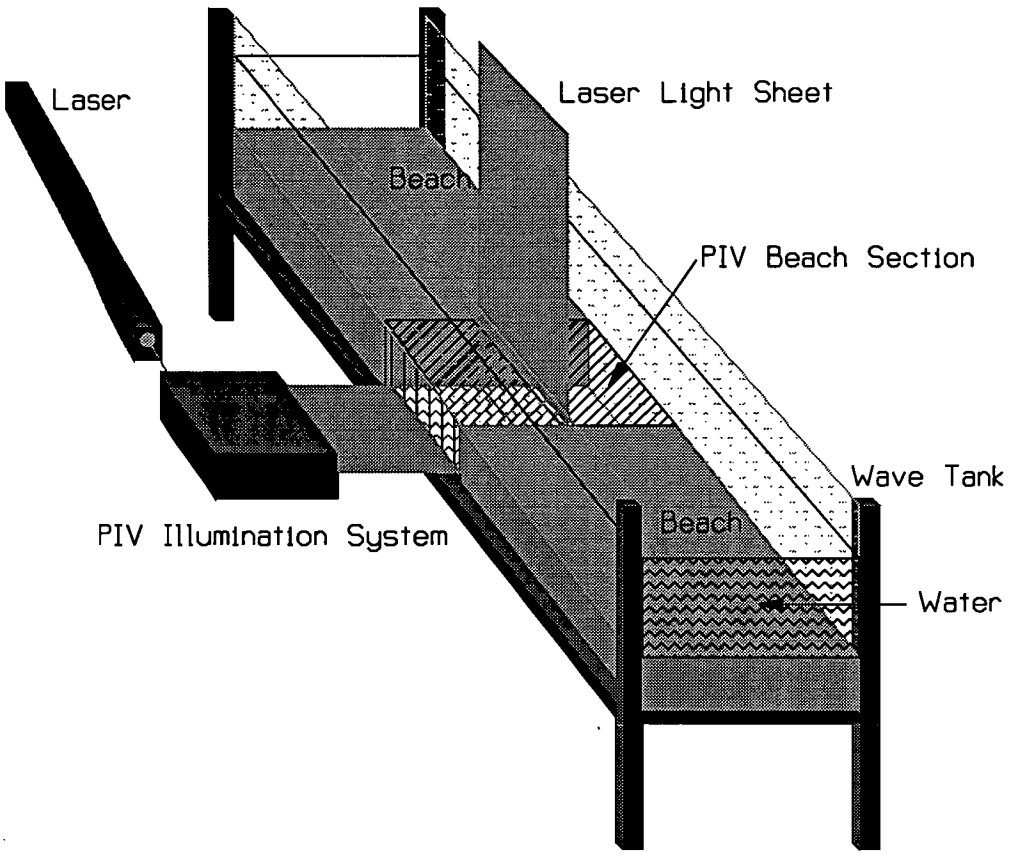

Figure 3.11: The PIV beach section installed in Florence

Chapter 4

Waves Breaking on Mildly Sloping Beaches

4.1 Introduction

In this chapter the experiments carried out on 1:30 and 1:100 beach slopes are described and the results presented. These two slopes are classified as gently sloping and are typical of sandy beaches. It is for these two cases that some theoretical comparisons can be made. For the reasons indicated in section 3.3.3 the experiments on the 1:30 and 1:100 sloping beaches were carried out at the universities of Edinburgh and Florence, respectively, and are now dealt with separately.

4.2 Experiments on a 1:30 Plane Sloping Beach

4.2.1 Introduction

A 1:30 plane sloping beach was installed in the two measurement sections of the 9.75m wave flume at The University of Edinburgh. Due to the restricted length of the flume a 1:30 beach does not reach the bottom of the tank. As we have a hinged paddle (Salter, 1982) rather than a piston-type wave maker, the water depth cannot be altered significantly, so a ramp was installed from the bottom of

the wave maker to the foot of the beach, 3m away, as shown in figure 4.1. The water depth at the foot of the beach was 0.19m and as the waves were so small, (T = 1s, H = 0.032m, L = 1.25m) the arrangement was deemed, if not ideal, then at least satisfactory. The ratio of d/L is $\sim$ 1/7, where d is the still water depth at the foot of the beach and L is the wavelength. This ratio falls between the deep water and shallow water classifications which are d/L $\sim$ 1/2 and d/L $\sim$ 1/20 respectively, making the experimental set up acceptable.

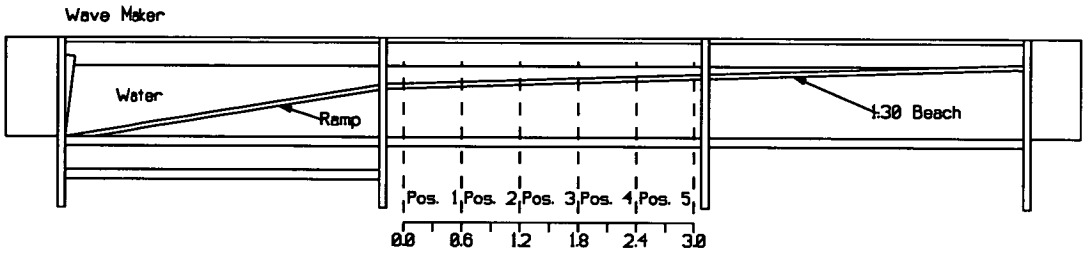

Figure 4.1: The wave tank showing the 1:30 beach and PIV measurement positions.

Although the PIV illumination system can produce a *pseudo* light sheet 1m long, only 0.6m was used in these experiments to obtain a bigger magnification ratio. At a photographic magnification of approximately 1:10 a water depth of 18 cm will appear as 18mm on the film, however, near the breaking point the mean water depth is much lower, resulting in a substantial decrease in the number of 1mm diameter interrogation regions on the negative. The velocity gradient across each interrogation zone also increases with decreasing magnification (see section 2.4), a major problem considering that this is the area of highest accelerations. Neither of these two effects are desirable and consequently the field of view was reduced.

PIV measurements were taken at five positions along the beach approaching the breaking point (see figure 4.1) and four phases of the wave were recorded at each of these positions. The first phase was taken a period of 12s after the wave maker was activated to allow the wave field to become established.

4.2.2 The Boussinesq- and Serre-type Models

The Boussinesq- and closely related Su-Gardner or Serre-type, models have been studied in some depth following the failure of other shallow water wave models to deal with hydrodynamics up to and including the surf zone. Brocchini et al. (1992) gives a good introduction to these models and compares them with various sets of wave height and velocity data. Dingemans (1994a) gives an overview of the different approaches currently being used by several European institutes. In this he explains the test scenario of a submerged breakwater on which all the models are tried. Liberatore & Petti (1992) and Beji & Battjes (1993) describe experiments on such a breakwater to compare with the models. Dingemans (1994a) emphasises the importance of modelling the frequency dispersion accurately if the wave height distribution behind the breakwater is to be modelled correctly; in fact it is the recently improved frequency dispersion terms which have revitalised this relatively old model. Brocchini et al. (1992) have shown comparisons of their models with velocity data provided by the author with some favourable results. Derivation of the Boussinesq and Serre equations is outwith the scope of this thesis. The equations for the velocity distributions used have been derived by Maurizio Brocchini and Michele Drago of Snamprogetti Sp.A, Italy, following on from Peregrine (1967), and it is their Boussinesq- and Serre-type models (*termed simply Boussinesq and Serre hereafter*) which have been used to provide the comparisons shown later in this chapter. However, if one looks at the general nature of these equations there are some substantial limitations on the region of their applicability. The Boussinesq equations are derived from the continuity and Euler equations shown in equations 4.18 & 4.19. Not only do they adopt the relatively standard assumption that the flow is irrotational, inviscid and incompressible, but the Boussinesq model is only valid for *mildly* non-linear waves in shallow water. Specifically they are confined to the limit shown in equation 4.20,

$$\frac{\partial \bar{u}}{\partial t} + \bar{u}\frac{\partial \bar{u}}{\partial x} + g\frac{\partial \eta}{\partial x} = \frac{1}{2}\frac{\partial}{\partial t}[h\frac{\partial^2(h\bar{u})}{\partial x^2} - \frac{h^2}{3}\frac{\partial^2 \bar{u}}{\partial x^2}] \tag{4.18}$$

$$\frac{\partial \eta}{\partial t} + \frac{\partial}{\partial x}[(h+\eta)\bar{u}] = 0 \tag{4.19}$$

$$\epsilon = O(\mu^2) << 1 \tag{4.20}$$

where $\epsilon = a/h$ & $\mu = kh$, a being the wave amplitude, k the wave number and h the water depth. Using the same approach as Su & Gardner (1968) the Euler equations can be expanded up to the order $O(\epsilon\mu^2)$ yielding the Serre equation (equation 4.21) which is valid up to the limit given in equation 4.22.

$$\frac{\partial \bar{u}}{\partial t} + \bar{u}\frac{\partial \bar{u}}{\partial x} + g\frac{\partial \eta}{\partial x} = h\frac{\partial h}{\partial x}\frac{\partial}{\partial t}[\frac{\partial \bar{u}}{\partial x}] + \frac{h^2}{3}\frac{\partial}{\partial t}[\frac{\partial^2 \bar{u}}{\partial x^2}] + h\frac{\partial \eta}{\partial x}\frac{\partial}{\partial t}[\frac{\partial \bar{u}}{\partial x}]$$

$$+\frac{2}{3}h\eta\frac{\partial}{\partial t}[\frac{\partial^2 \bar{u}}{\partial x^2}] + \frac{h^2}{3}\frac{\partial}{\partial x}[\bar{u}\frac{\partial^2 \bar{u}}{\partial x^2} - (\frac{\partial \bar{u}}{\partial x})^2] \tag{4.21}$$

$$\epsilon = O(\mu) < 1 \tag{4.22}$$

Therefore, the Serre equations are valid for higher waves although they are still confined to shallow water. The way both models deal with the velocity field is the second and perhaps more important shortcoming. To start with, both are one-dimensional models; only the depth-averaged horizontal velocity component can be explicitly derived by the models. If one is to obtain a velocity distribution vertically up through the wave, for the horizontal component, then a separate formula has to be used. The generally accepted approach is to impose a parabolic velocity profile; the equation used in this study is shown in equation 4.23 (Brocchini et al., 1992) where z is the vertical coordinate, the bottom being defined as $z \equiv -h$, and the subscript $_{xx}$ denotes the second partial derivative with respect to x.

$$u(z) = \bar{u} - \frac{h}{2}(h\bar{u})_{xx} + \frac{h^2}{6}\bar{u}_{xx} - z(h\bar{u})_{xx} - \frac{z^2}{2}\bar{u}_{xx} \tag{4.23}$$

The only way of gaining any vertical velocity components is to take the divergence of equation 4.23, resulting in equation 4.24 with third order partial derivatives in x.

$$w(z) = -(h\bar{u})_x - z[\bar{u}_x - \frac{h}{2}(h\bar{u})_{xx}]_x + (\frac{h^2}{6}\bar{u}_{xx})_x + \frac{z^2}{2}(h\bar{u})_{xxx} + \frac{z^3}{6}\bar{u}_{xxx} \tag{4.24}$$

The purpose of this study is to examine how good the parabolic distribution is when compared to actual measurements. This is done by calculating the depth-averaged mean horizontal velocity components and their second order spatial derivatives every 5 cm along the wave from the PIV vector maps. These values are used in equation 4.23 and the resulting parabolic profile compared with the actual measured profile. The assumption here is that the best fit parabolic profile will be obtained by using the actual depth-averaged horizontal velocities rather than those predicted by the Boussinesq and Serre models. Alternatively, if the models predicted the depth-averaged velocity distribution perfectly, would they then provide a perfect vertical profile of velocity? In section 4.2.3 these comparisons are shown together with two test cases where the Boussinesq and Serre models have been run. In the latter case the distribution of the depth-averaged horizontal velocity components are compared with the experimental values and then the resulting vertical velocity profiles are shown.

The method of calculating the parabolic profiles is as follows: the depth-averaged horizontal velocity is calculated for every column of vectors on a PIV velocity plot, see figure 4.2 for example. The distribution of the mean velocities can then be plotted, eg. figure 4.3, in order to calculate the second derivatives, $\bar{u}_{xx}$ and $(h\bar{u})_{xx}$.

Because the standard deviation in calculating the mean velocity for every column of vectors was the same order of magnitude as the difference between the means

at adjacent positions, the actual values of $\bar{u}$ could not be used to calculate the second derivatives by a straightforward differencing method; this would give vastly erroneous values, especially when one considers the small value of dx (= 0.01). In order to smooth out this essentially statistical fluctuation, a fifth order least squares polynomial or a fifth order spline curve was used to calculate $\bar{u}_{xx}$ and $(h\bar{u})_{xx}$; this is also shown in the graphs of the mean velocity distributions and as the fit is so good it is not thought to introduce any significant errors. To underline this point the distributions of $\bar{u}_x$ and $\bar{u}_{xx}$ are shown in the same figures and these can be seen to be, in general, smoothly varying quantities confirming the validity of the approach. The profiles could then be calculated from equation 4.23.

4.2.3 1:30 Beach Results

The results are presented for all positions of one phase of the wave in the following format: the PIV vector map is shown then the graph of mean horizontal velocities ($\bar{u}$) and the 1st and 2nd spatial derivatives ($\bar{u}_x$ & $\bar{u}_{xx}$) and finally a set of twelve small graphs showing the calculated parabolic profile with the measured data.

Results from Position 1, Phase 4

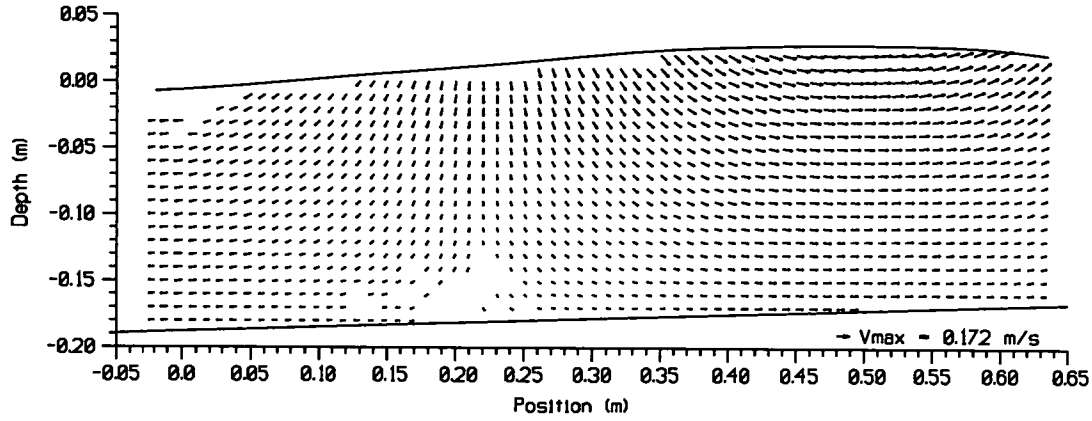

Figure 4.2: PIV vector map: Position 1, Phase 4

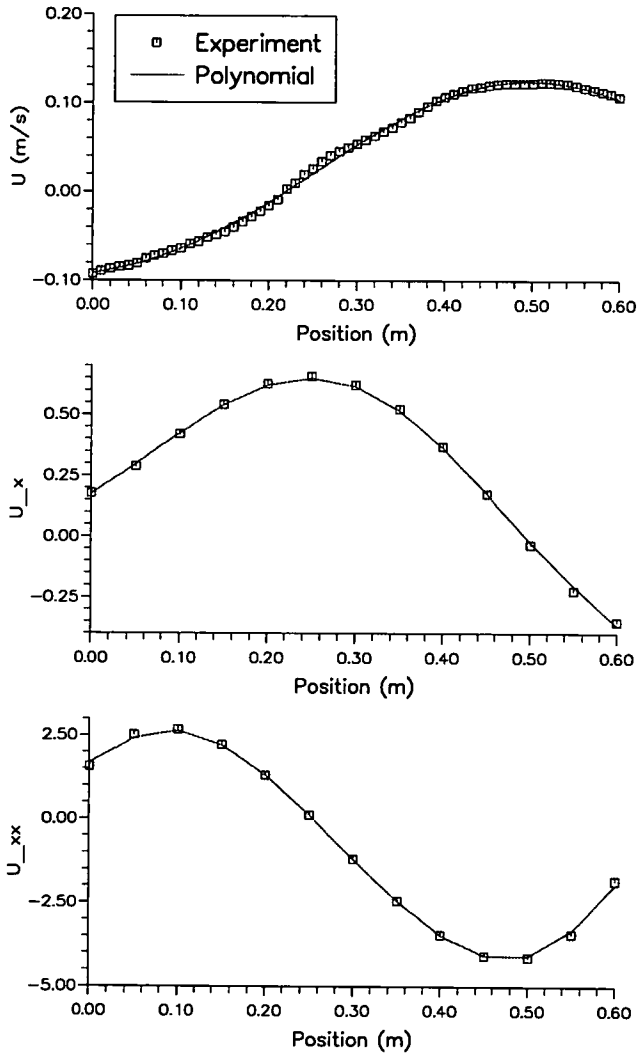

Figure 4.3: $\bar{u}$, $(\bar{u})_x$ & $(\bar{u})_{xx}$ Distributions: Position 1, Phase 4

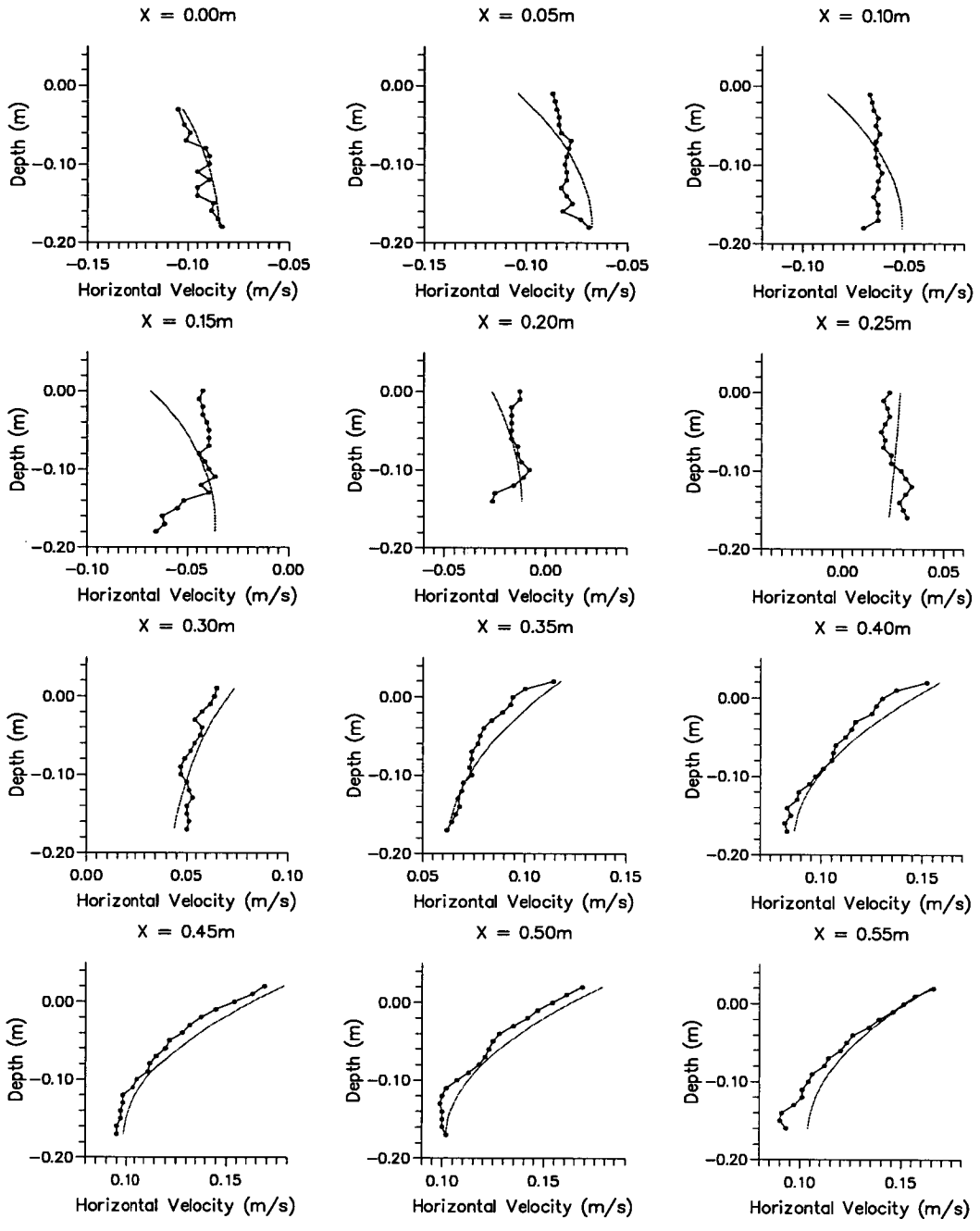

Figure 4.4: Comparison of parabolic profile with data: Position 1, Phase 4. ($h_{x=0.0} = 0.19$m; $h_{x=0.55} = 0.17$m; ($dx = 0.05$m, $dh = 1.67 \times 10^{-3}$m))

Results from Position 2, Phase 4

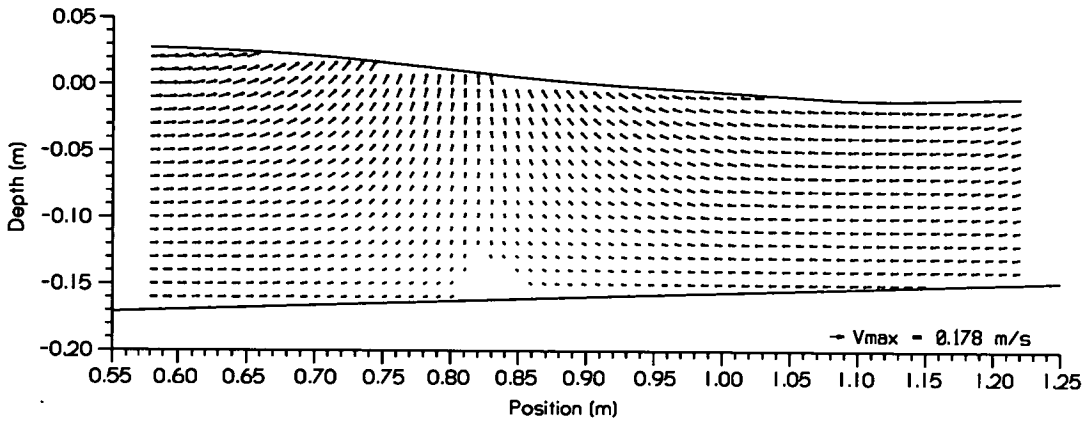

Figure 4.5: PIV vector map: Position 2, Phase 4

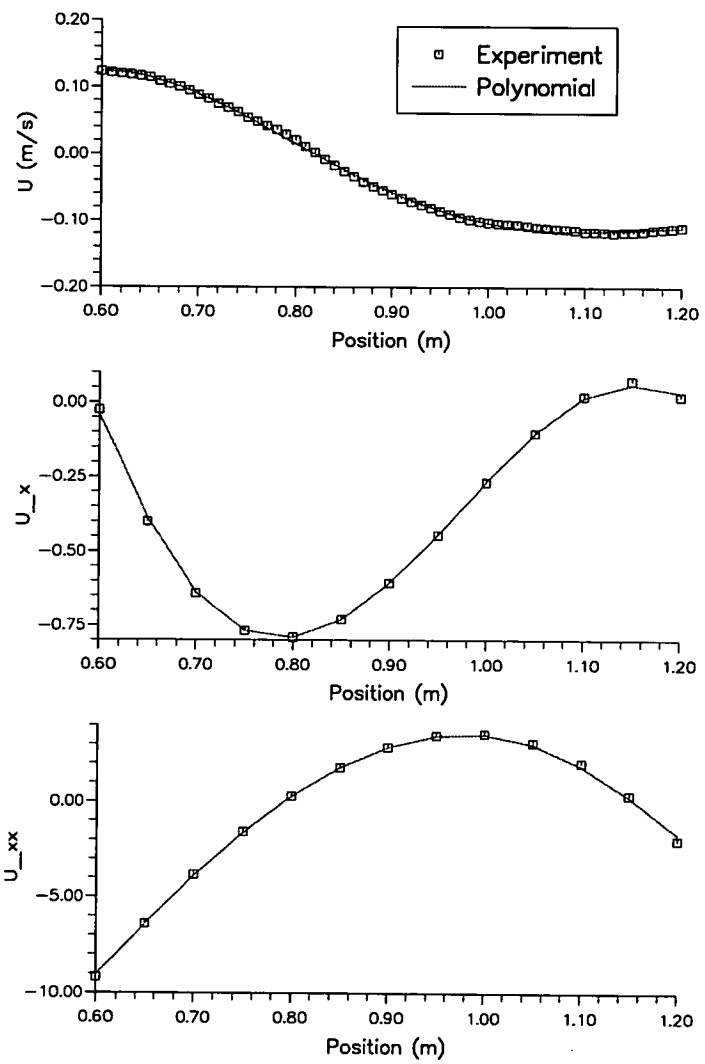

Figure 4.6: $\bar{u}$, $(\bar{u})_x$ & $(\bar{u})_{xx}$ Distributions: Position 2, Phase 4

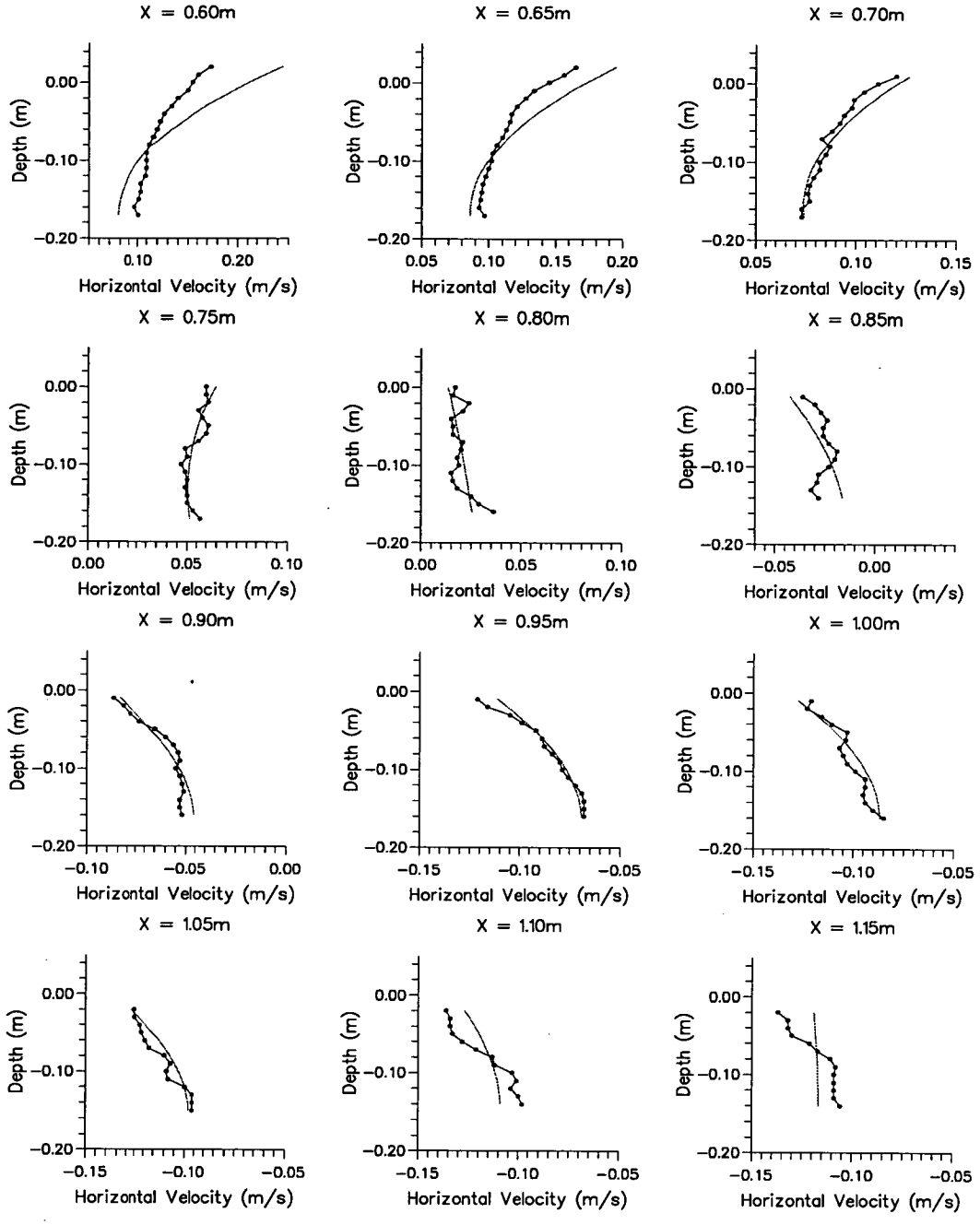

Figure 4.7: Comparison of parabolic profile with data: Position 2, Phase 4. ($h_{x=0.6} = 0.17$m; $h_{x=1.15} = 0.15$m; ($dx = 0.05$m, $dh = 1.67 \times 10^{-3}$m))

Results from Position 3, Phase 4

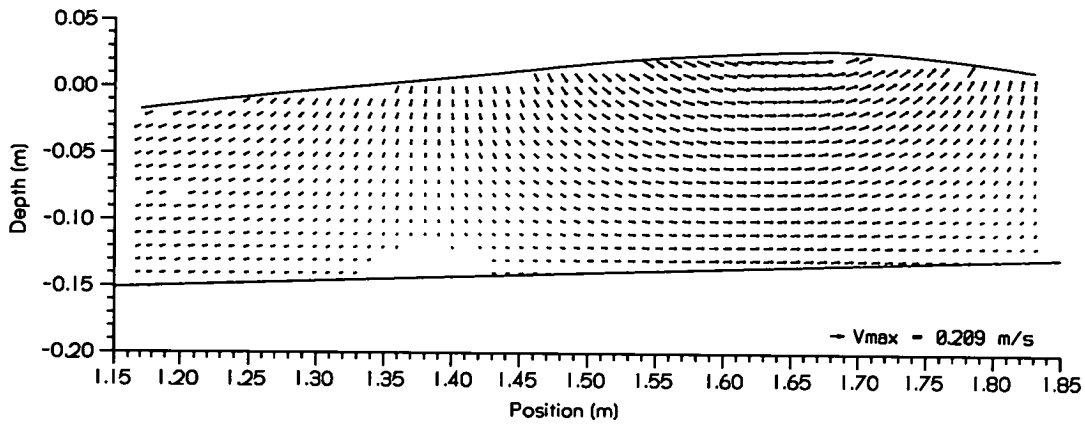

Figure 4.8: PIV vector map: Position 3, Phase 4

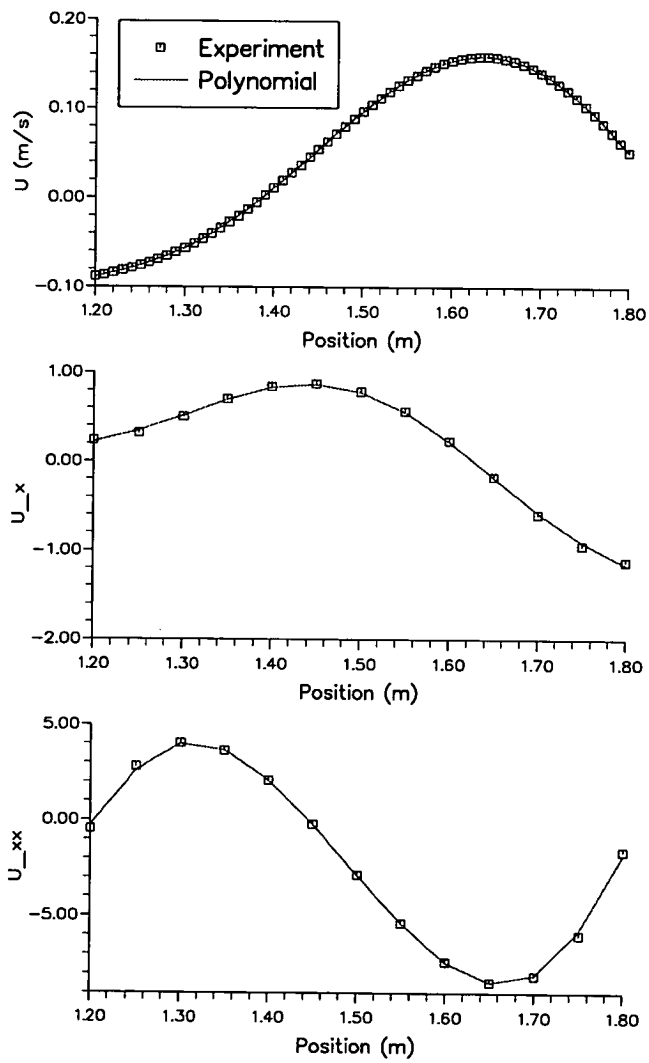

Figure 4.9: $\bar{u}$, $(\bar{u})_x$ & $(\bar{u})_{xx}$ Distributions: Position 3, Phase 4

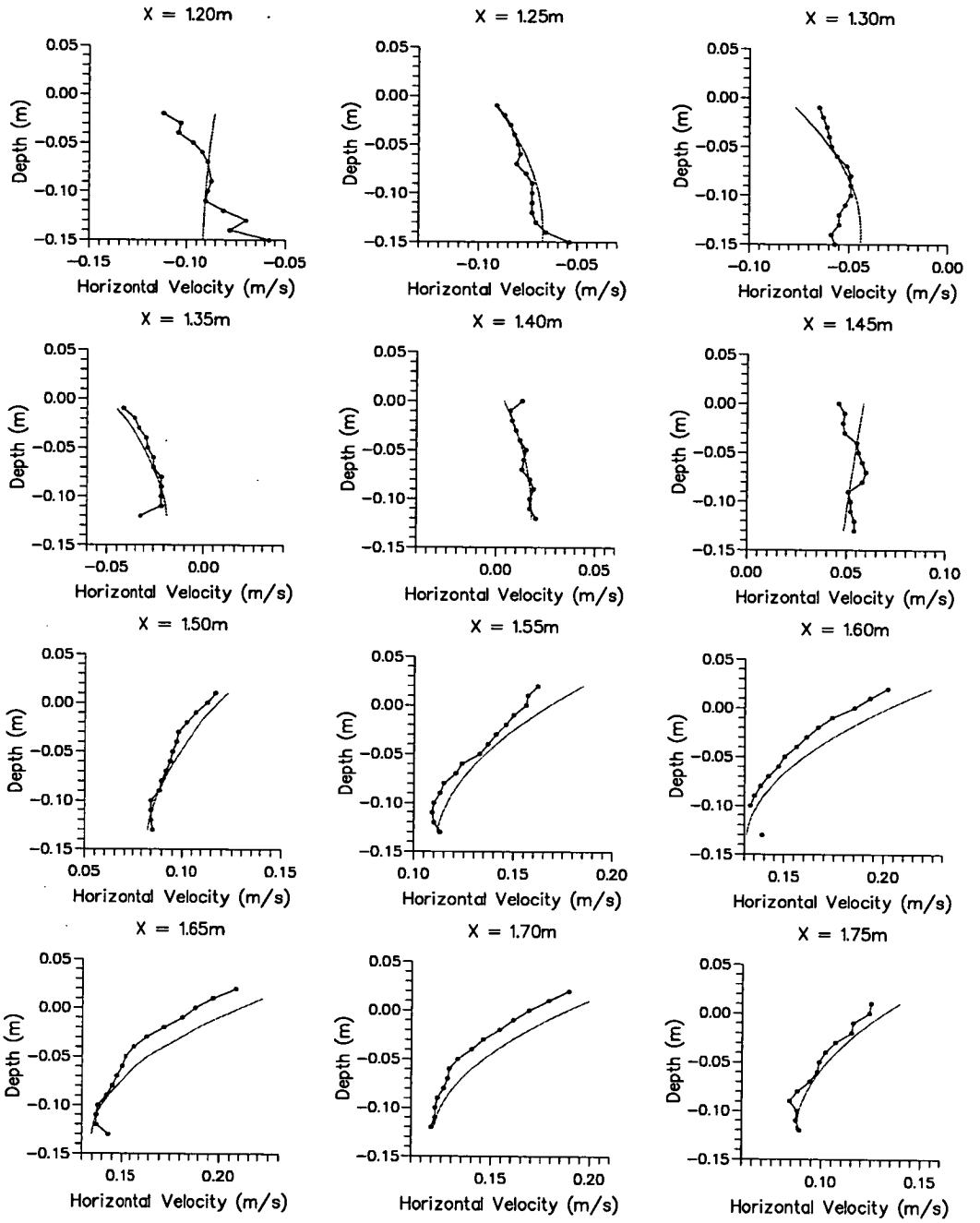

Figure 4.10: Comparison of parabolic profile with data: Position 3, Phase 4. ($h_{x=1.2} = 0.15$m; $h_{x=1.75} = 0.13$m; ($dx = 0.05$m, $dh = 1.67 \times 10^{-3}$m))

Results from Position 4, Phase 4

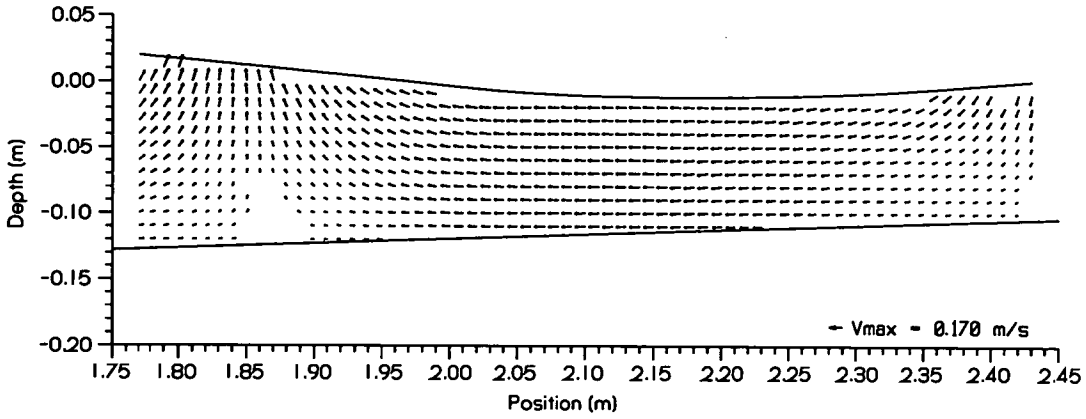

Figure 4.11: PIV vector map: Position 4, Phase 4

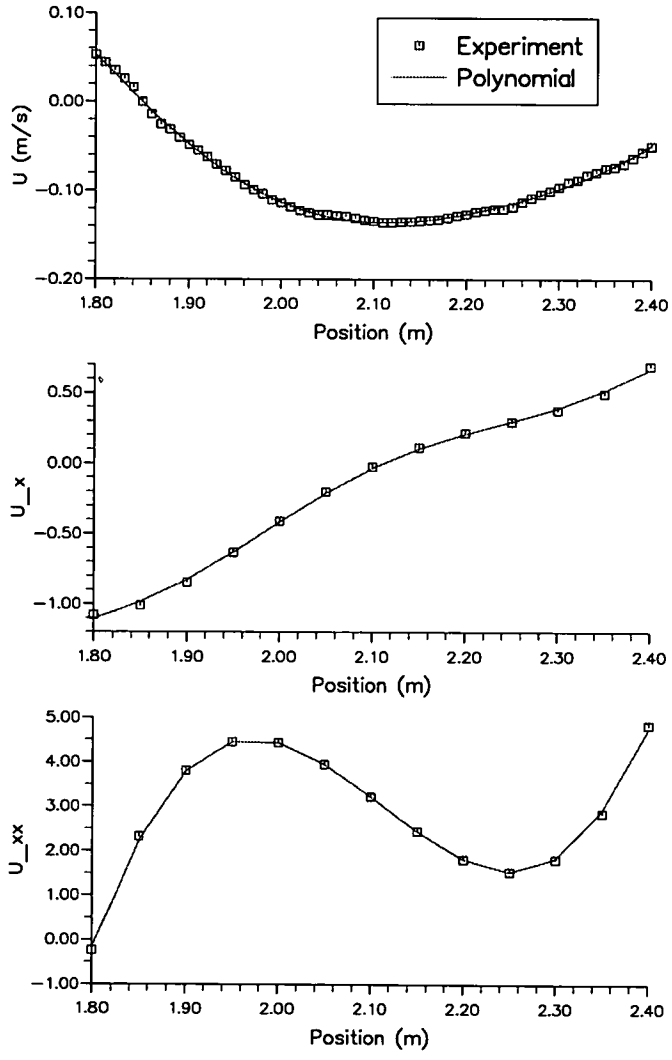

Figure 4.12: $\bar{u}$, $(\bar{u})_x$ & $(\bar{u})_{xx}$ Distributions: Position 4, Phase 4

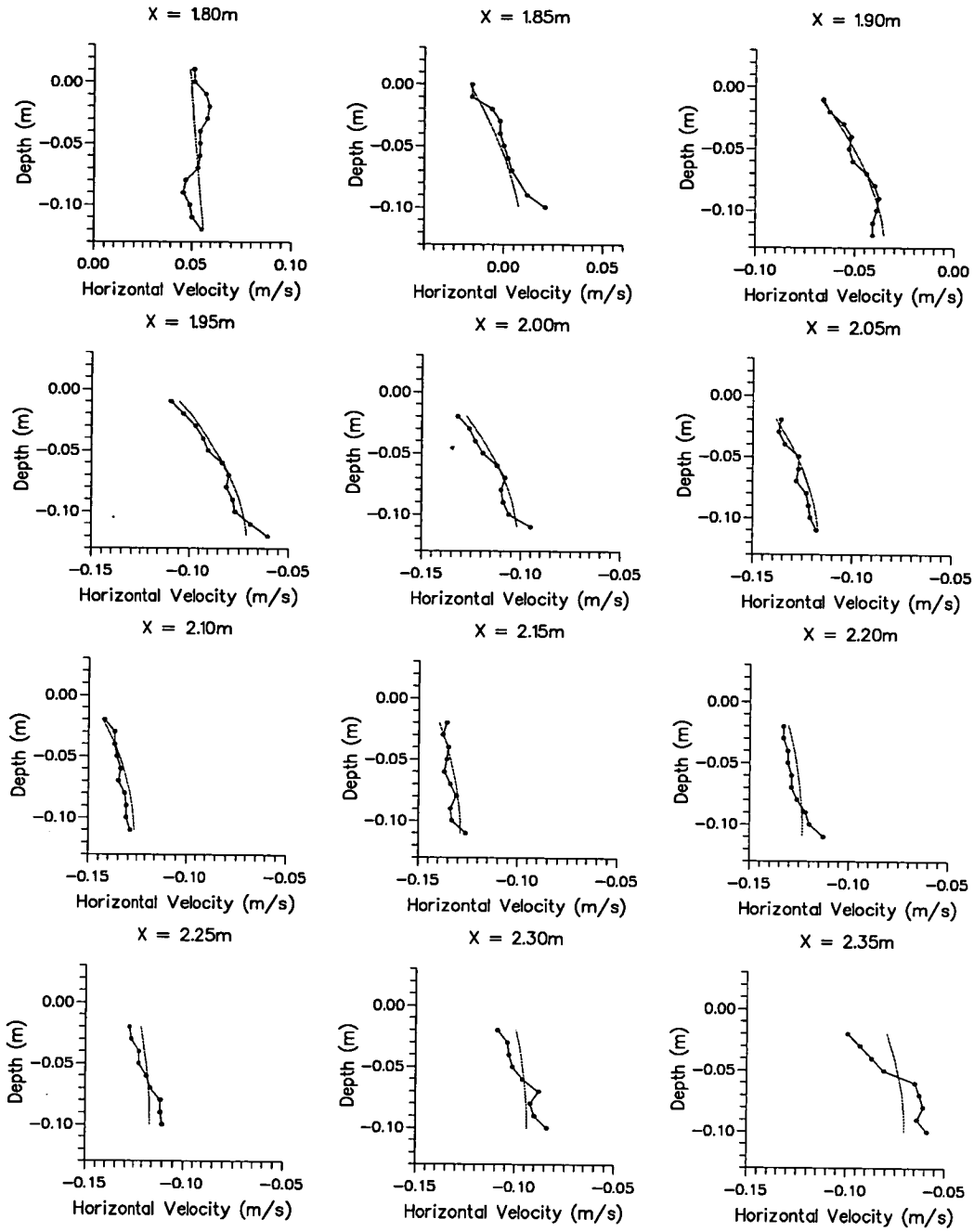

Figure 4.13: Comparison of parabolic profile with data: Position 4, Phase 4. ($h_{x=1.8} = 0.13$m; $h_{x=2.35} = 0.11$m; ($dx = 0.05$m, $dh = 1.67 \times 10^{-3}$m))

Results from Position 5, Phase 4

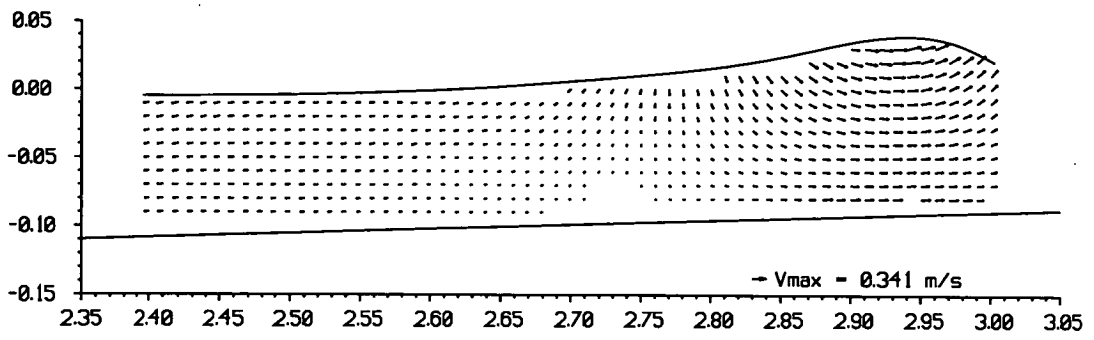

Figure 4.14: PIV vector map: Position 5, Phase 4

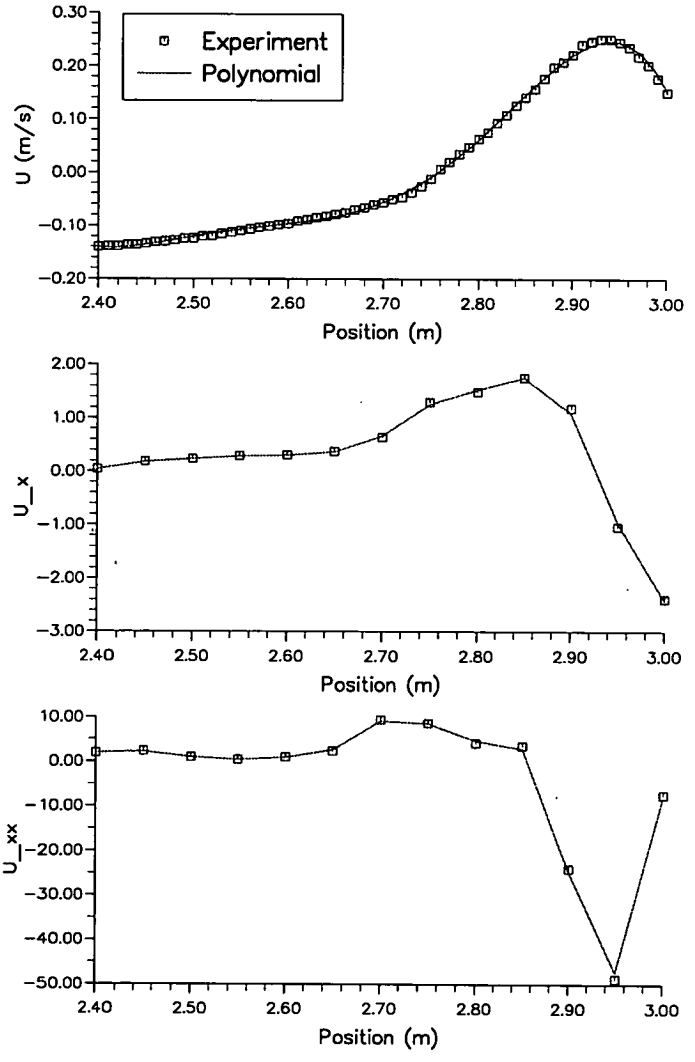

Figure 4.15: $\bar{u}$, $(\bar{u})_x$ & $(\bar{u})_{xx}$ Distributions: Position 5, Phase 4

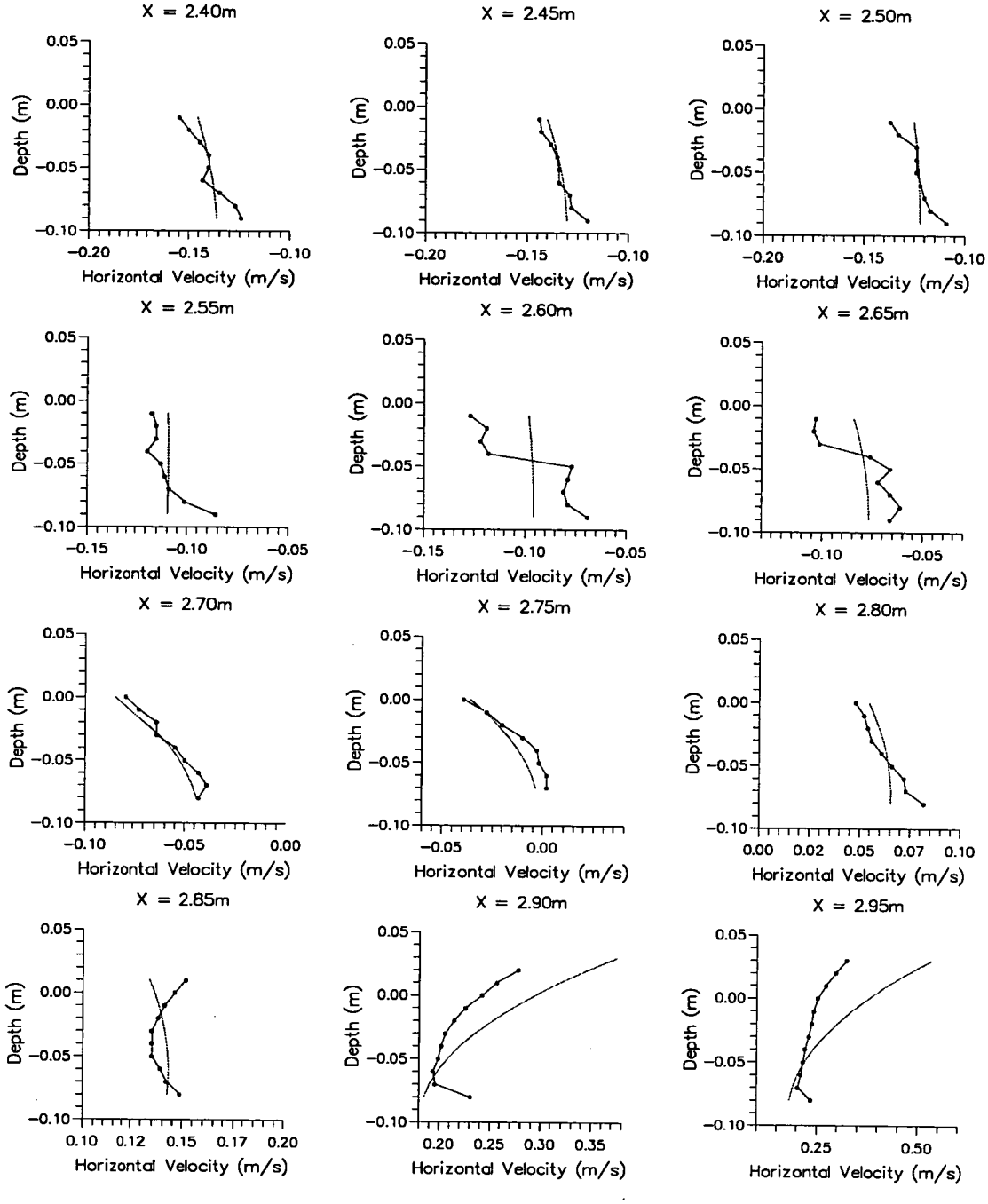

Figure 4.16: Comparison of parabolic profile with data: Position 5, Phase 4. ($h_{x=2.4} = 0.11$m; $h_{x=2.95} = 0.09$m; ($dx = 0.05$m, $dh = 1.67 \times 10^{-3}$m))

Boussinesq and Serre Model Comparisons

Having shown how equation 4.23 fits a parabolic profile to the measured data, it now seems logical to see how well the Boussinesq and Serre models can predict the depth-averaged horizontal velocity.

The Boussinesq and Serre models developed at Snamprogetti, Italy, have been run for the third and fifth measurement positions, the vector maps of which are shown in figures 4.8 & 4.17. The depth-averaged horizontal velocities predicted by the models, along with those calculated from the measured data, are shown in figures 4.18 & 4.19. The subsequent velocity profiles, calculated in the same fashion as before, are shown in figures 4.20 & 4.21.

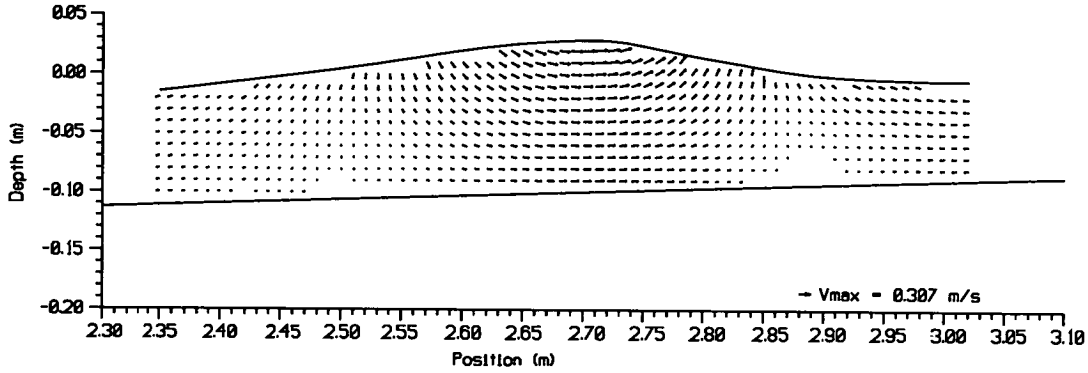

Figure 4.17: PIV velocity vector map: Position 5, Phase 3

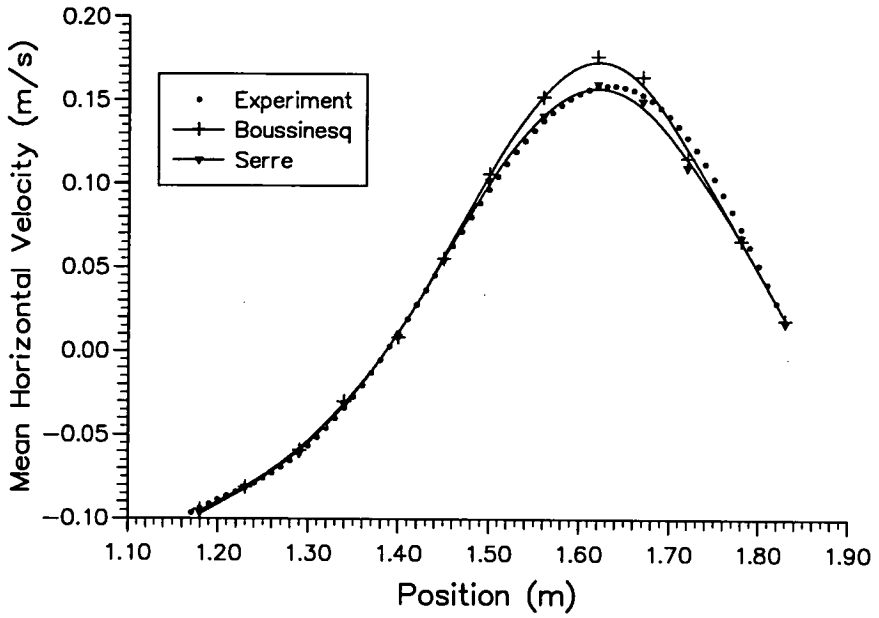

Figure 4.18: Mean horizontal velocities from the models and experiments for Position 3, Phase 4.

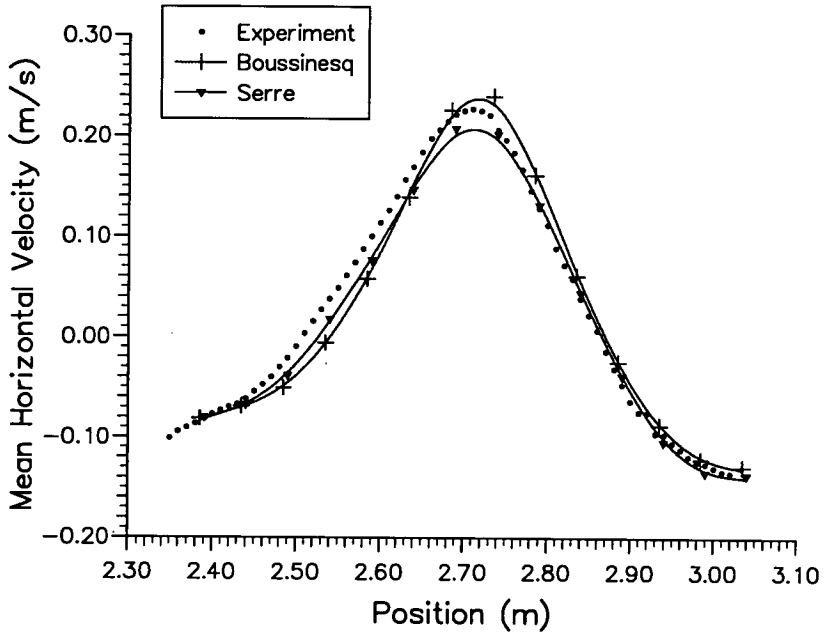

Figure 4.19: Mean horizontal velocities from the models and experiments for Position 5, Phase 3.

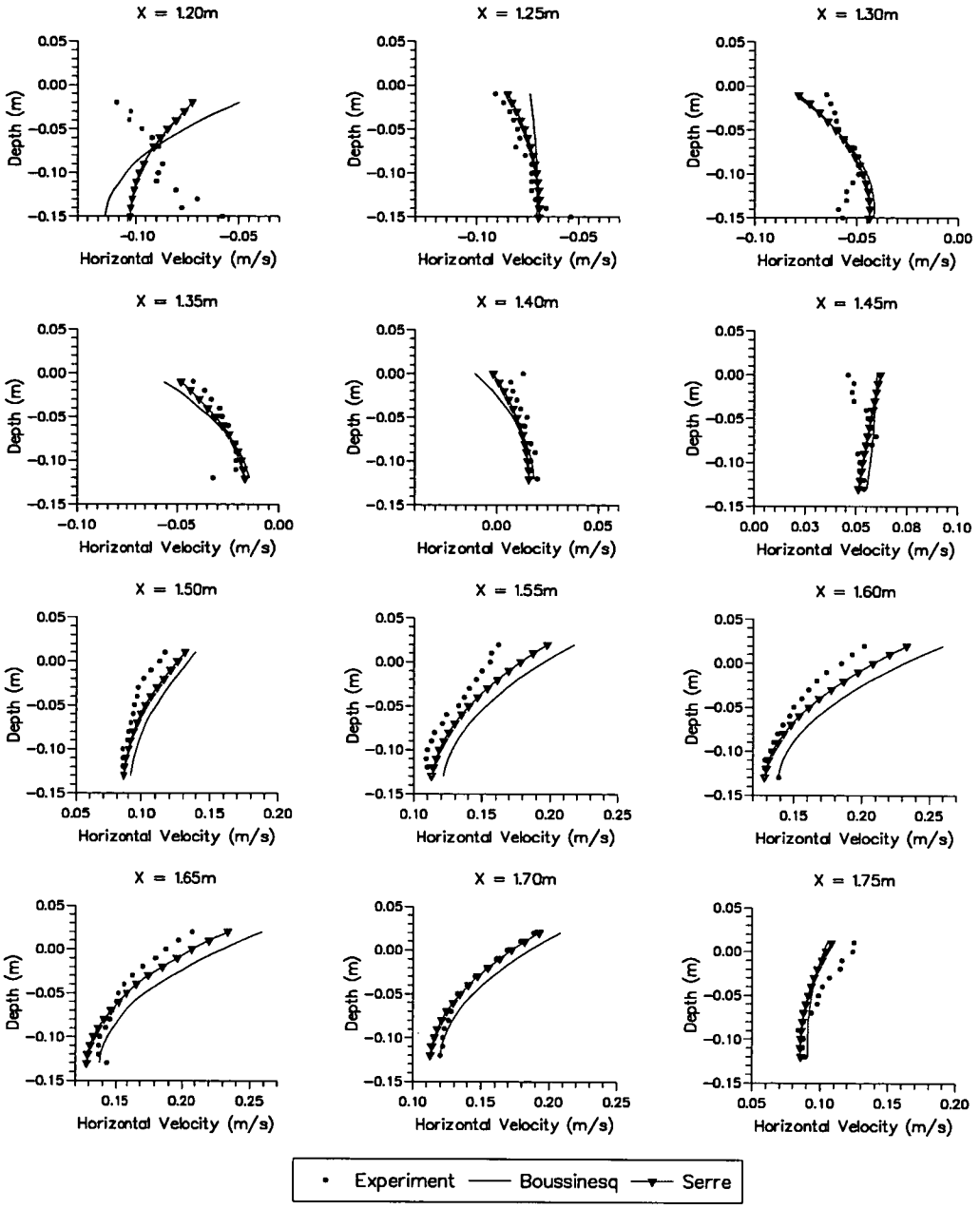

Figure 4.20: Modelled and Measured Velocity Profiles at Different Horizontal Positions (x) in the 1s wave on a 1:30 Beach. ($h_{x=1.2} = 0.15$m; $h_{x=1.75} = 0.13$m; ($dx = 0.05$m, $dh = 1.67 \times 10^{-3}$m))

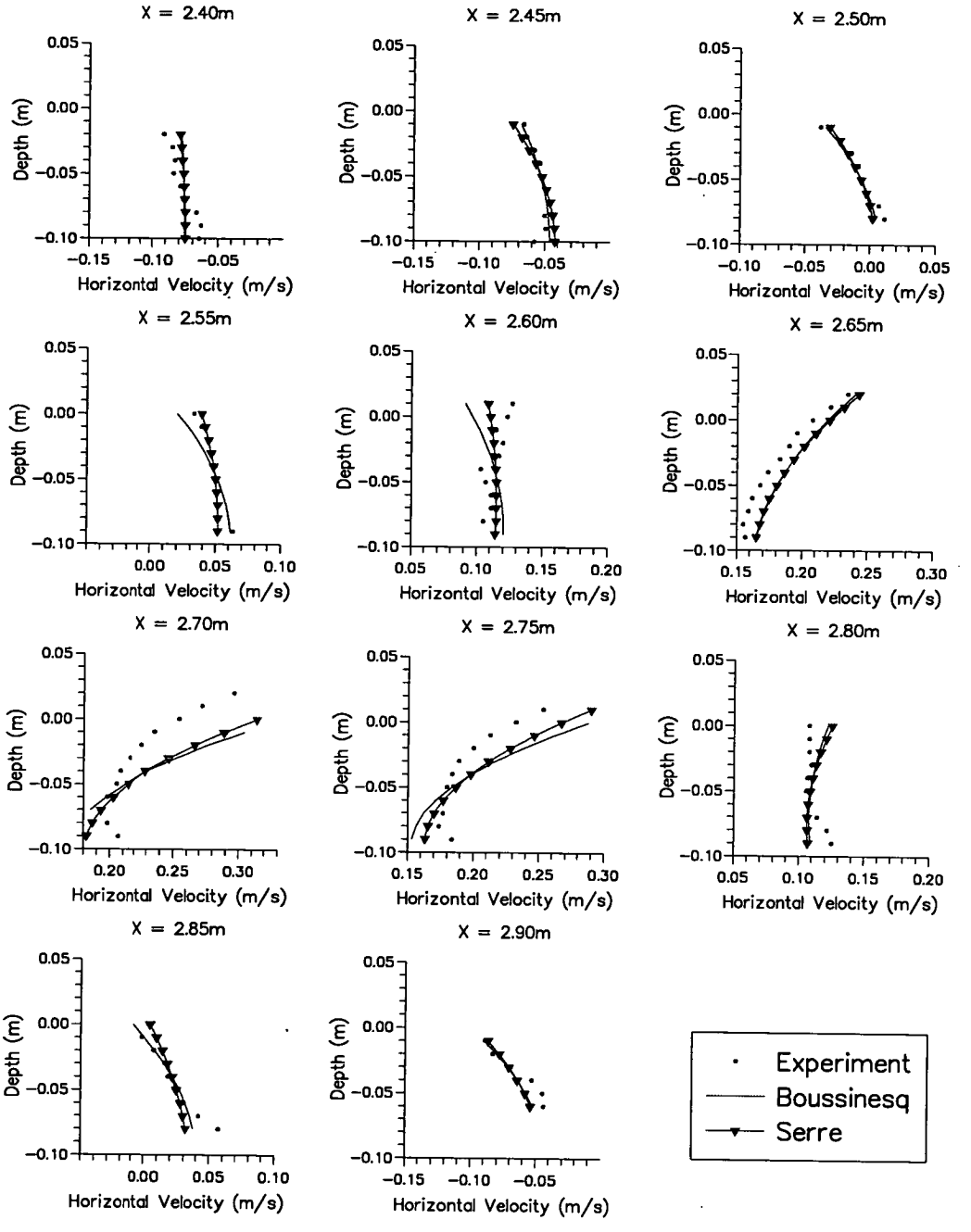

Figure 4.21: Modelled and Measured Velocity Profiles at Different Horizontal Positions (x) in the 1s wave on a 1:30 Beach. ($h_{x=2.4} = 0.11$m; $h_{x=2.9} = 0.09$m; ($dx = 0.05$m, $dh = 1.67 \times 10^{-3}$m))

4.2.4 Comments

In general the comparison of a parabolic profile calculated from experimental values agreed fairly well with the measured profiles. The agreement was particularly good near the bed. Although the use of a least squares polynomial to calculate $\bar{u}_{xx}$ and $(h\bar{u})_{xx}$ appears satisfactory for the vast majority of cases, there were very occasionally errors that arose due to fitting a polynomial approximation at the edges of the data, as can be seen, for example, at $x = 1.20$m in figures 4.10 & 4.20.

There was a consistent overestimate of the measured velocity by the parabolic profile in the near-surface region of the crest of the wave, which appears to get worse as the wave steepens. The degree to which this discrepancy increases with non-linearity is dealt with in section 4.4. One can briefly envisage one of the problems: equation 4.23 is derived assuming the same range of validity as the Boussinesq model ie., it includes terms of order $(kh)^2$, but ignores those of order $(a/h)(kh)^2$, however, as one approaches breaking $a/h = O(1)$ and so the neglected terms are of the same order of magnitude as the included ones.

The trough phase of the wave showed good agreement, in general, between the measured and parabolic profiles. There were, however, a small number of profiles exhibiting some noticeable scatter of the measured profile (see, for example, $x = 2.60$m in figure 4.16), this is most probably due to turbulence generated by wave breaking being transported back offshore in the undertow. It is perhaps worth noting that a parabolic profile cannot incorporate turbulence effects which may have a significant effect on, say, sediment transport (Nielsen, 92, 94).

The comparison of the Boussinesq and Serre model predictions of the depth-averaged horizontal velocity with the measured values shows an overestimate of the peak velocity by the Boussinesq model and a very close estimate for the Serre model at the first position shown. In the second position, further up the beach, the Boussinesq still overestimates the peak value but the Serre now underestimates it. In both positions the models provided a slightly sharper mean velocity distribution

than that given by the measurements. This underestimation by the Serre model is perhaps counter-intuitive considering that it is derived to a higher order than the Boussinesq model and therefore should more accurately predict this steeper, more non-linear wave.

The velocity profiles calculated from the Boussinesq and Serre model predictions did not show particularly good agreement. This is due to the difference between the predicted and measured spatial distributions of the depth-averaged horizontal velocity, and manifests itself by a shift along the x-axis of the models' profiles with respect to the experiment's. The shape of the curves predicted by the models is similar to that of the experimental profiles, but still tend to overestimate the curvature of the parabola leading to an overestimate of the near-surface velocity in the crest region. This indicates the sensitivity of the variable $\bar{u}_{xx}$ because small differences in the predicted and measured distributions of $\bar{u}$ can lead to large differences in the parabolic profile. Only the near-bed velocities were adequately modelled on a consistent basis.

4.3 Experiments on a 1:100 Plane Sloping Beach

The wave tank at Edinburgh is too short to use for beaches with gradients of the order of 1:100, so the 50m wave flume at the University of Florence was used in a collaborative study. Monochromatic waves with a period of 3s and a height of 0.1m were used. The wave maker was of the piston type and although it was fitted with an absorbing system this was found to be inappropriate for regular waves on such a shallow beach slope. A zero-up-crossing wave gauge analysis found that the repeatability of the waves was better with the absorbing system switched off. This was thought to be due to the fact that the short-wave reflection off such a shallow beach slope is very small and the main reflection in the tank is due to a combination of two processes. The first is the generation of low-frequency waves by the waves breaking on the beach (Watson & Peregrine, 1992, Watson et al., 1994) and the second is the seiching motion induced in the tank. Both of

these components have very long periods (of the order of tens of seconds) and the absorbing system has difficulty coping with these low-frequency reflections and in general it was found to be trying to over-compensate for them, creating a wave field which was less repeatable than when the system was switched off.

The scan length of the PIV illumination system used in these experiments was 0.5m. Measurements were taken at four positions in the custom built beach section (described in section 3.3.3) for two water depths, effectively doubling the measurement zone to 4m in length, or the number of measurement positions to eight. Due to technical practicalities it was impossible to trigger the camera from the computer controlling the wave generator, as is normally done in Edinburgh. The triggering was provided by the voltage variation induced in wave gauges as the crest of the waves passed. The voltage variation could be carefully adjusted, by varying the depth of the wave gauge and/or its gain, to just provide enough of a voltage pulse to close a relay switch, triggering the camera. The gauges were separated by a quarter of a wavelength and were adjusted so that the crest of the incoming wave would trigger the camera to photograph the same phase of the preceding wave in the measurement zone, see figure 4.22. The circuit to trigger the camera included a switch so that an individual wave could be selected to trigger the camera. The particular gauge to trigger the camera was selected by manually connecting each one in turn, from a distribution board, into the circuit.

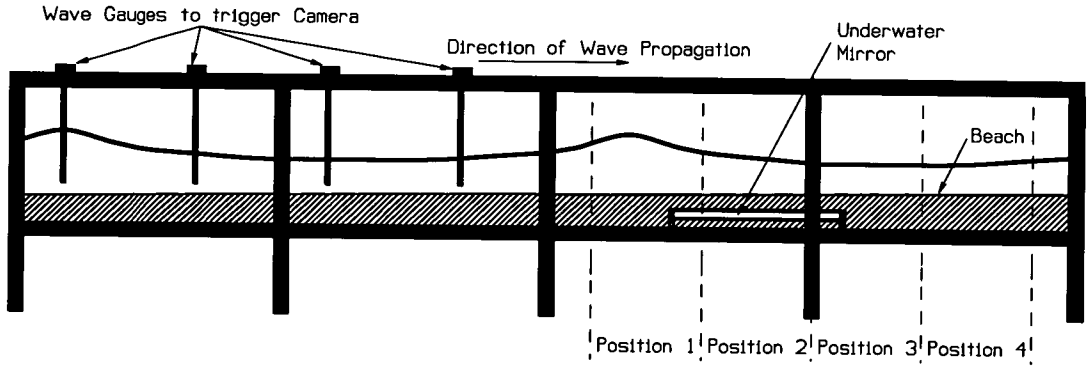

Figure 4.22: The PIV Measurement Section and Camera Triggering Wave Gauges.

This method, coupled with the degree of unrepeatability of the waves, did not provide adequate continuity between different measurement positions at suppos-

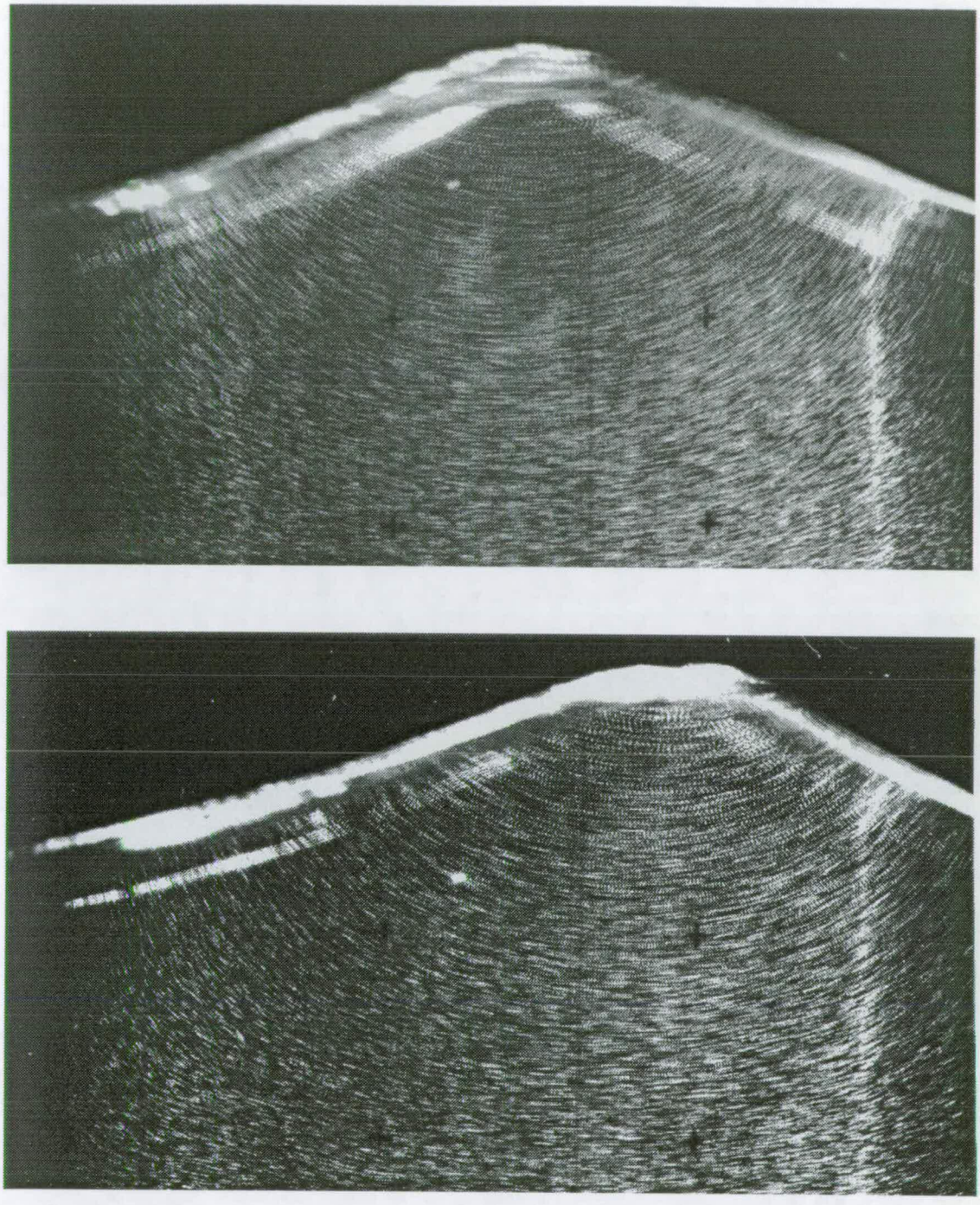

Figure 4.23: Two Waves at Nominally Identical Phases.

edly identical phases. It is the wave repeatability, however, due to the different phases of the long waves, that is the major contributor to this problem. There were several occasions when two exposures were taken of the same phase at a given

position, and they appear markedly different, even to a casual observer. Figure 4.23 show photographs of two waves nominally at identical phases.

For this reason it was impossible to calculate wavelength averaged properties, only velocity characteristics from individual measurements can be shown.

4.3.1 1:100 Beach Results

For brevity, vector maps and parabolic profiles are shown for only four examples of a 3s wave breaking on a 1:100 beach, representing crest and trough phases before and during breaking, at Positions 1 and 5. The method of calculating the parabolic profiles is the same as in section 4.2.3 with the exception that for the two crest phases a fifth order spline fit was used rather than the fifth order polynomial to obtain $(\bar{u})_{xx}$ and $(h\bar{u})_{xx}$ as this provided a better fit for these sharper distributions.

The results are presented in the same format as in section 4.2.3, ie. the PIV vector map is shown then the graph of mean horizontal velocities and the smooth/polynomial fit together with their first and second derivatives (for the crest phases) and finally a set of small graphs showing the calculated parabolic profile with the measured data.

Results from Position 1, Phase 1

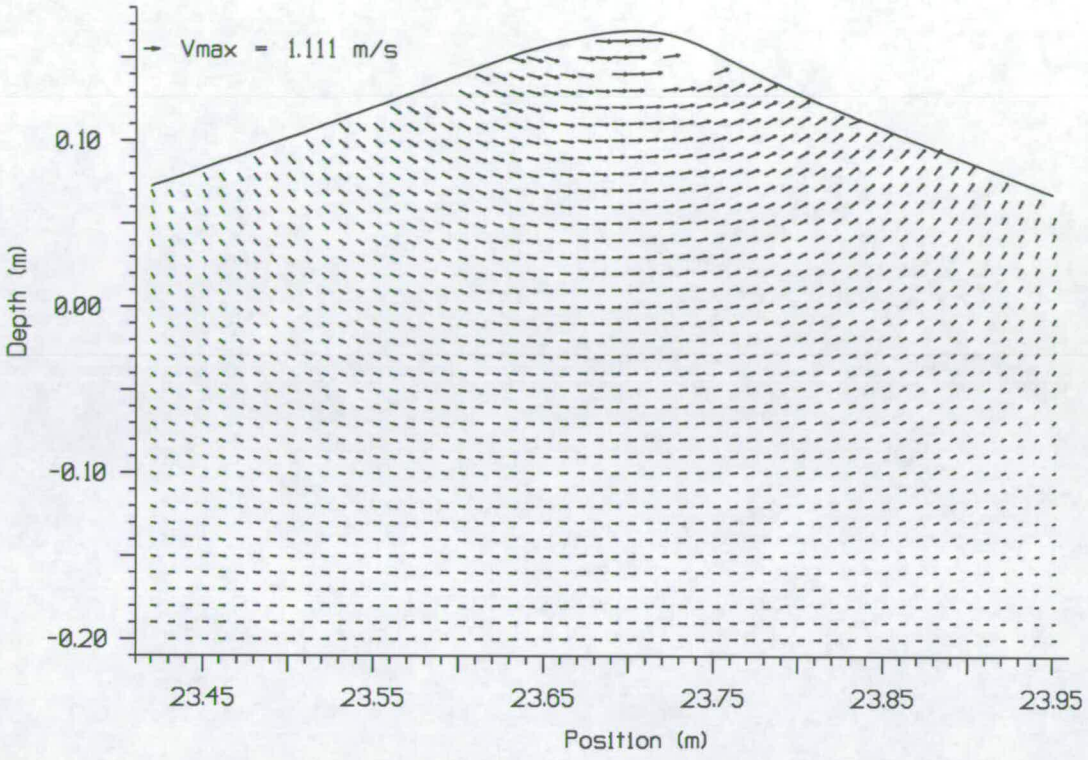

Figure 4.24: PIV vector map: Position 1, Phase 1

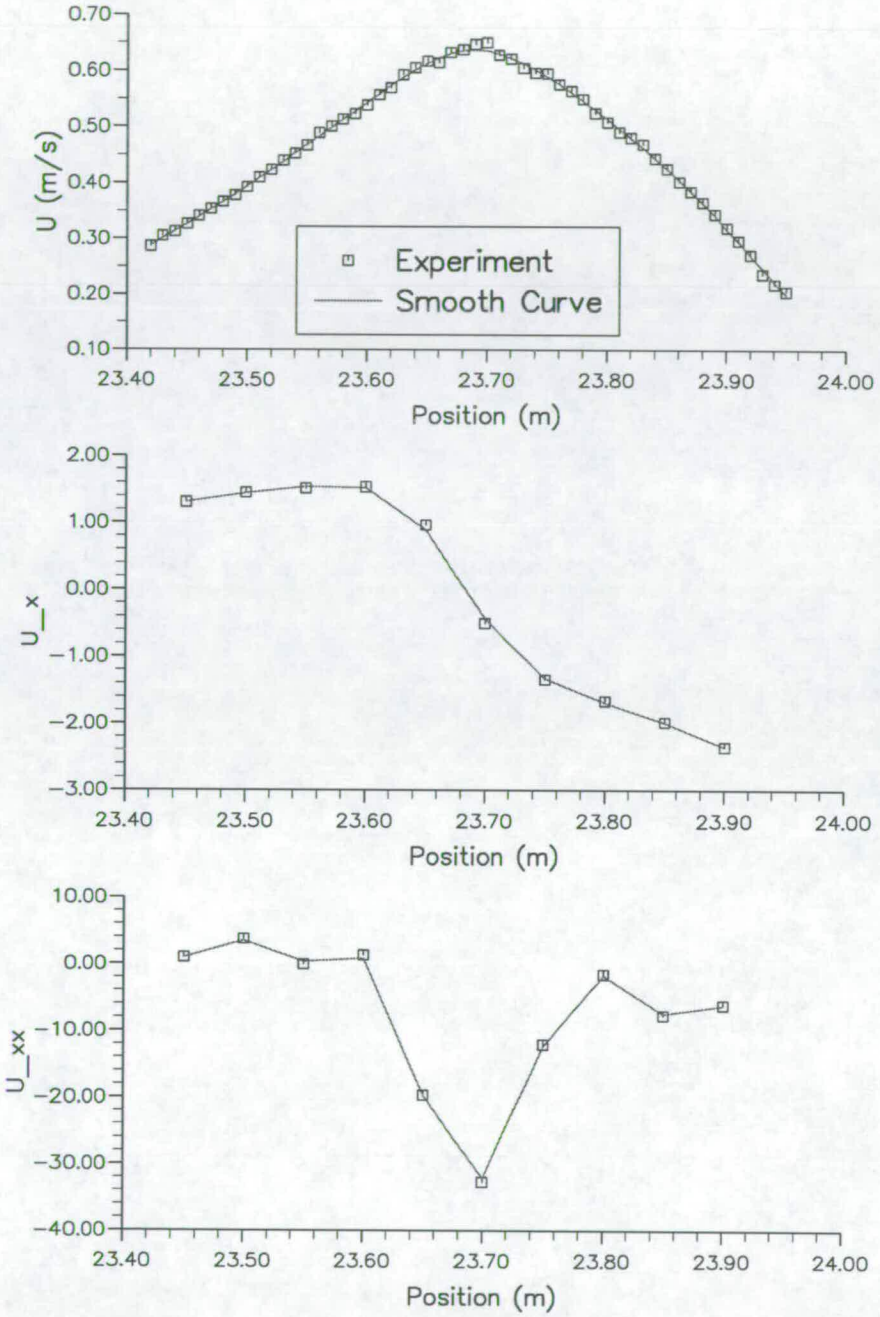

Figure 4.25: $\bar{u}$, $(\bar{u})_x$ & $(\bar{u})_{xx}$ Distributions: Position 1, Phase 1

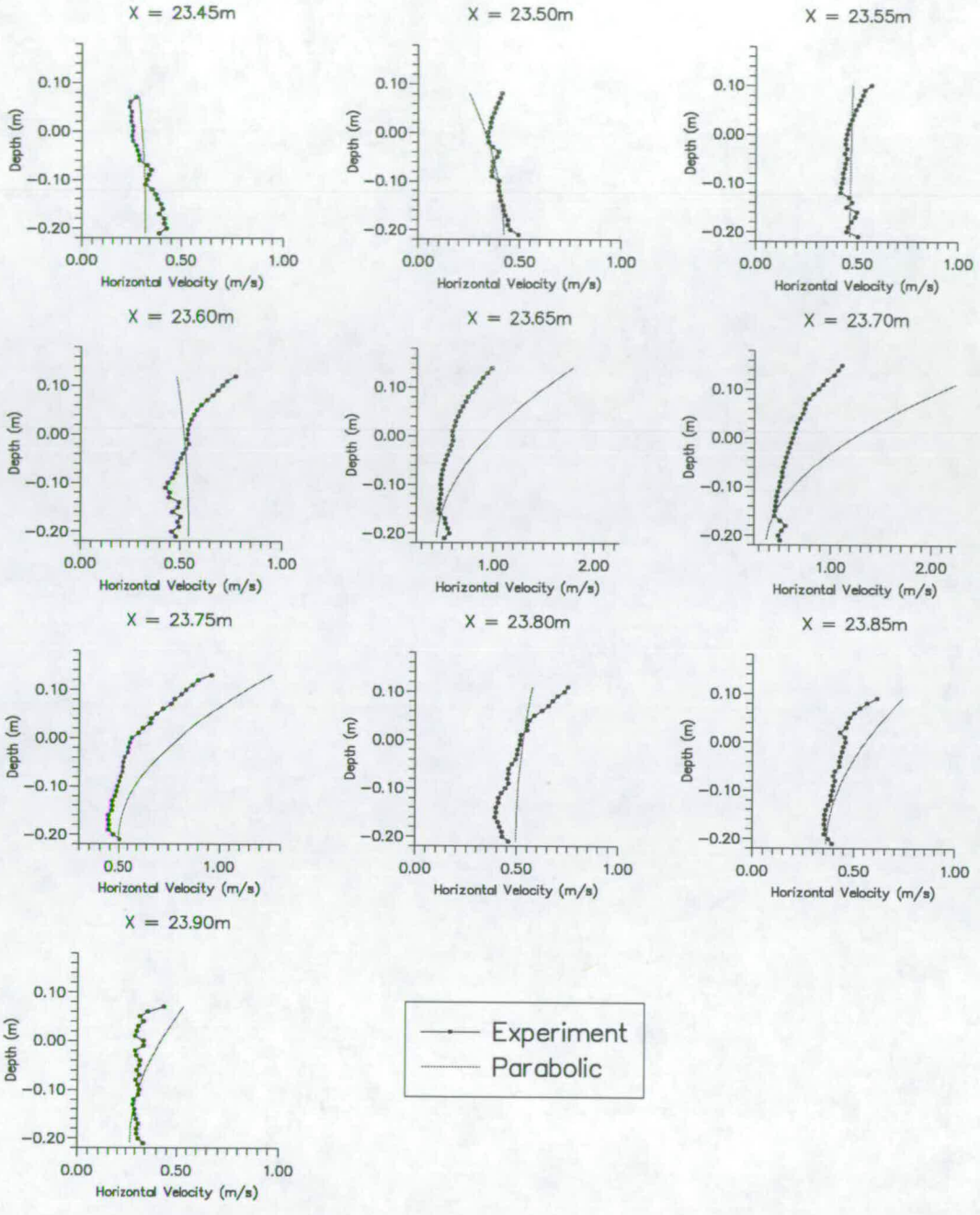

Figure 4.26: Comparison of parabolic profile with data: Position 1, Phase 1. ($h_{x=23.45} = 0.220$m; $h_{x=23.90} = 0.216$m; ($dx = 0.05$m, $dh = 5.00 \times 10^{-4}$m))

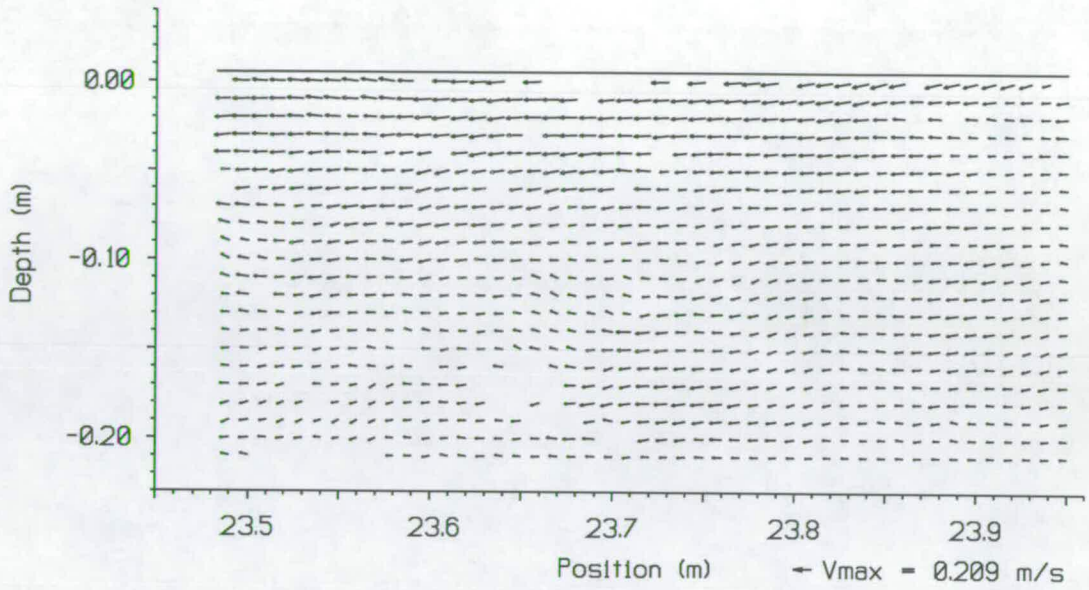

Figure 4.27: PIV vector map: Position 1, Phase 3

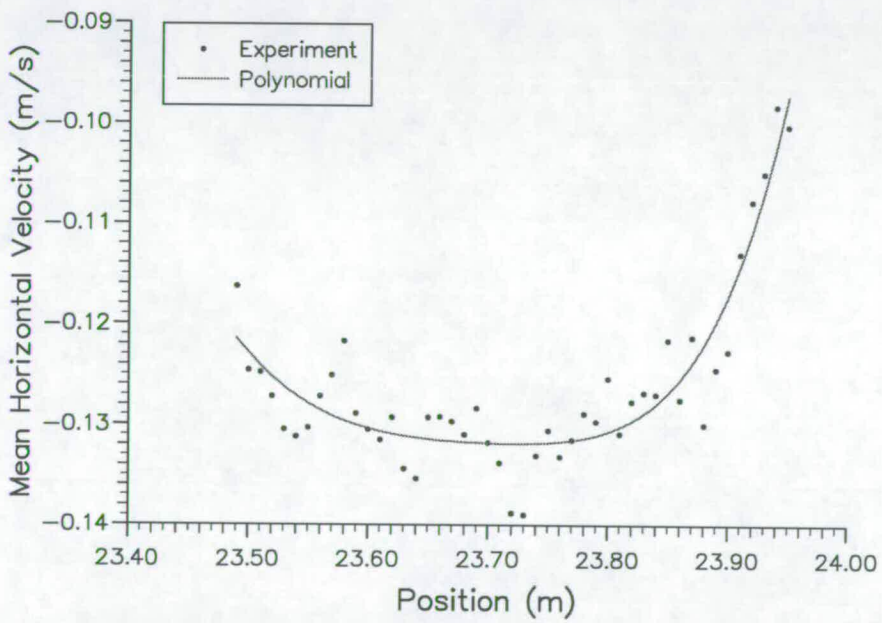

Figure 4.28: Mean horizontal velocities from vector map: Position 1, Phase 3

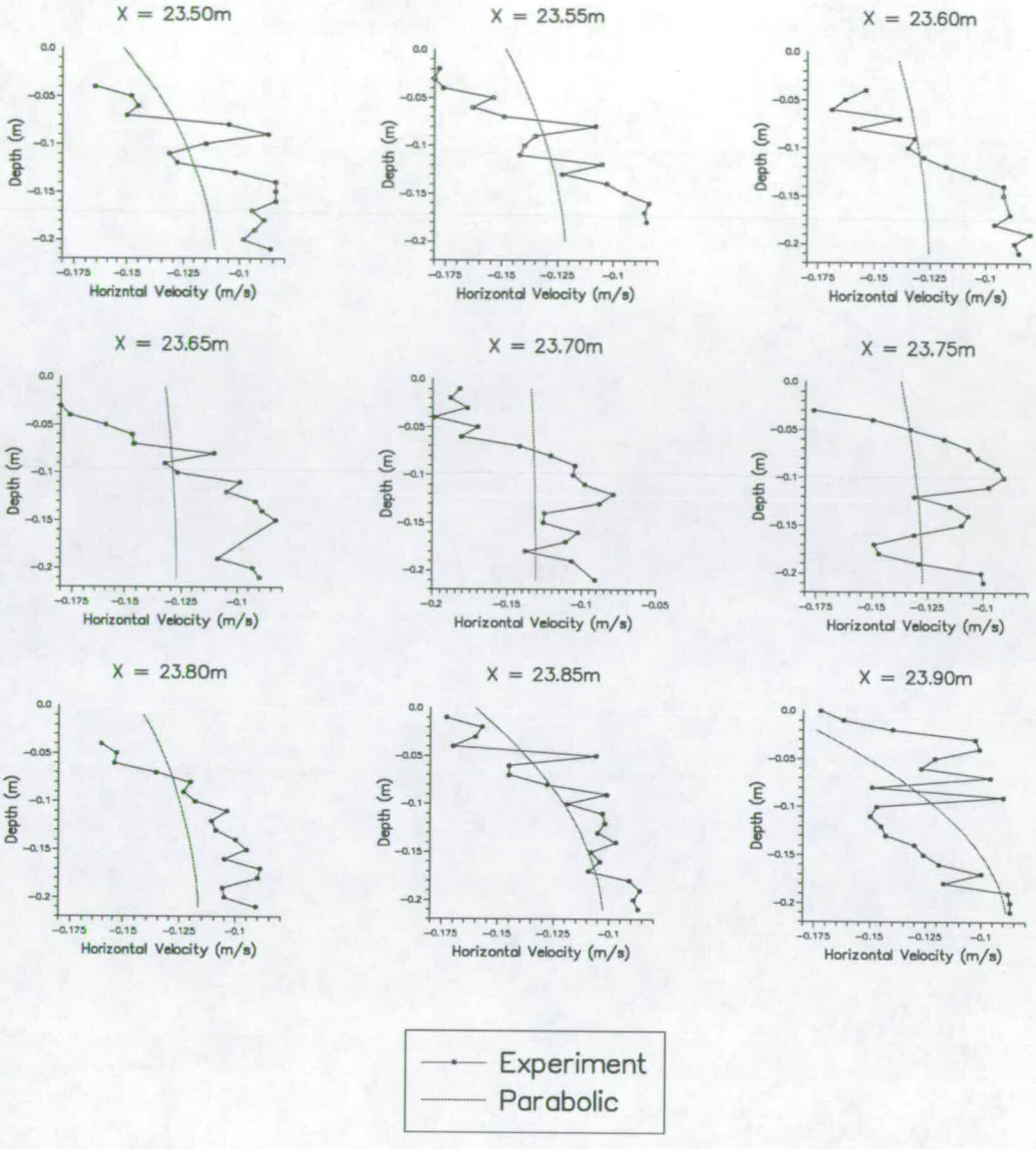

Figure 4.29: Comparison of parabolic profile with data: Position 1, Phase 3. ($h_{x=23.5} = 0.220$m; $h_{x=23.90} = 0.216$m; ($dx = 0.05$m, $dh = 5.00 \times 10^{-4}$m))

Results from Position 5, Phase 1

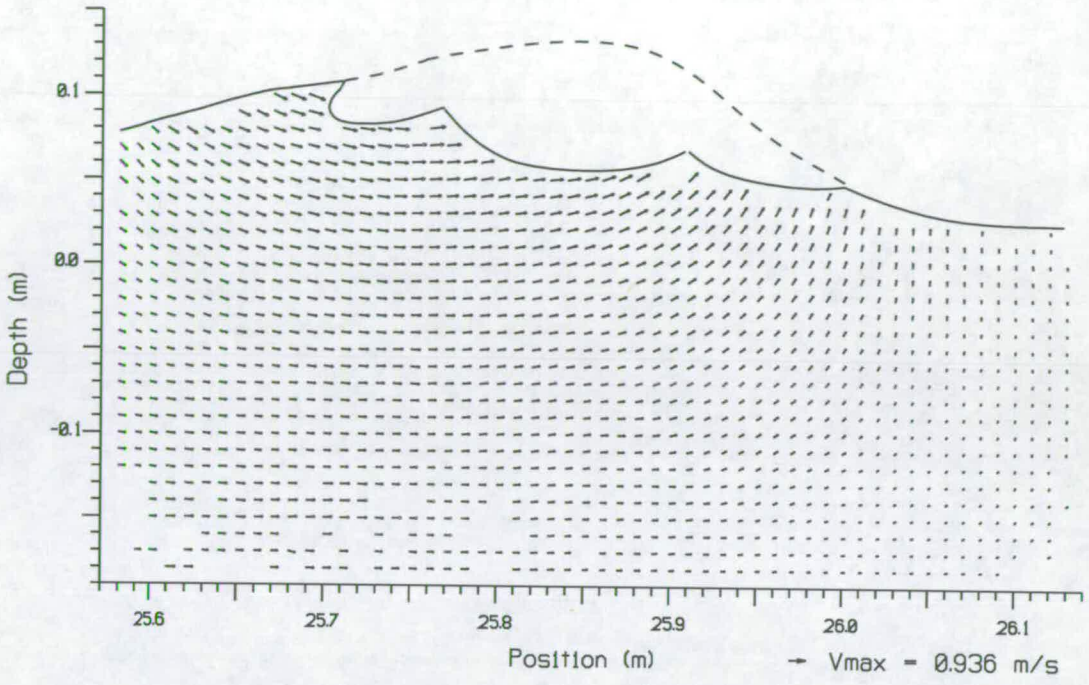

Figure 4.30: PIV vector map: Position 5, Phase 1

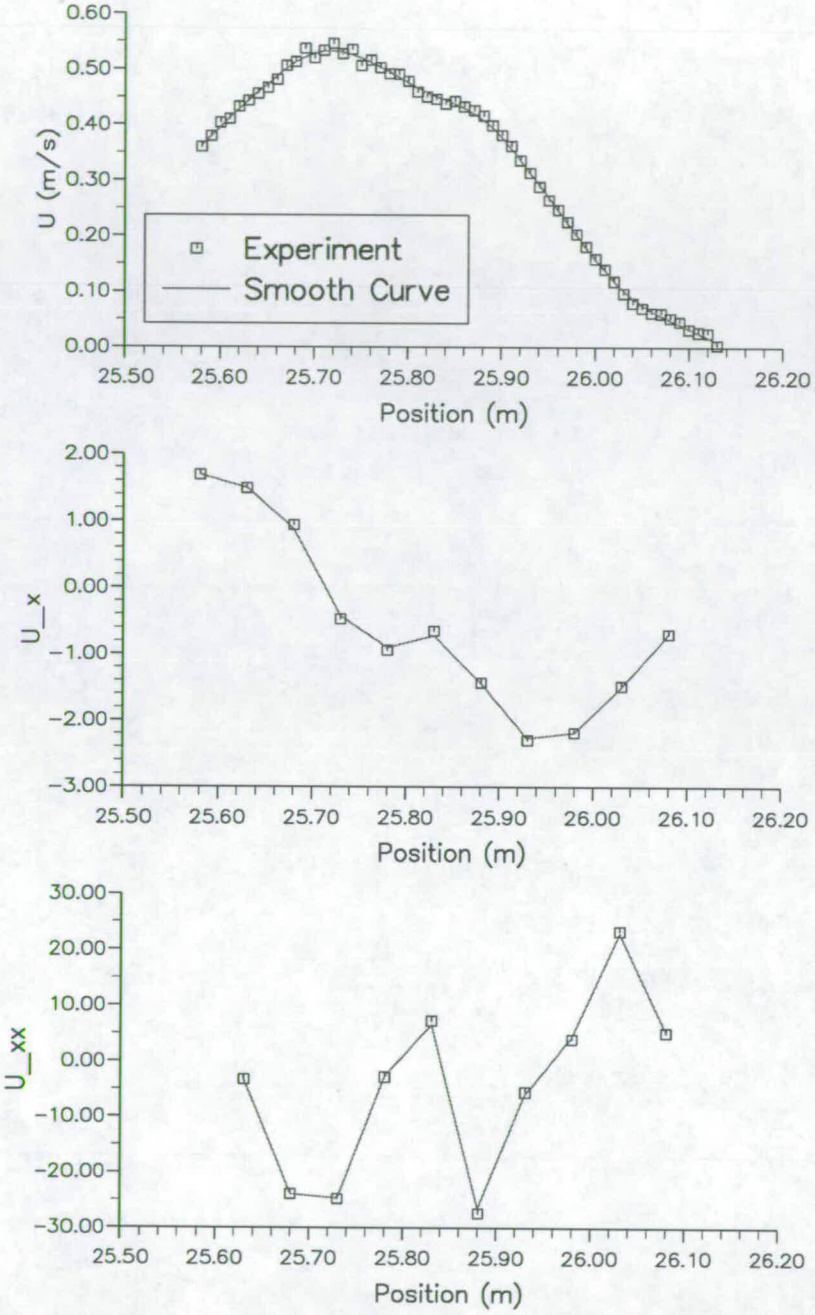

Figure 4.31: $\bar{u}$, $(\bar{u})_x$ & $(\bar{u})_{xx}$ Distributions: Position 5, Phase 1

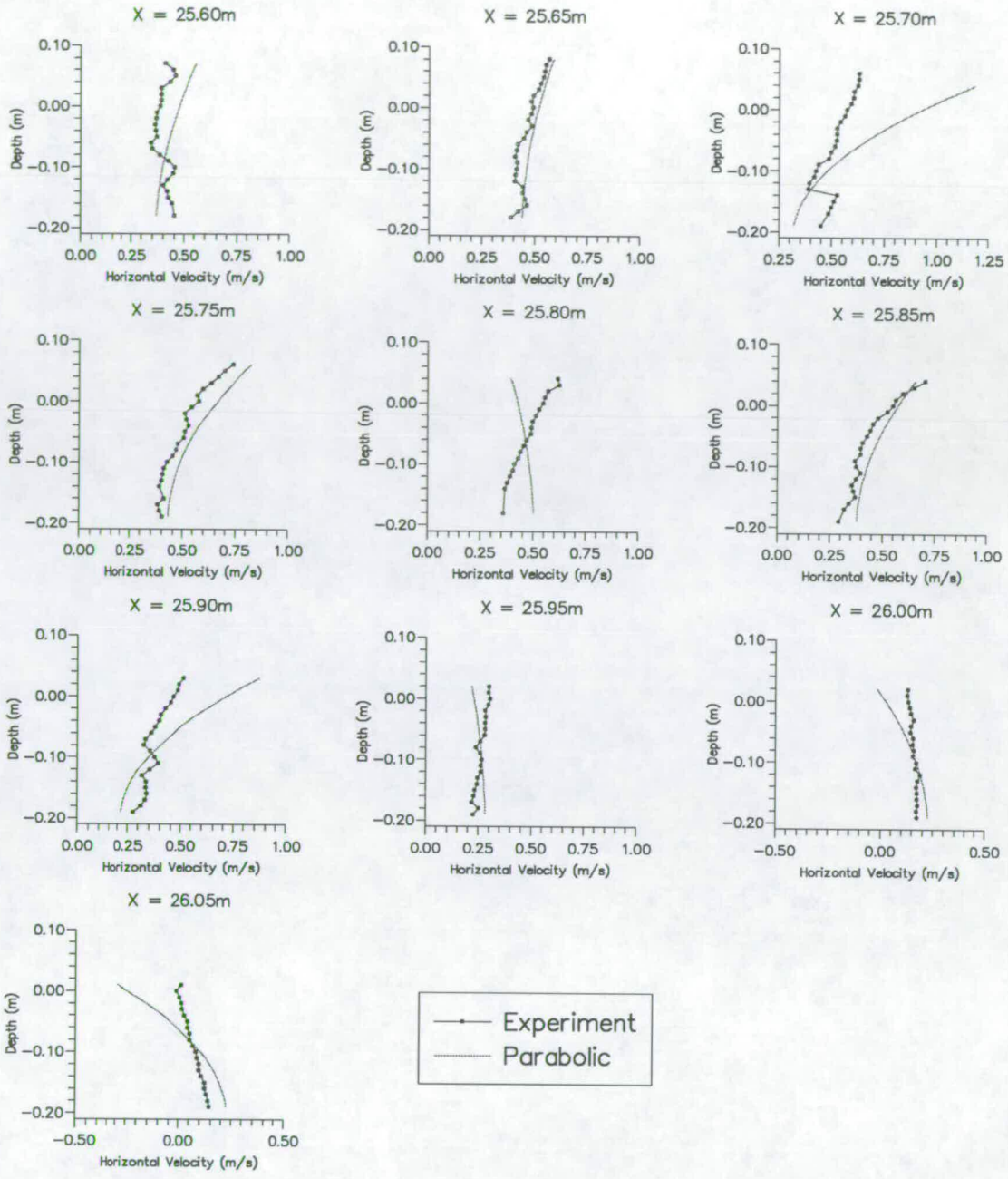

Figure 4.32: Comparison of parabolic profile with data: Position 5, Phase 1. ($h_{x=25.60} = 0.199$m; $h_{x=26.05} = 0.195$m; ($dx = 0.05$m, $dh = 5.00 \times 10^{-4}$m))

Results from Position 5, Phase 3

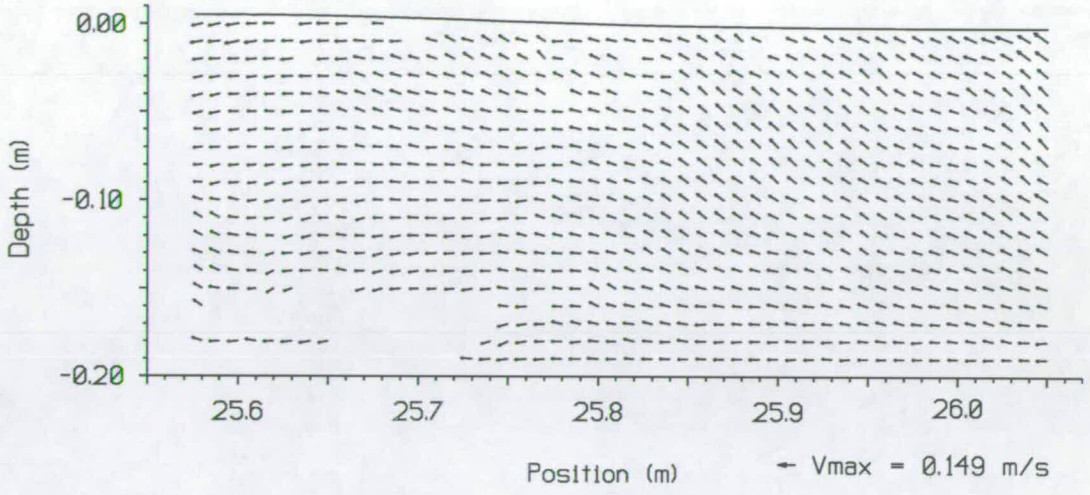

Figure 4.33: PIV vector map: Position 5, Phase 3

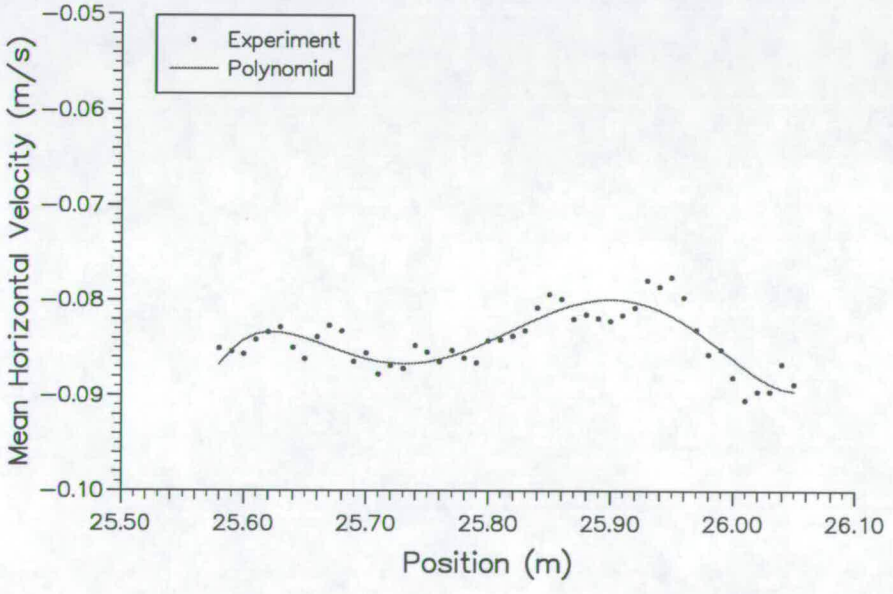

Figure 4.34: Mean horizontal velocities from vector map: Position 5, Phase 3

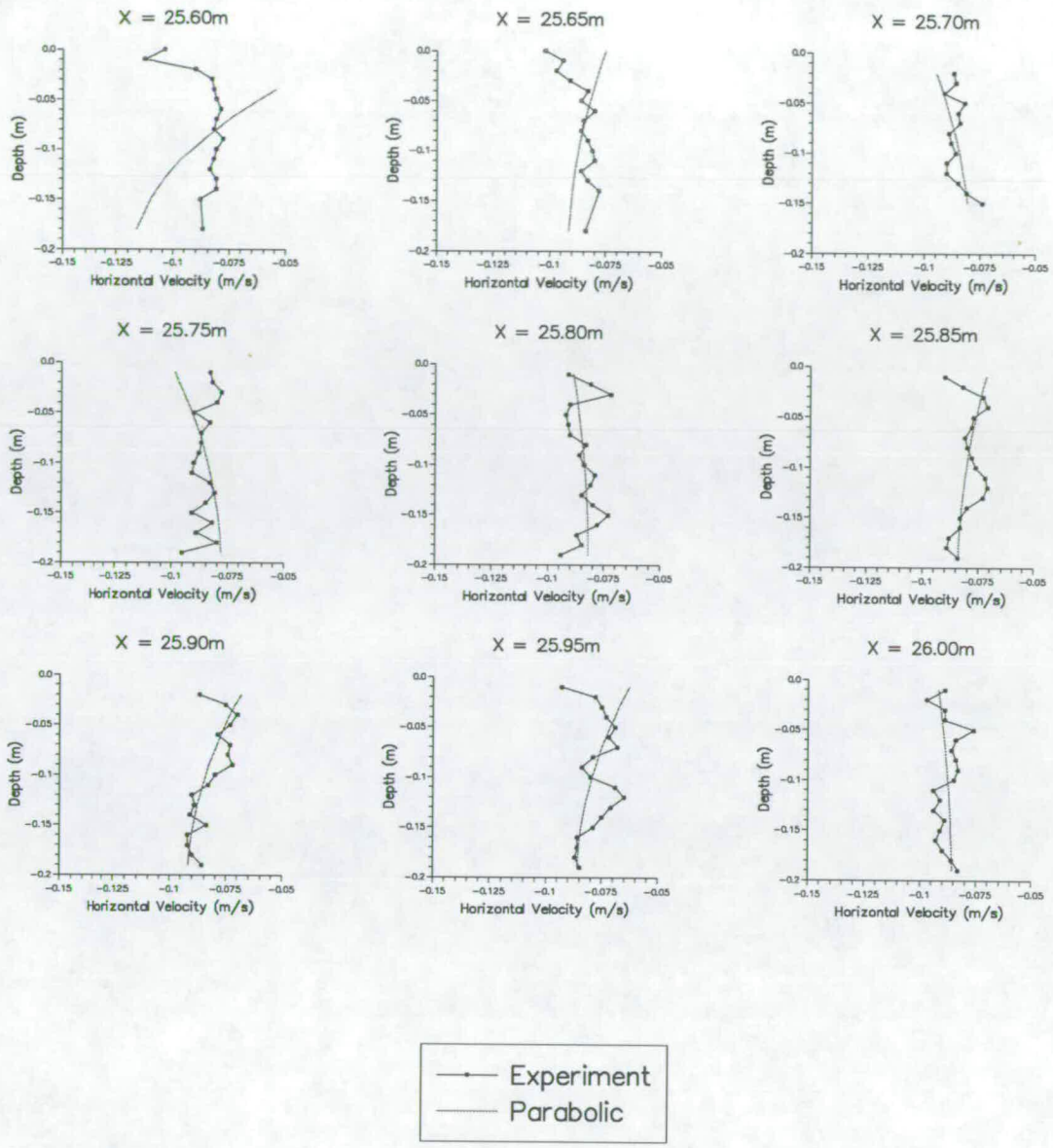

Figure 4.35: Comparison of parabolic profile with data: Position 5, Phase 3. ($h_{x=25.60} = 0.199$m; $h_{x=26.00} = 0.195$m; ($dx = 0.05$m, $dh = 5.00 \times 10^{-4}$m))

4.3.2 Comments

The benefit of the longer tank is particularly evident here because there is an adequate depth of water in the breaking zone to allow accurate measurements with PIV. Consequently, it is the breaking zone which is the focus of attention of this analysis. The main features of these graphs are summarised as follows:

1. There are larger discrepancies between the measured data and parabolic profiles than were evident on the 1:30 beach where a detailed analysis in the breaking zone was impossible due to the particularly shallow water depth in this region. This is most probably due to the higher degree of non-linearity in the waves in the breaking zone than farther down the beach and is shown in section 4.4.

2. Due to the aerated region in the breaker shown in figure 4.30 there will be an underestimate of the measured value of the depth-averaged velocity as PIV cannot measure in this area obscured by bubbles. This is evident from the peculiar shape of the mean velocity distribution shown in figure 4.31 and gives rise to the disagreement in the slope of the parabola at the $x = 25.8$m position in figure 4.32.

3. The mean horizontal velocities in the trough zones are much more scattered than in the 1:30 case due mainly to the increased turbulence in the breaking zone. This manifests itself not only in fitting the polynomial to the mean velocity data, but also in the comparison with the parabolic and actual velocity profiles.

4.4 Velocity Discrepancies under the Crest

There is a marked discrepancy between the calculated parabolic curve and the measured values of the horizontal velocity component in the near-surface region

under the crest; as has been noted in Sections 4.2.4 & 4.3.2. Since this discrepancy increased as the wave travelled up the beach it was decided to quantify the degree to which they differ with respect to the ratio a/h. Using this parameter one can use data from both beaches despite having different wave conditions on each.

The discrepancy or error, E, has been calculated using equation 4.25; where $Upara_i$ is the ith velocity component according to the parabolic profile and $Umeas_i$ is the corresponding measured component, with N being the number of measurements.

$$E = \frac{1}{N} \sum_{i=0}^{N} \frac{(Upara_i - Umeas_i)^2}{Umeas_i^2} \tag{4.25}$$

The error has been calculated in this way for crests recorded at all five measurement positions along the 1:30 beach and from the first measurement position on the 1:100 beach (see section 4.3.1). Figure 4.36 shows the average error E as a function of a/h on logarithmic axes with the straight line indicating a least squares best fit.

One can see from the "$\log_e - \log_e$" plot in figure 4.36, that the discrepancy between the parabolic and measured profiles appears to increase logarithmically up the beach for increasing non-linearity. Calculating the equation of the straight line from the graph, one obtains the relation shown in equation 4.26.

$$\log_e E = 3.11 \log_e(a/h) + 0.68 \tag{4.26}$$

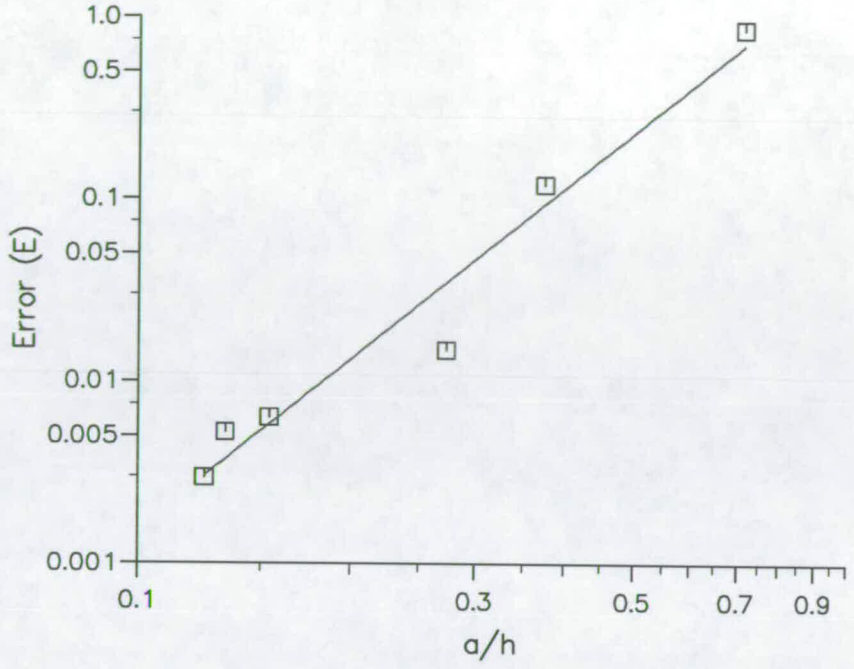

Figure 4.36: The variation of discrepancy E with a/h.

4.5 Integral Properties

4.5.1 Introduction

Further to the comparison of vertical velocity profiles from PIV data with wave model predictions is the calculation of the integral properties introduced in section 1.3. These wavelength-averaged functions, such as the radiation stress and mean energy flux have received much attention (Longuet-Higgins (1974), Longuet-Higgins & Fenton(1974), Longuet-Higgins (1975), Cokelet (1977), Stive & Wind (1982) and Klopman(1990)). As mentioned earlier, it is the derivatives of the radiation stress with respect to x and y which are among the most important factors in coastal engineering, driving the cross-shore and long-shore currents respectively (Dally & Dean, 1984); ie. $\vec{F} \equiv -\partial S_{ij}/\partial x_j$ is the driving force in the momentum equation.

It is the intention of this analysis to use the PIV data from the 1:30 beach to calculate the following integral properties: radiation stress S_{xx} (equation 4.27), mean energy flux F (equation 4.28) and mean momentum flux S (equation 4.29). The equations given below are based on those in Klopman (1990), following on from Longuet-Higgins (1975), for surface waves in the case of a non-zero Eulerian flow, ie. the horizontal velocity, at any level below that of the trough, averaged over one wavelength does *not* have to be zero; this is Stoke's second definition of phase velocity. They are derived exactly only for waves propagating in a constant depth of water, however, Copeland (1985) shows that these unaltered equations can provide accurate (within $\sim \pm 2\%$) solutions on slopes up to 1:3, at least as far as the spatial mean value of S_{xx} is concerned. For this reason their use to calculate values from the data measured on the 1:30 slope is thought to be valid.

$$S_{xx} = 4T - 3V + \bar{u_b^2} d' - 2\bar{u} I \tag{4.27}$$

$$F = C(3T - 2V) + \frac{1}{2}\bar{u_b^2}(I + \rho C d') - 2C\bar{u} I \tag{4.28}$$

$$S = S_{xx} - 2CI + \rho d'(C^2 + \frac{1}{2} g d') \tag{4.29}$$

In equations 4.27, 4.28 & 4.29 η is the surface elevation, C is the celerity or phase velocity of the wave, ρ is the water density, g is the acceleration due to gravity, h is the mean water level, $\bar{u_b^2}$ is the mean squared bed velocity, $\bar{u}$ is the mean horizontal velocity at any elevation below trough level and d' is the average water depth from the still water level, ie. the depth at $x + \frac{\lambda}{2}$. T is the mean kinetic energy, V is the mean potential energy and I is the mean wave momentum, defined as follows:

$$T = \overline{\int_{z_b}^{\eta} \frac{1}{2} \rho (u^2 + v^2) dz} \tag{4.30}$$

$$V = \overline{\int_{\bar{\eta}}^{\eta} \rho g z dz} \tag{4.31}$$

$$I = \overline{\int_{z_b}^{\eta} \rho u dz} \tag{4.32}$$

where z_b is the depth at the bed and $\bar{\eta}$ is the mean sea level; the overbar denotes averaging over one wavelength.

The data provided by PIV takes the form of a discrete grid of velocities so the integral signs in equations 4.30, 4.31 & 4.32 are replaced by summations, resulting in equations 4.33, 4.35 & 4.36,

$$T = \frac{1}{\lambda} \sum_{x}^{x+\lambda} \sum_{z=z_b}^{\eta} \frac{1}{2} \rho (u^2 + v^2) \delta a \tag{4.33}$$

$$V = \frac{1}{\lambda} \sum_{x}^{x+\lambda} \sum_{z=\bar{\eta}}^{\eta} \rho g z \delta a \tag{4.34}$$

$$= \frac{1}{\lambda} \sum_{x}^{x+\lambda} \sum_{z=\bar{\eta}}^{\eta} \frac{1}{2} \rho g z^2 \delta l \tag{4.35}$$

$$I = \frac{1}{\lambda} \sum_{x}^{x+\lambda} \sum_{z=z_b}^{\eta} \rho u \delta a \tag{4.36}$$

where δl is the length of one grid cell, and δa is its area.

It is the detailed velocity data provided by PIV which makes it desirable for calculating the integral properties; however, two problems have occurred with its implementation. The first of these drawbacks concerns the fact that, by definition, these properties are calculated by averaging over one wave period or wavelength. As PIV provides a spatial distribution of the velocity field, intuitively one would average over the wavelength rather than the period. This has one main drawback,

namely that it is the spatial derivative of the radiation stress which is desirable because it drives the cross-shore currents, so a detailed distribution of the radiation stress with respect to x is required, a factor not satisfied by averaging over a wavelength. Previous experiments to measure the radiation stress have relied on point-measurement techniques which, although suffering from low spatial resolution velocity data, have the benefit of being able to average over a wave period at a particular point (Stive & Wind, 1982, Rapp & Melville, 1990). In an attempt to minimise this problem a combined "space-phase" average has been carried out; as four phases of the wave were recorded at each measurement position the integral properties have been calculated from a quarter-wavelength contribution from each phase, thus reducing the extent over which the average is calculated by a factor of four. Obviously, if more phases had been recorded this space could be further reduced, and this is a recommendation for future PIV experiments aimed at calculating integral properties.

The second of the problems incurred was the step-like representation of the free surface caused by the fact that PIV data is produced in the form of a discrete grid of points. In order to improve this rather unrealistic representation of the free-surface, the corners of each "step" are joined, and velocities are extrapolated into the resulting triangle, as shown diagrammatically in figure 4.37.

4.5.2 Integral Properties Program and Test Case

A program to calculate the integral properties from PIV data has been written by the author, named INTPROP, based on the above equations. In order to test how well INTPROP performed it was tested with two numerical models before applying it to experimental data. The test involved using INTPROP to calculate the integral properties for the velocity field of an 11th order wave, generated by a program written by Chaplin (1980) . This program, based on stream function theory (Dean, 1965), has the same data format as PIV measurements, ie. a discrete grid of velocities. These values were then compared to those calculated by a program written by Klopman (1990) utilising the Fourier approximation

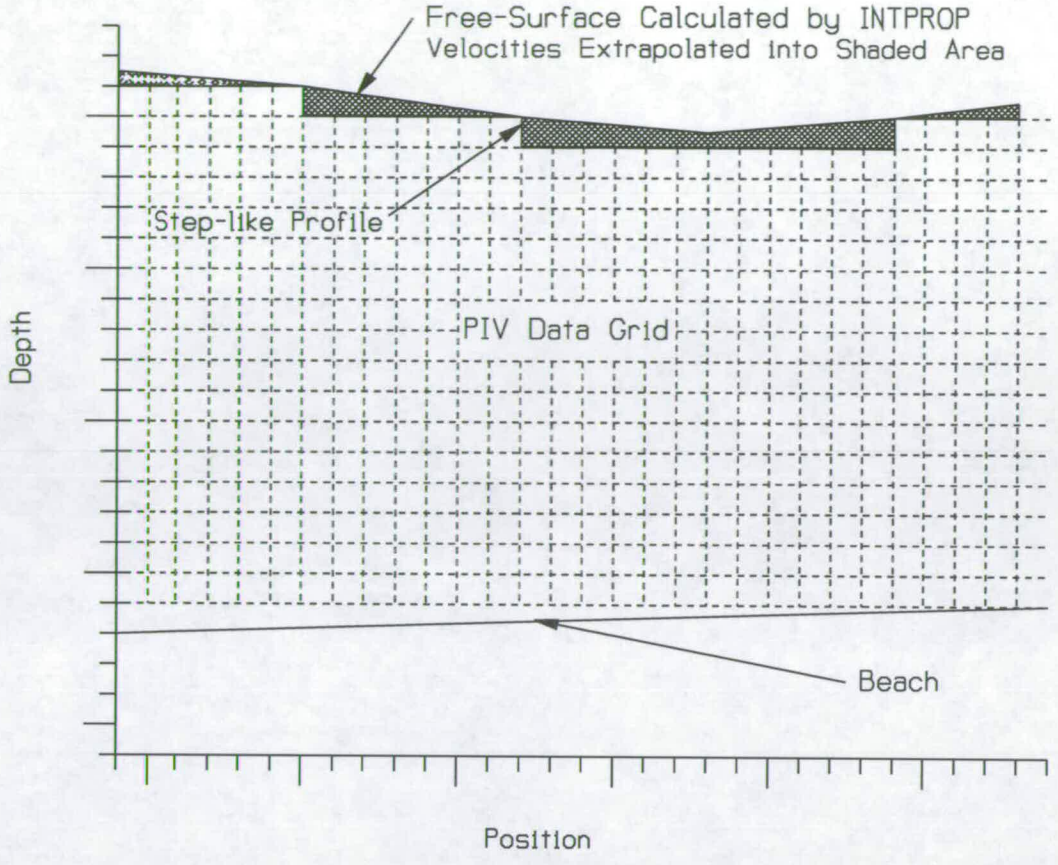

Figure 4.37: The "Step-like" free-surface generated by PIV Analysis.

method of Rienecker & Fenton (1981), with the same wave characteristics. The test case was a 0.8 s wave, with a wave height of 0.1m in a constant water depth of 0.75m. The results of the comparison are shown in table 4.1, with the percentage difference being calculated from equation 4.37.

$$difference = \frac{|intprop - klopman|}{intprop} \times 100 \tag{4.37}$$

At first glance some of these comparisons do not seem particularly good, and there are two possible reasons for these discrepancies; firstly the free-surface is not adequately represented, and secondly, the discrepancies may be due to the fact that the calculations are based on data from two different numerical models, with different inherent assumptions and properties. The main terms in the calculation of the radiation stress and mean energy flux, equations 4.27 & 4.28 respectively,

Property	*INTPROP + Chaplin*	*Klopman*	*Difference(%)*
Mean Sea Level	0.749	0.750	0.13
Potential Energy	5.019	5.771	14.98
Kinetic Energy	5.737	6.033	5.16
Wave Momentum	8.210	8.942	8.92
Radiation Stress	7.936	6.849	13.67
Wave Energy Flux	9.714	8.867	8.72
Momentum Flux	4106.40	4107.18	0.0002

Table 4.1: Integral Property Comparison

are the potential and kinetic energies. One can see from table 4.1 that the kinetic energies from both models show quite good agreement, but the potential energies exhibit larger differences. The main cause of the discrepancies between both the radiation stress and the mean energy flux are mainly due to this difference in potential energy. As the potential energy is a function of the free surface elevation it seems logical to check the two surface profiles first. Both programs yield the nearly identical values for the mean water level. The maximum and minimum elevations according to Klopman's program are 0.058m and -0.042m, respectively. The step-like data from Chaplin's program ranges from -0.05m to 0.05m, however, INTPROP makes the following assumption in creating the smoother free-surface: no velocity measurement will be obtained from a grid cell with less than half its height in the fluid. This corresponds to the situation, at the PIV negative analysis stage, where the interrogating laser beam falls on the free surface and only a small part of its area is in the flow, this normally causes signal drop-out. For this reason the maximum and minimum water surface elevations generated by the INTPROP program are 0.055m and -0.045m respectively, which is 0.003m lower than Klopman's values resulting in a 6% underestimate of the potential energy, reducing the discrepancy between them to about 6.3%, which is more acceptable.

As a large proportion of the differences between various properties shown in table 4.1 can be ascribed to the fact that two different wave models are being used, it was decided to proceed and use INTPROP to calculate integral properties from PIV data.

4.5.3 Integral Properties of waves on a 1:30 Beach

The integral properties were calculated for the 1.0s waves on the 1:30 plane sloping beach. The method of "space-phase" averaging, described in section 4.5.1, was used to limit the spatial extent over which the average was calculated, to 0.26m and 0.25m depending on the position on the beach. The wavelength was calculated at several different positions along the beach by looking at the zero-up-crossing points from the complete set of vector maps. It was found that the wavelength near the foot of the beach was $\sim$ 1.04m reducing to about 1m half way along the beach. This provided the two averaging ranges mentioned above. As the quarter-wavelengths of the waves on the 1:100 beach were greater than the length of the measurement region (ie. $\lambda/4 > 0.5$m) and "phase-matching" between adjacent measuring positions was not accomplished, the integral properties could not be calculated for this beach.

Figure 4.38 shows the variation of the mean water level in relation to the still water level; the characteristic set-down approaching the breaking point is evident.

The radiation stress, mean energy flux and momentum flux are shown in Figures 4.39, 4.40 & 4.41 respectively.

Although the distribution of the momentum flux is remarkably linear, there appears to be some considerable scatter on the graphs for the radiation stress and the mean energy flux. However, the scatter is mainly restricted to two regions, with the same set of five points having significantly lower values than the others in both graphs (these are marked as crosses on the figures.) One has to look, therefore, at the main factors from which the radiation stress and mean energy

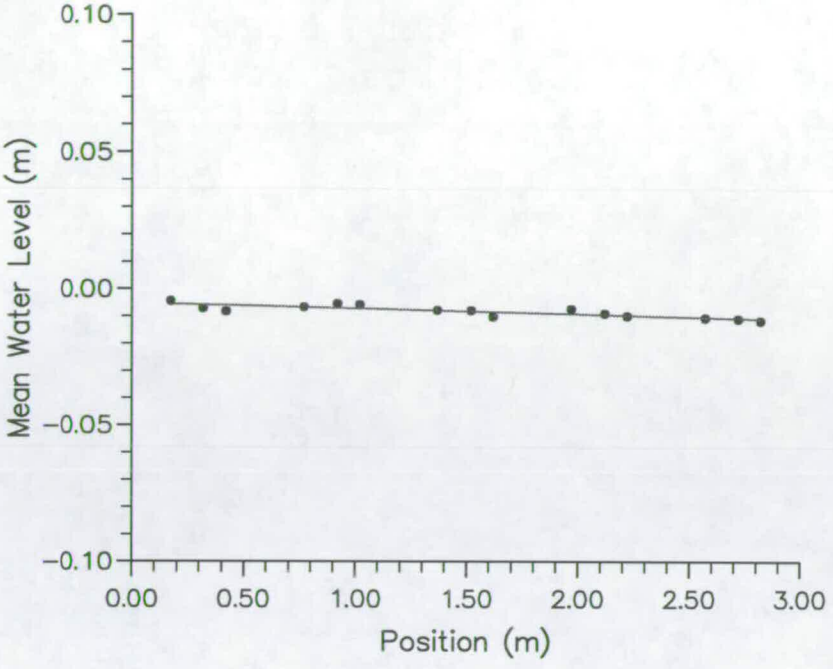

Figure 4.38: Variation of the mean water level calculated by INTPROP.

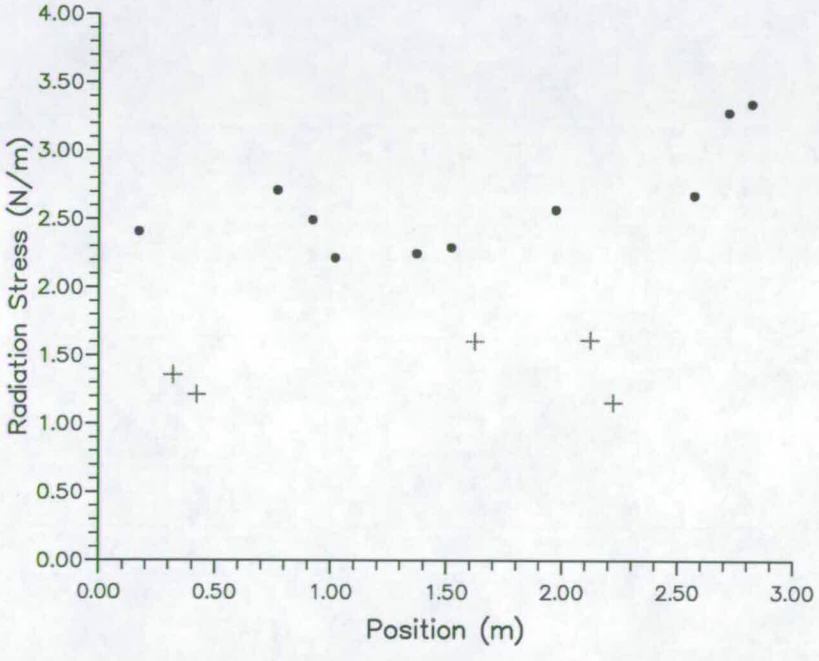

Figure 4.39: Radiation Stress Distribution (+ denotes a sub-set of values with significant differences. Refer to text for details.)

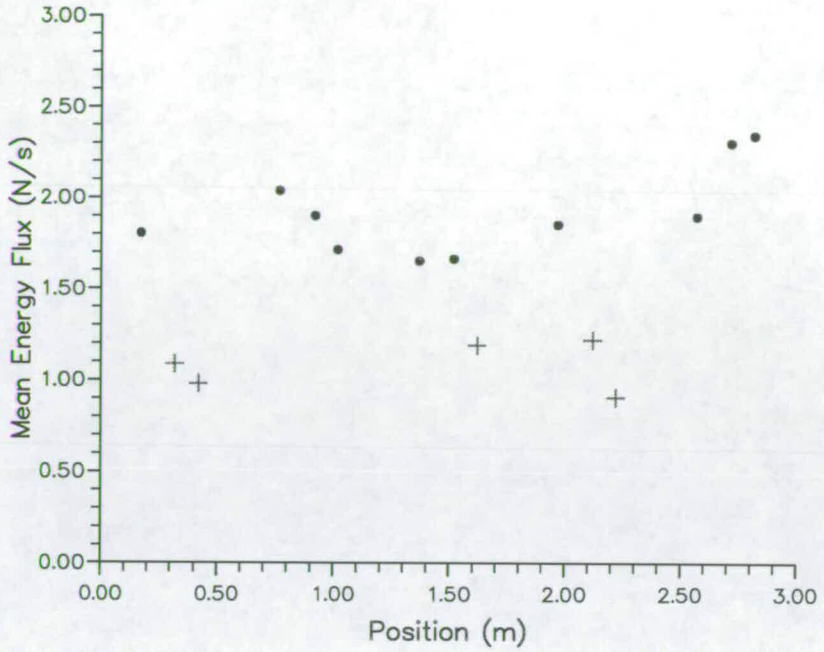

Figure 4.40: Mean Energy Flux Distribution (+ denotes a sub-set of values with significant differences. Refer to text for details.)

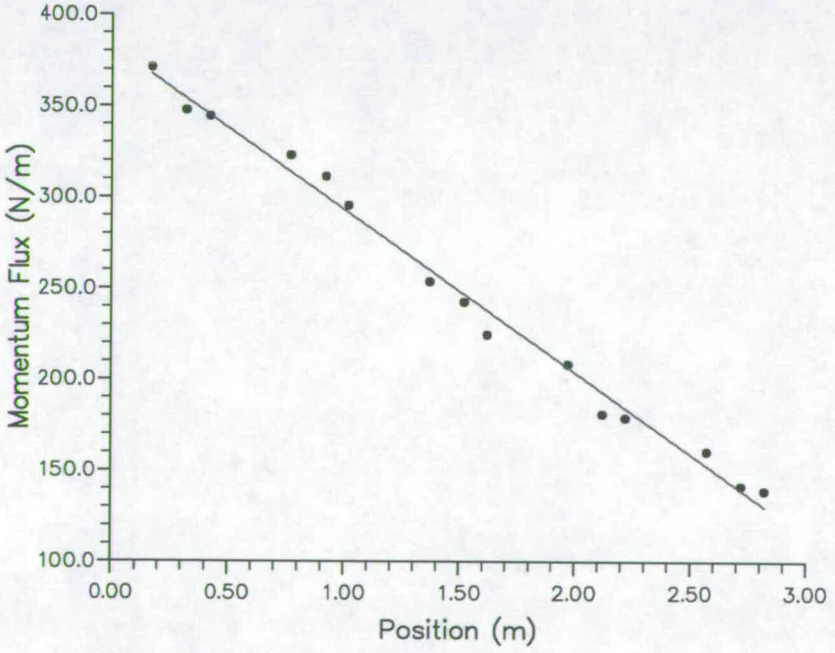

Figure 4.41: Momentum Flux Distribution

flux are calculated, namely the potential and kinetic energies; these are shown in Figures 4.42 & 4.43 respectively.

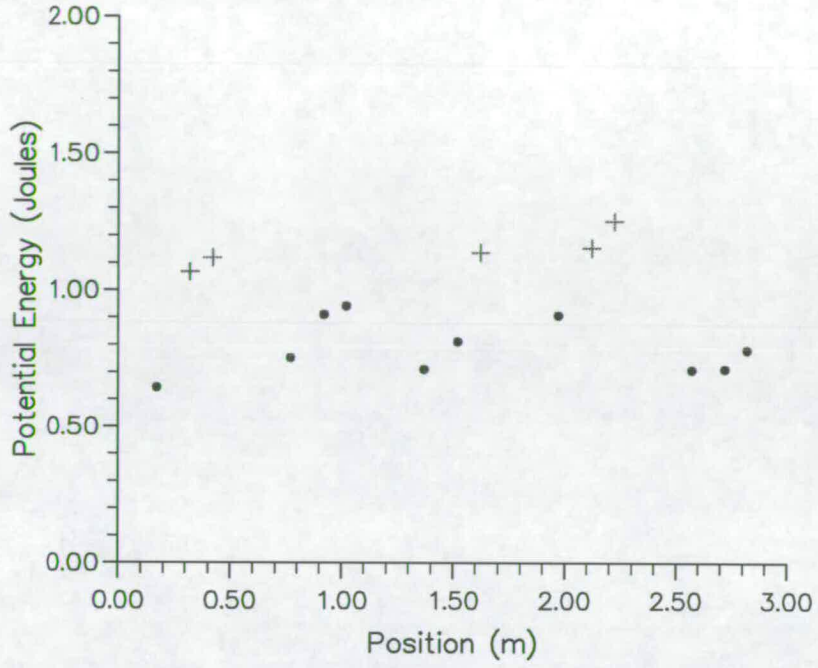

Figure 4.42: Potential Energy Distribution (+ denotes a sub-set of values with significant differences. Refer to text for details.)

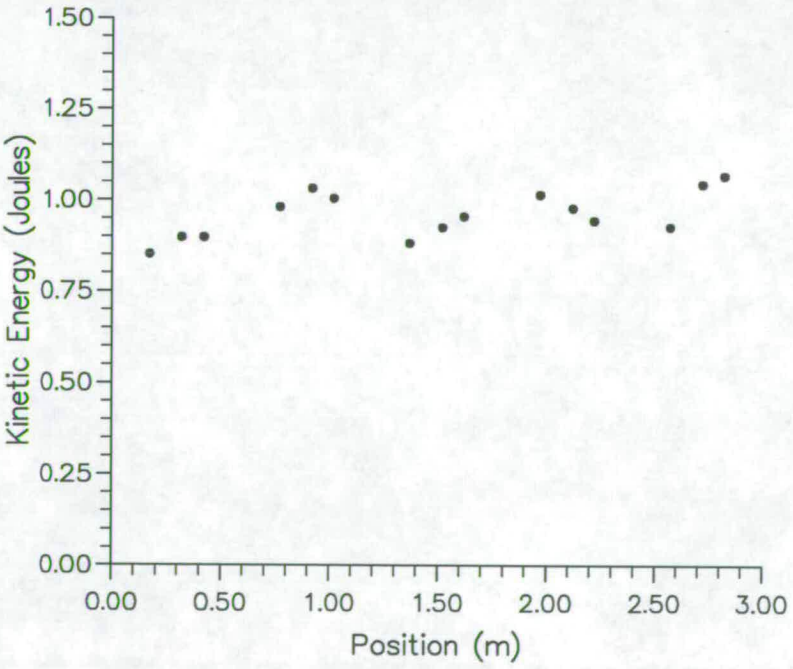

Figure 4.43: Kinetic Energy Distribution

One can see from figure 4.42 that the five points with significantly lower values of radiation stress and mean energy flux have substantially larger potential energies than the rest. This would indicate an inaccurate representation of the free surface, a factor which has already been acknowledged as a shortcoming in using data in the form of a discrete spatial grid. In fact, on closer inspection of the data it was found that for these cases the trough phase was represented by a straight line at the minimum elevation level; ie. it did not have a concave free-surface line which would reduce the difference from the mean sea level and consequently reduce the potential energy.

4.5.4 Comments on Integral Property Calculations

The use of PIV data to calculate the radiation stress, mean energy and momentum fluxes has been shown to be at least possible, and the distribution of the mean momentum flux shows good linearity with position along the beach. The scatter evident in the radiation stress and mean energy flux distributions has been mainly attributed to errors in the potential energy caused by problems associated with accurately specifying the free-surface from the "step-like" profile produced by PIV. If one was able to input the surface profile separately, from a wave gauge at each measurement position, the scatter would almost certainly be substantially reduced. The "space-phase" averaging technique appears to work and one can assume that any scatter due to this approach would be substantially reduced if more phases were recorded resulting in a smaller averaging domain. This would also enable the calculation of the derivative of the radiation stress with respect to x.

Chapter 5

Waves Breaking on Steep, Profiled Beaches

5.1 Introduction

The second type of beach examined in this study was that of steep, profiled beaches. This work was stimulated by experiments to measure shingle beach profile response to wave attack (Powell, 1988). Those experiments were carried out in the wave basin at HR Wallingford where various spectra of the JONSWAP type were allowed to impact normally on a shingle beach initially inclined at 1:7. The waves were created from three 5m absorbing wave boards and were chosen to represent different storm conditions. The beach profile was measured after every 500 waves using an automated tactile probe which was mounted on a rig above the beach. The rig was stepped in an offshore direction and at each step the probe was lowered until it touched the beach when the height was recorded. It was then retracted and stepped onto the next position. It was found that the beach had reached a state of dynamic equilibrium after about 3000 waves.

In general, storm conditions create a beach profile which has a bar near the wave breaking point, a relatively flat surf zone and a steep scarp just above the mean sea level formed by the run-up; this is shown in figure 5.1.

In these experiments great care was taken in choosing a suitable beach material,

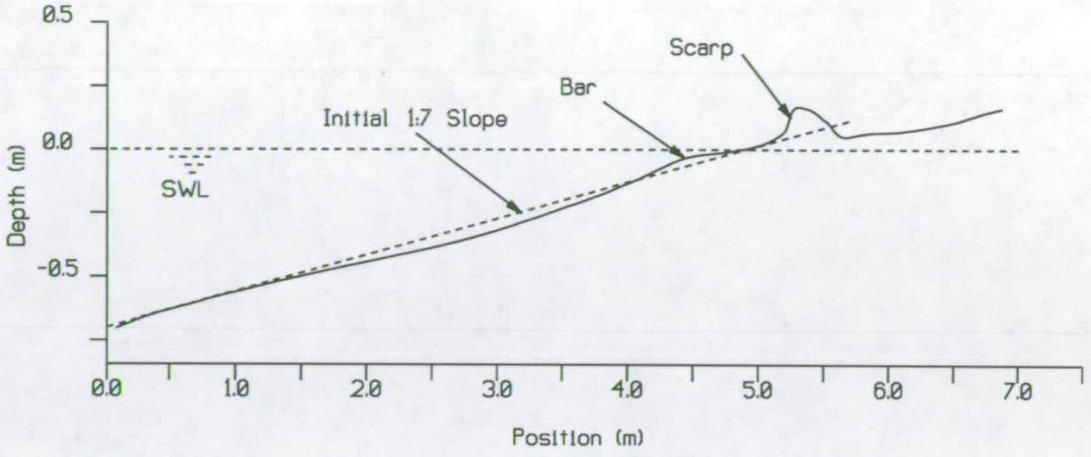

Figure 5.1: The general beach profile formed in storm conditions

to accurately represent the motion of the shingle beaches. There are three main features to consider in this selection, namely:

1. The permeability of the shingle beach.
2. The relative magnitudes of on-shore and off-shore motion; these should be constant.
3. The threshold of motion should be correctly scaled.

These criteria have been considered separately in Powell (1988) and coal particles were found to have the correct density and diameter for a model scale of 1:17. The coal particles chosen have a mean diameter (D_{50}) of 3.2mm and a specific gravity of 1:3.9.

From the numerous tests carried out at HR Wallingford, three profiles were selected for experiments at The University of Edinburgh for velocity field measurements; initially reported in Powell et al. (1992). Parameters from the wave spectra used to generate these three beach profiles are shown in table 5.1.

Profile	$T_{mean}(s)$	$T_{peak}(s)$	$H_{sig}(m)$	$Steepness(H_{sig}/\lambda_{mean})$
1	1.17	1.35	0.106	0.05
2	1.16	1.33	0.085	0.04
3	1.20	1.38	0.068	0.03

Table 5.1: HR Wallingford Wave Spectra Parameters

As the area of interest of the beach was seaward of the scarp, it was possible to work at a larger scale (1:10) than the experiments at HR Wallingford. The waves chosen for the present study were monochromatic waves whose frequency matched the mean frequency of the appropriate spectrum and whose height was derived from the significant wave height, shown in table 5.1, according to the relations given in equation 5.38 following on from equation 1.3.

$$H = \sqrt{2}H_r \qquad\qquad H_r = \frac{H_s}{4} \tag{5.38}$$

The use of monochromatic waves may seem a little unrealistic at first, however, this choice was made mainly due to the fact that PIV produces a spatial distribution of the velocity field at an instant, and so measuring a constantly varying wave field as in a JONSWAP spectrum, would provide results which would be difficult to interpret. One further consideration is that although the beach still reacts to individual waves, the average effect of the spectrum has resulted in a stable profile, hence our use of the mean wave frequency.

The measurement of bi-chromatic and tri-chromatic waves on beaches is currently under investigation in order to represent a more realistic wave field. This is an important next step because using monochromatic waves excludes the possibly significant effects of wave grouping and surf beat.

Due to time limitations only two beaches were modelled (Profiles 1 and 2 in table 5.1), however, the three different wave conditions were measured on each.

Profile	*Frequency*(Hz)	*Wave Height*(m)
1	0.655	0.063
2	0.660	0.050
3	0.640	0.040

Table 5.2: Wave Parameters used in the Edinburgh Experiments.

The wave parameters, now Froude scaled to a factor of 1:10, are shown in table 5.2.

The two profiles that were modelled and the one caused by wave number 3 are shown in figure 5.2 along with the initial 1:7 slope.

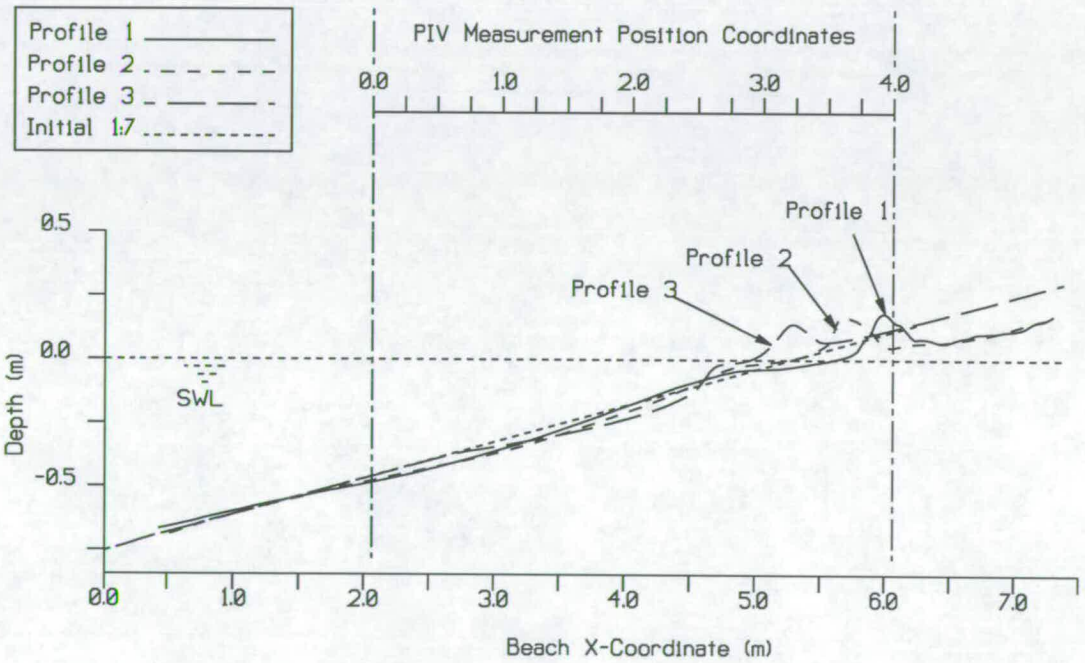

Figure 5.2: Three Beach Profiles & Initial 1:7 Slope

It is worth mentioning here the main characteristics of each of the beaches shown in figure 5.2. The first point to note is the horizontal position of the shoreline (intersection of the beach with the still water line (SWL)) with reference to the initial 1:7 slope. One can see that for Profile 1 it has advanced up the beach and for

Profile 3 it has moved offshore, while, for Profile 2, the position of the shoreline has remained essentially unchanged. Dealing first with Profile 1: this erosion of the shoreline is characteristic of the steep, energetic waves. The wave momentum after breaking is considerably greater than the other two waves and has resulted in the relatively long surf zone from the break-point at the offshore bar to the scarp face. This means that in the up-rush material will be pushed towards the scarp tending to build it up and move it further shorewards, and in the backwash material will be dragged back towards, and eventually beyond the bar. Both these processes tend to move the shoreline backwards. Now considering Profile 3, we have a build-up of material at the shoreline resulting in an offshore movement of the shoreline. Whilst only really speculating what may be happening, because this profile was not modelled at Edinburgh, if one looks at the profile in relation to the initial 1:7 slope it seems that the formation of the bar and scarp has occurred from a relatively localised scouring of the area in front of the bar which has piled material up in the region of the shoreline. This has created a steep offshore face to the bar forcing the waves to break at this particular point, and as the waves are smaller and they have a steeper slope to climb, the distance between the top of the bar and the face of the scarp is relatively small, allowing only a small run for the backwash to return material in an offshore direction. Profile 2 therefore, seems to be a balance between these two erosive and accretive processes. As the period of each of the waves is approximately the same (the maximum difference is 3%) it is the wave height variation causing either erosion, stability or accretion of the shoreline. One should remember here that this description assumes only monochromatic wave impact. (The detailed characteristics of the different JONSWAP spectra used to generate these three profiles are unknown to the author.)

Shingle beaches differ greatly from sandy beaches due to the different size of the material they consist of. As shingle is larger and heavier than sand a much steeper slope (1:7) can exist when compared to that of sandy beaches (1:100-1:30). This means that waves break much more abruptly on shingle beaches and one does not get the kind of travelling breaking waves favoured by surfers, typical of very shallow sandy beaches exposed to large wave attack; generally formed from the

long fetch associated with oceans rather than seas. A further consideration of a larger beach material is how it packs together. Not only does the larger material increase the friction of a beach but it also creates relatively large gaps between the individual elements. Dally et al., (1985) conclude that bottom friction plays a negligible role in wave decay when compared to shoaling and breaking, although this was for a sandy beach.

Thornton & Guza, (1983) derive an equation for the energy decay due to bottom friction, expressed as a fraction of that due to wave breaking, in the inner surf zone, which is shown in equation 5.39.

$$\frac{\epsilon_f}{\epsilon_b} = \frac{c_f}{3}[\frac{g^{1/2}}{\pi \bar{f}}]^{1/5}[\frac{15}{23}\frac{B\gamma^3}{\tan\beta}]^{4/5}h^{-1/10} \tag{5.39}$$

Where ϵ_f & ϵ_b are the energy dissipation rates due to friction and breaking respectively. c_f is the friction coefficient, $\bar{f}$ is the average wave frequency (a narrow band spectrum is assumed), B is the fraction of foam on the face of a wave, γ is an adjustable parameter linking the maximum height of a periodic wave in a given depth of water (ie. $H_{max} = \gamma h$) and β is the angle of the beach. Using values typical of the Torrey Pines Beach Data Set $c_f = 0.01$, $\bar{f} = 0.07$Hz, $\beta = 0.02$, $\gamma = 0.42$ and $B = 1$ (fully developed bores) the fraction of energy dissipation due to bottom friction was found to be less than 3%. For the smooth beach models used in the tests at Edinburgh this fraction will be further reduced because of the steeper slope. However, on a real shingle beach where the material size ranges from about $10 - 60$mm D_{50} the proportion of energy disspated by bottom friction may increase dramatically, especially in the swash zone; despite the steeper slope decreasing the $B\gamma^3/\tan\beta$ term in equation 5.39 by approximately an order of magnitude.

Turning now to the increased permeability of shingle beaches when compared to sandy ones, we find two main phenomena. Firstly, the real-time draining of the run-up and backwash into the beach above the Mean Sea Level (MSL), this has the effect of reducing the extent of the run-up and the amount of water returning in

the backwash, with a corresponding reduction in associated sediment movement. The second phenomenon is the out-flow of water further down the beach, which may assist the movement of material, particularly in the offshore direction. Having started the project and encountered a number of practical difficulties in building beaches with optical access for the laser beam, it was decided that construction of a permeable beach was beyond the scope of this study and indeed time factors prohibited the intended examination of friction effects. Given that this type of measurement has never been applied to waves on beaches it seems reasonable to first examine the main effects of beach shape on the internal kinematics of monochromatic waves. Further study to include irregular waves, roughness and permeability effects are certainly to be recommended.

5.2 Experiments on Profiled Beach 1

On Beach 1 measurements were taken at six adjacent positions of each of the three waves. Four phases of each wave were recorded at each position. In this way a complete flow field all along the beach was obtained for four phases of the three waves.

5.2.1 Wave Breaking on Profile 1: A Description

Plunging breakers were formed for each of the waves measured on Profiled Beach 1, as is shown in the photographs in figures 5.3, 5.4 & 5.5.

These photographs, and the corresponding ones for Profiled Beach 2, are from PIV negatives and one can clearly see the multiple-images of the seeding particles, particularly in the backwash, spout and even the spray of the photograph in figure 5.3. This is one of the advantages of the PIV technique used: that the data recording medium can provide a photograph displaying the qualitative flow pattern; and the analysed negative provides a quantitative velocity map.

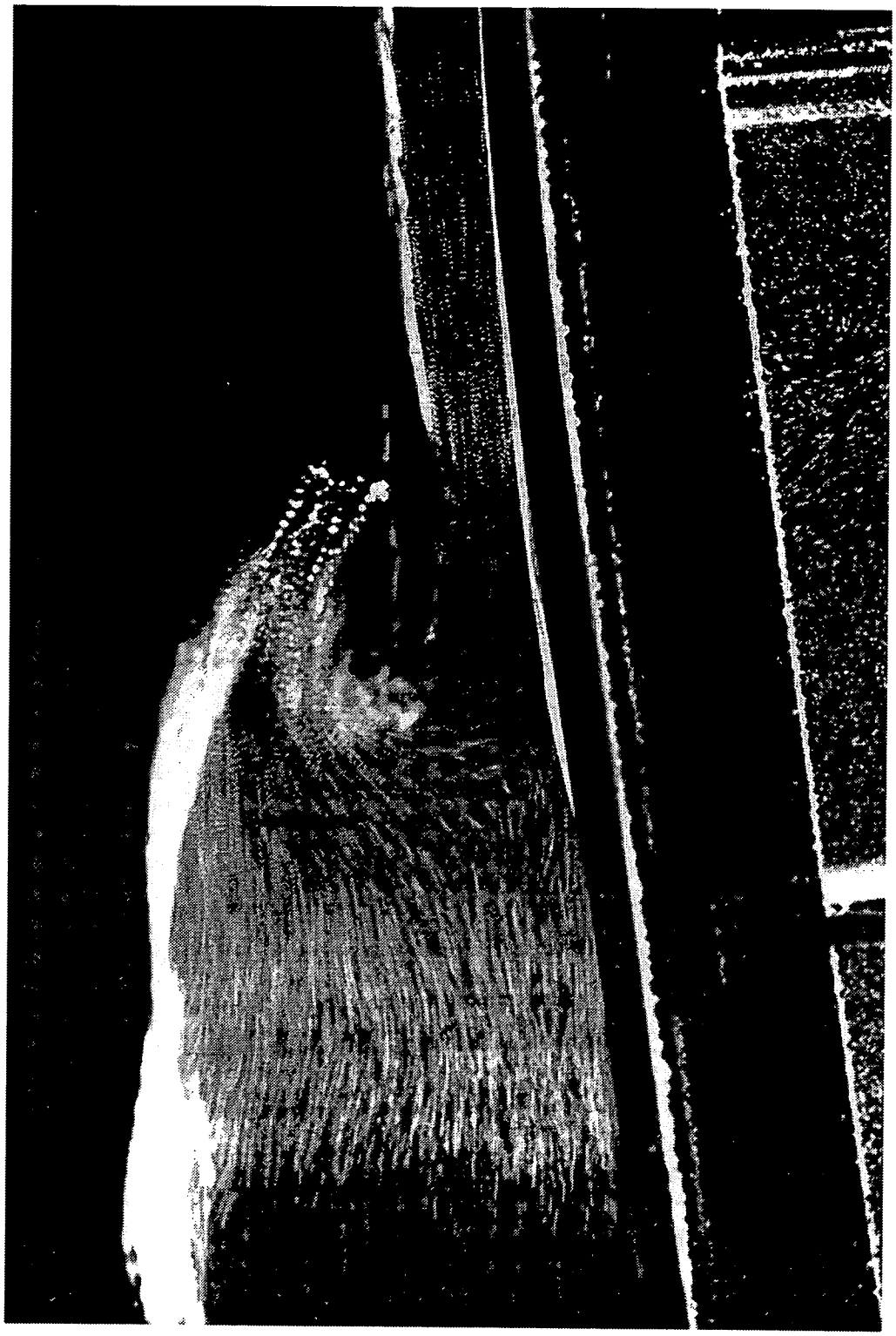

Figure 5.3: Wave 1 Breaking on Profile 1: f=0.655 Hz, H=0.063m

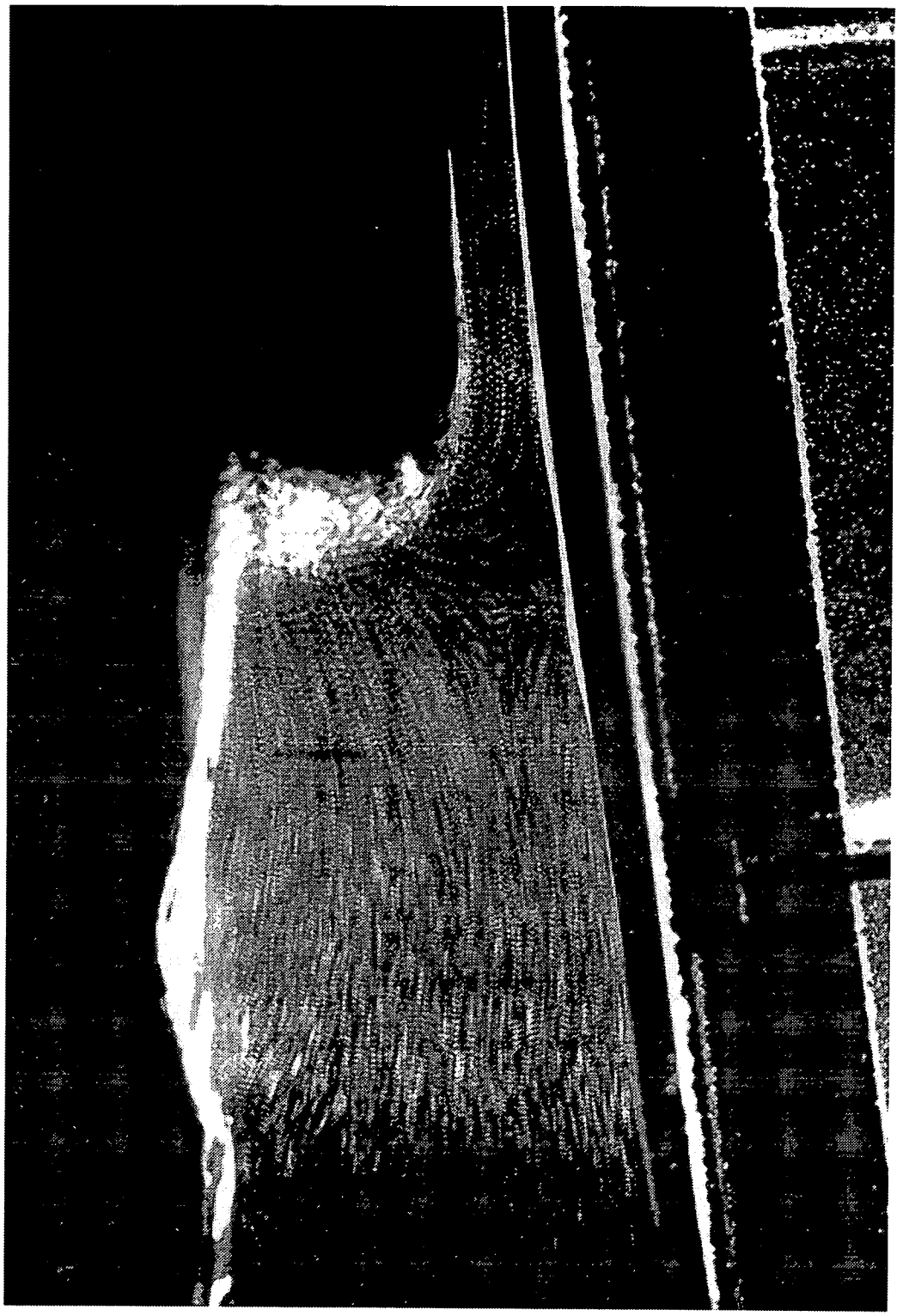

Figure 5.4: Wave 2 Breaking on Profile 1: f=0.66 Hz, H=0.050m

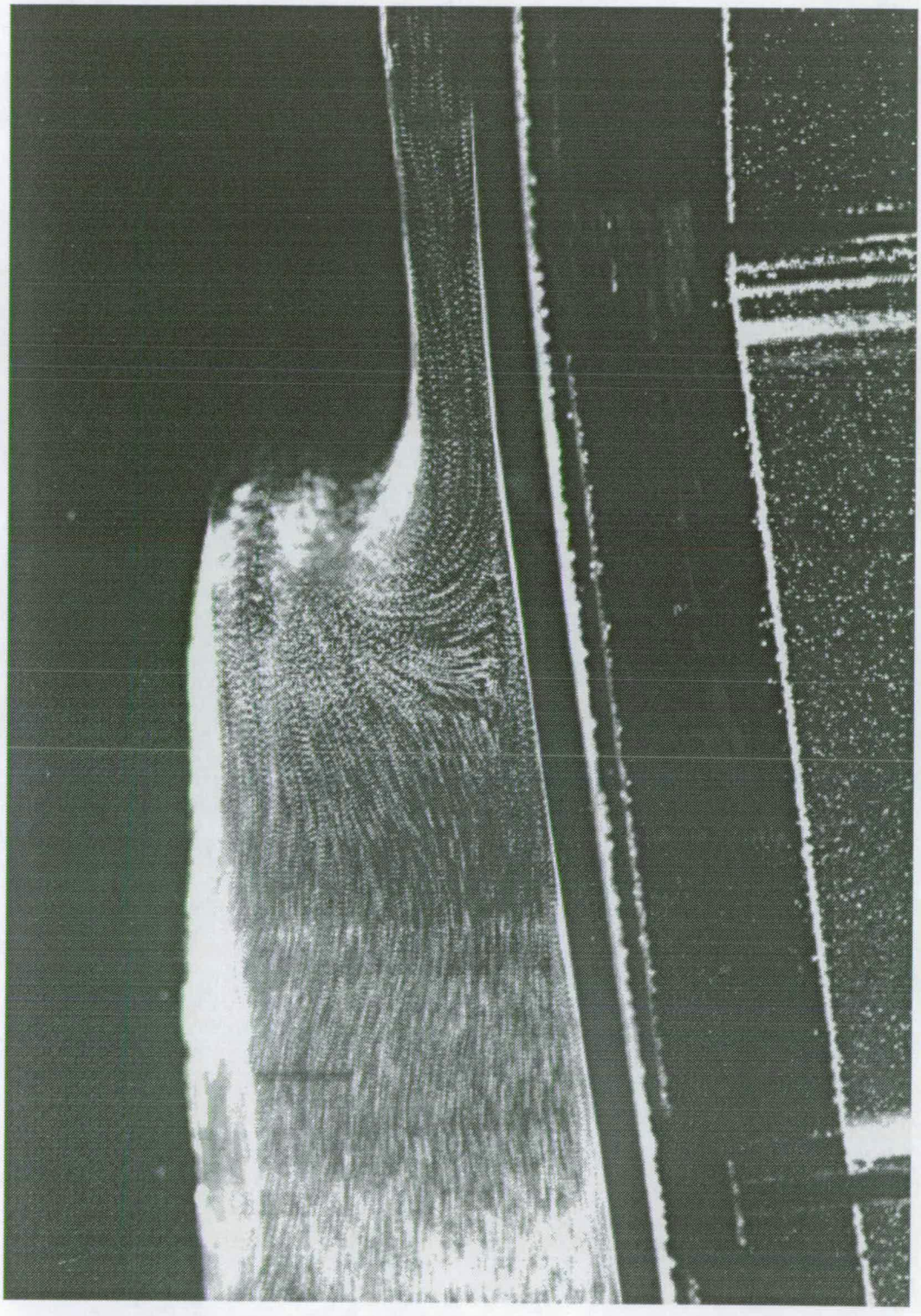

Figure 5.5: Wave 3 Breaking on Profile 1: f=0.64 Hz, H=0.040m

The fast flowing backwash can be seen clearly on all these photographs and this is an important characteristic of steep beaches and one which makes numerical modelling extremely difficult. The scarp provides a surface which abruptly stops the run-up and returns it offshore, this is emphasised in these experiments by the impermeability of the beach. On a real shingle beach there would be substantial in-flow into the beach above the MSL which would reduce the amount of water returning in the backwash. This high degree of beach reflectivity produces short-wavelength reflected waves which travel back offshore; this can be seen in some of the velocity vector maps in Sections 5.2.2 & 5.3.2.

5.2.2 Velocity maps for Profiled Beach 1

The three waves will be dealt with separately and four velocity vector maps are given as examples for each wave. The breaking crest and backwash phases are given for all the waves with the remaining vector maps representing different phases and positions along the beach. Starting with Wave 1 ($T = 0.655$s, $H = 0.063$m); figure 5.6 shows the trough phase at Position 3.

Figure 5.7 shows the crest at the next measurement position. There are quite a number of missing vectors in this figure, for two reasons. Firstly the exposure was slightly too low, as was the seeding density resulting in the patchy appearance of the central area and the space at the top right. The second reason, and this is evident on a number of vector maps from this beach and Beach 2, is due to a combination of near-zero velocity and high accelerations, the latter of which causes an unacceptably high displacement gradient across the small PIV interrogation area (see section 2.4.2). This is normally evident near the bed in front of the in-coming crest where the strongly negative horizontal velocity in the trough of the previous wave, reverses through a region of mainly vertical motion and then adopts a positive horizontal velocity under the crest; as can be seen near the beach on the right hand side of figure 5.7.

The plunging breaker formed at Position 6 is shown in figure 5.8 where the in-

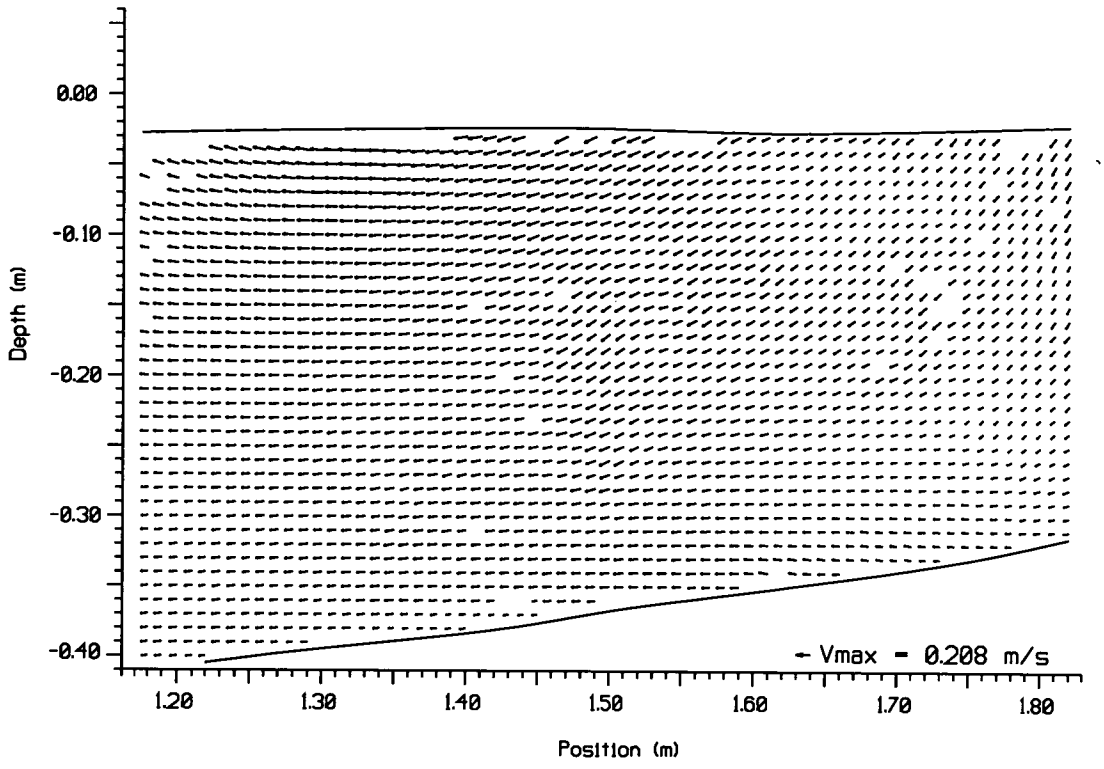

Figure 5.6: Wave 1: Position 3: Phase 2

teraction with the strong backwash component can also be seen. The preceding phase is shown in figure 5.9, showing the fully formed backwash.

Moving on to Wave 2 ($T = 0.66$s, $H = 0.050$m), figure 5.10 shows the trough phase at Position 3, where once again the detail of PIV velocity data is demonstrated. One can note the reduction in the maximum velocity (absolute value) at this position between Waves 1 & 2, figure 5.6 shows the corresponding phase at Position 3 for Wave 1 whose maximum velocity magnitude is 0.208 ms^{-1} compared to the 0.185 ms^{-1} of Wave 2.

The crest phase at Position 4 is shown in figure 5.11, which also shows the expected velocity differential between corresponding phases of different amplitude waves at the same position. The maximum velocity measured in Wave 1 (figure 5.7) is 0.243 ms^{-1} and for Wave 2 it is 0.227 ms^{-1}.

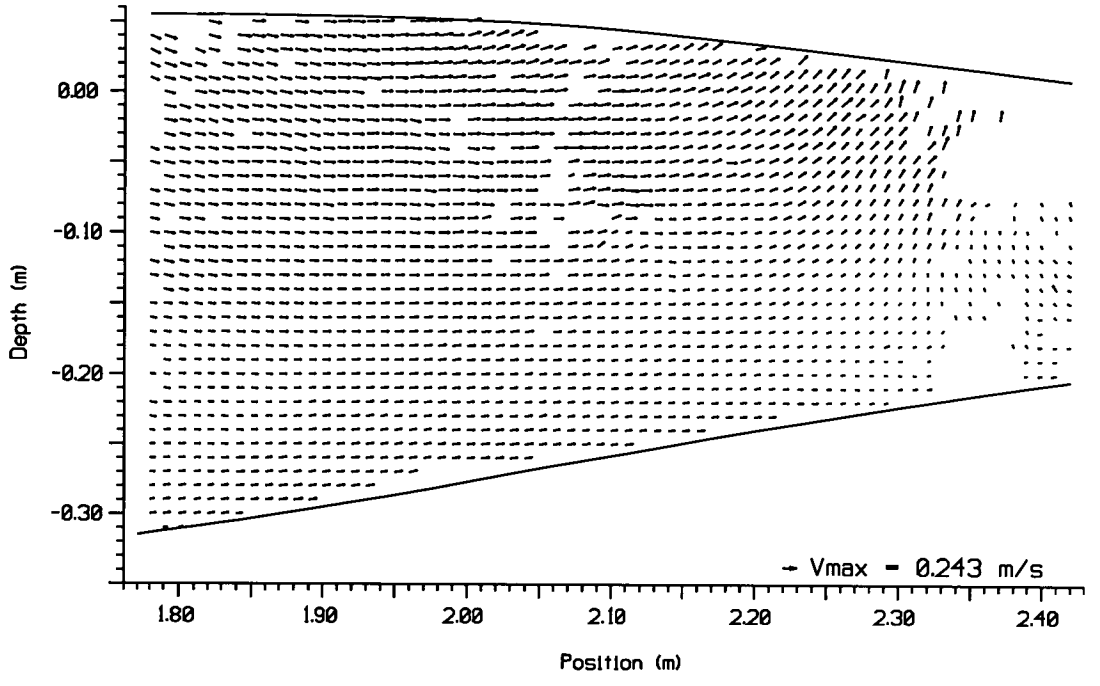

Figure 5.7: Wave 1: Position 4: Phase 1

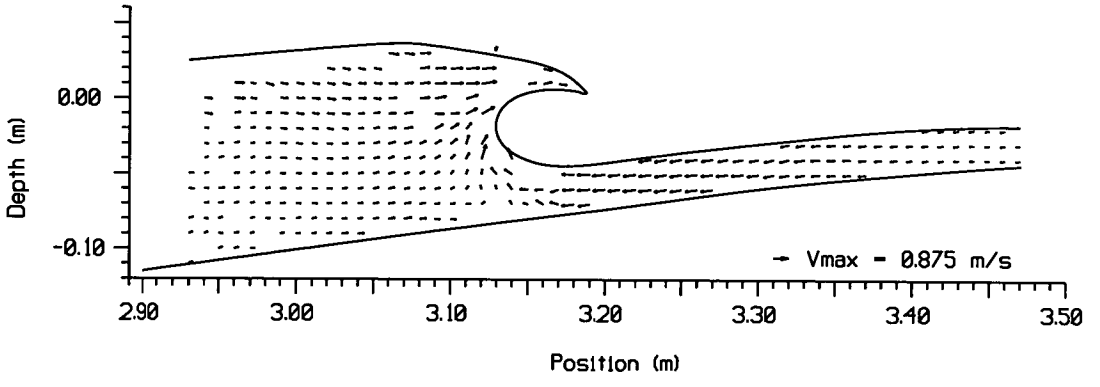

Figure 5.8: Wave 1: Position 6: Phase 3

Figure 5.12 shows Wave 2 breaking at Position 6; unfortunately there is more signal drop out due to a combination of PIV-related factors, such as photographic exposure, seeding density variations and the high dynamic range of this flow. However, the interaction of this wave with the backwash of the previous one and the magnitude of the velocities near the tip of the breaker are still shown. The fully formed backwash is shown in figure 5.13.

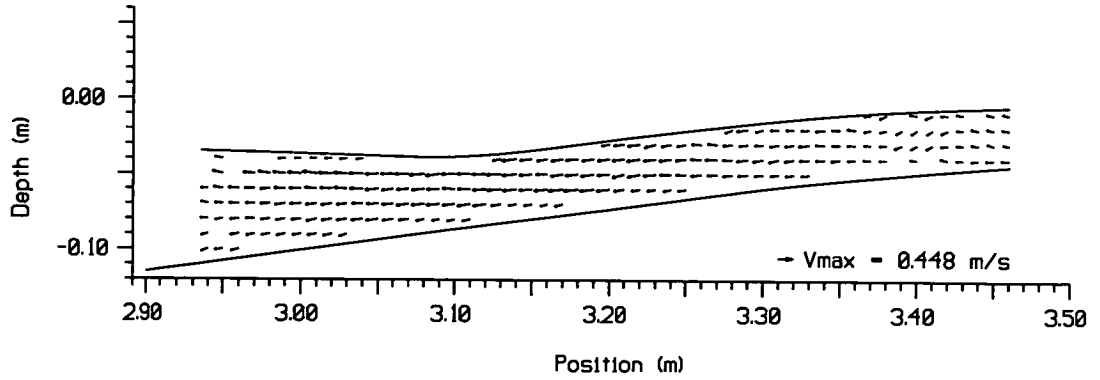

Figure 5.9: Wave 1: Position 6: Phase 2

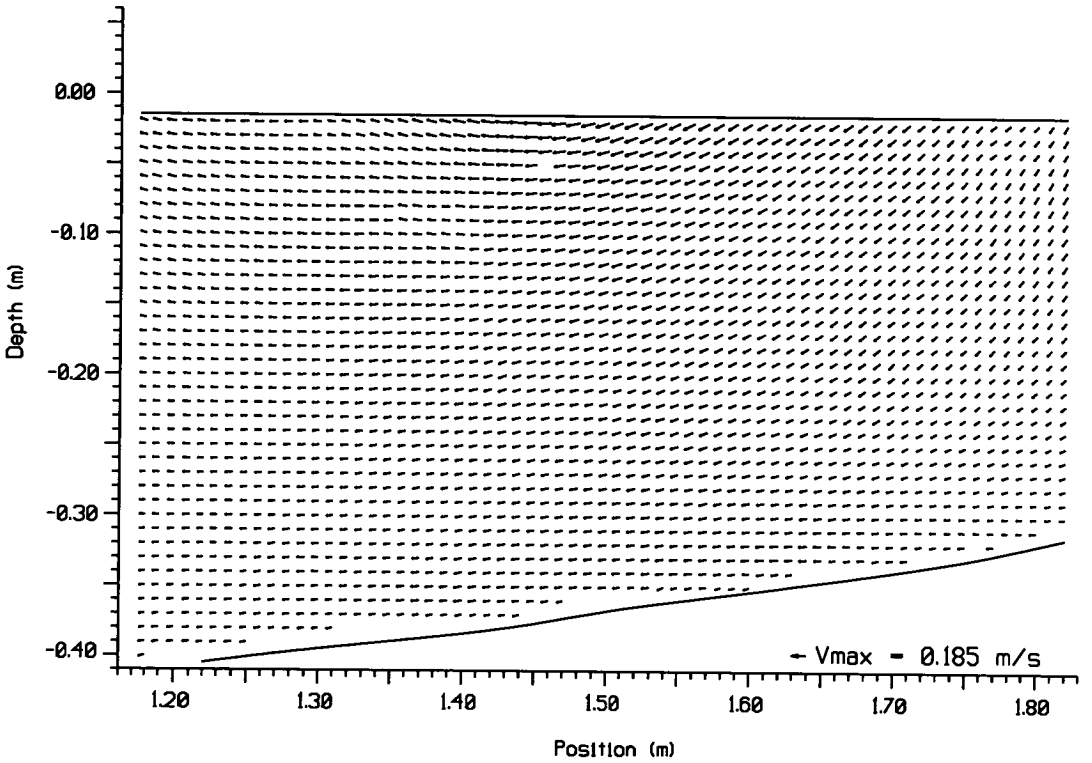

Figure 5.10: Wave 2: Position 3: Phase 2

The problem of resolving very low velocities is shown clearly in figure 5.14 for Wave 3 ($T = 0.64$s, $H = 0.040$m) at Position 2, which is otherwise a very detailed vector plot.

The crest phase at Position 4 is shown in figure 5.15; as with the the previous two

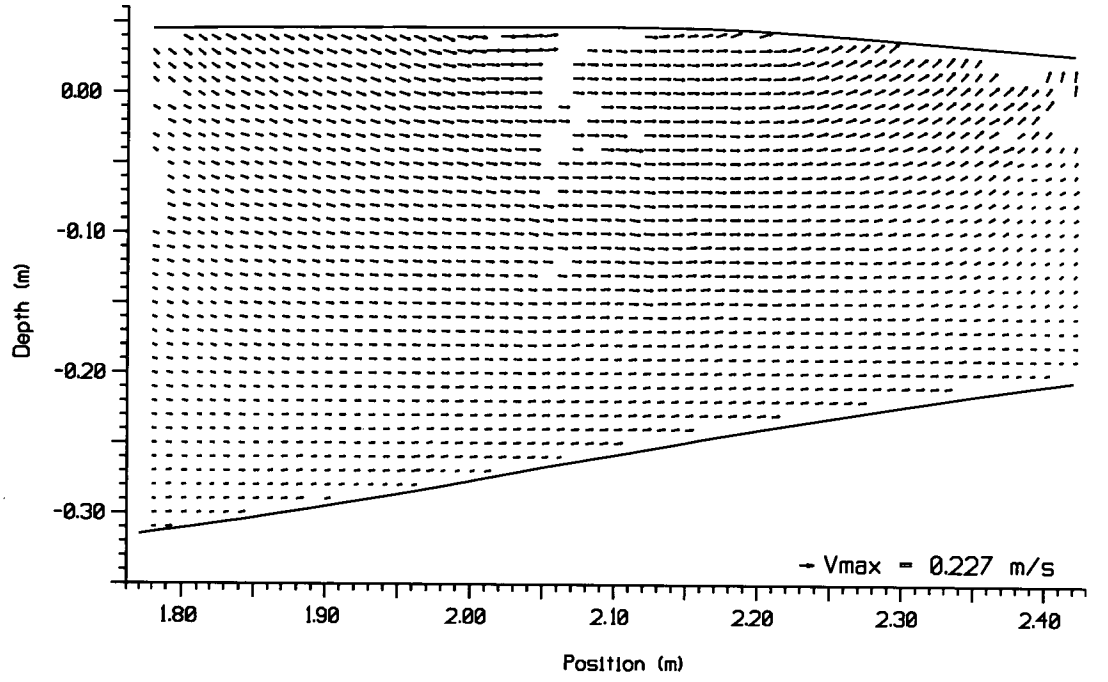

Figure 5.11: Wave 2: Position 4: Phase 1

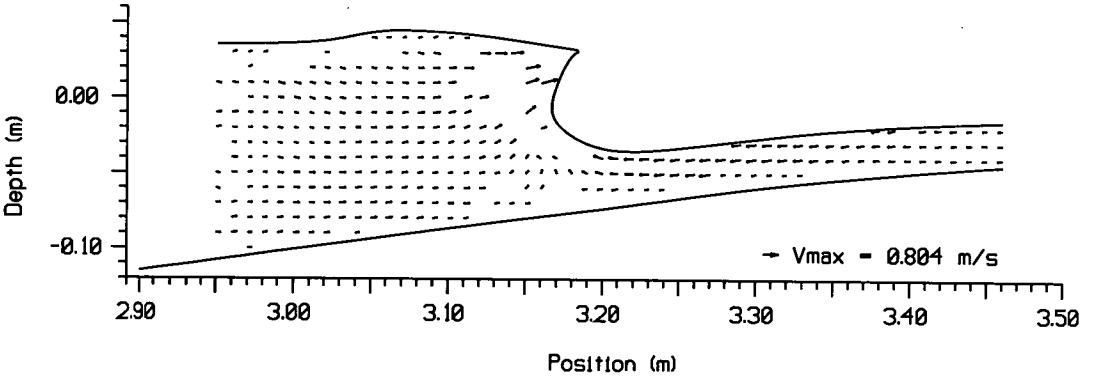

Figure 5.12: Wave 2: Position 6: Phase 3

waves we can verify that the maximum velocity has once again reduced with the amplitude of the wave.

Looking at the maximum velocity measured in the plunging breaker shown in figure 5.16 one can see that it actually exceeds that of the larger waves. However, in this case vector values were obtained closer to the tip of the plunging breaker. The turning of the backwash into the front face of the wave is also shown clearly.

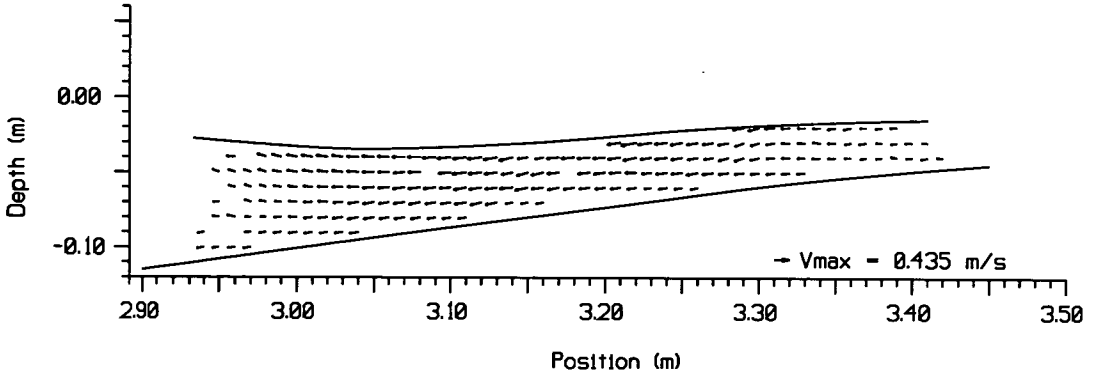

Figure 5.13: Wave 2: Position 6: Phase 2

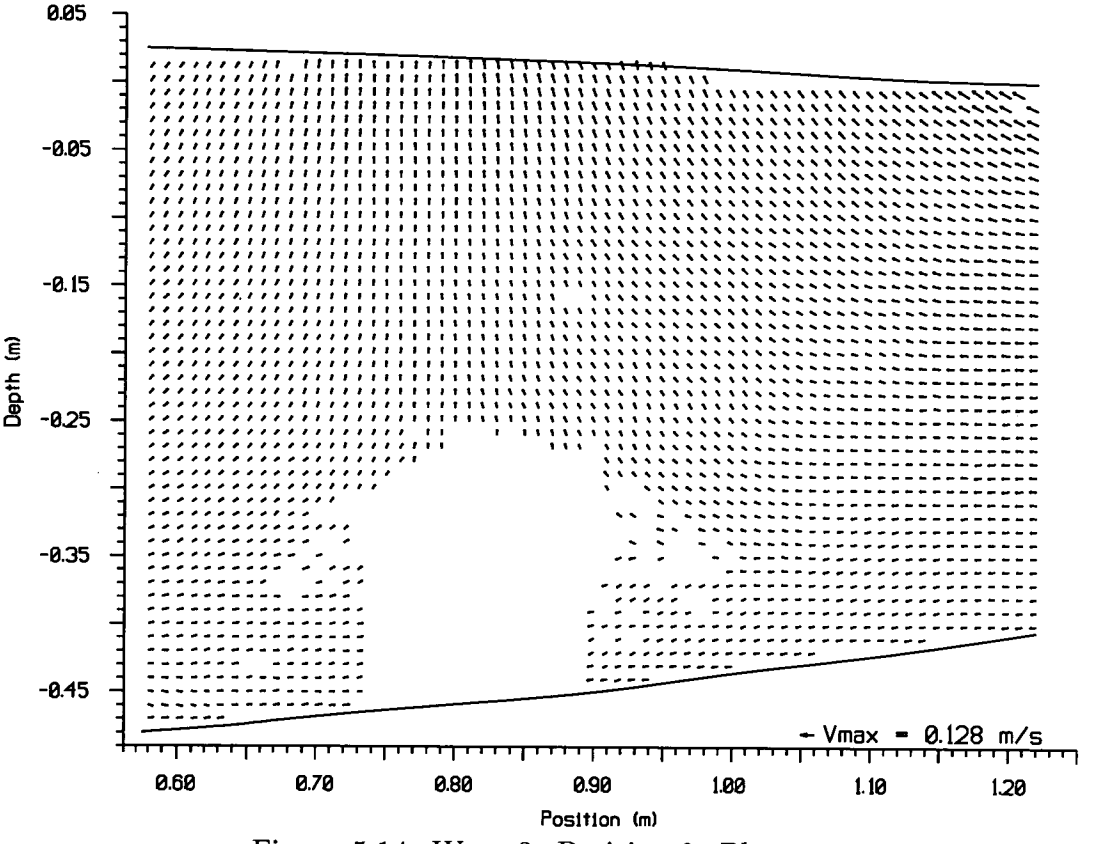

Figure 5.14: Wave 3: Position 2: Phase 3

In figure 5.17 the interaction of the backwash and the incoming wave is shown very clearly.

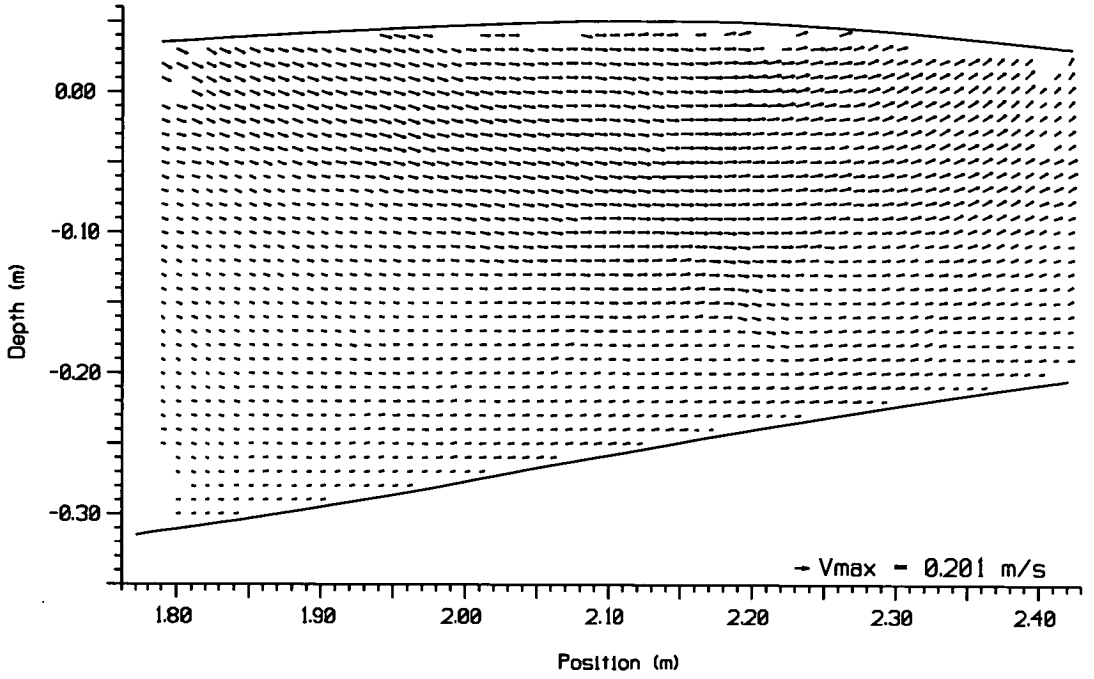

Figure 5.15: Wave 3: Position 4: Phase 2

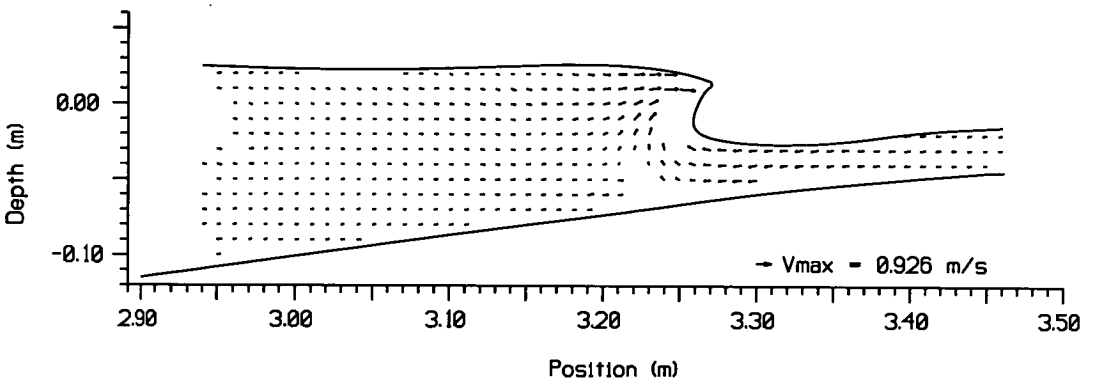

Figure 5.16: Wave 3: Position 6: Phase 4

5.3 Experiments on Profiled Beach 2

Measurements were made at five positions along the beach of the three wave conditions listed in table 5.2. At each measurement position four phases of each wave were recorded.

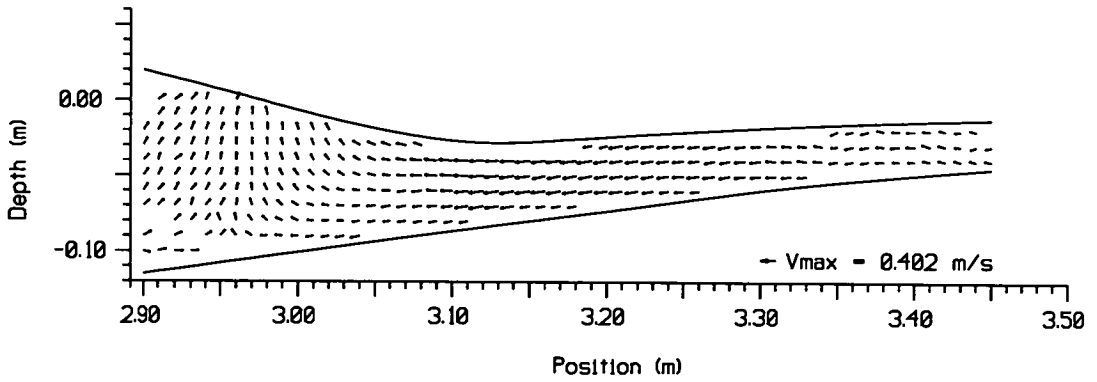

Figure 5.17: Wave 3: Position 5: Phase 3

5.3.1 Wave Breaking on Profile 2: A Description

The actual form of the breaking wave varies considerably between the two beaches and, to a lesser degree, between the different waves. On Profile 2 surging breakers are formed, to some extent, for all three waves examined. Only the smallest wave shows any real overturning, and even this is very low on the face of the wave. The breaking crests from each wave are shown in the photographs in figures 5.18, 5.19 & 5.20.

The formation of the, perhaps expected, plunging wave is suppressed by the fast-flowing backwash from the previous wave and breaking occurs where the incoming wave and backwash meet, ie. near the bottom of the wave, just offshore of the top of the bar. The broken wave then surges up the beach where it is almost totally reflected by the steep face of the scarp. The substantial backwash component is further emphasised by the short length of the surf zone, when compared to Beach 1, terminated by the steep faced scarp just above the SWL. The effect of this scarp is to rapidly halt the run-up, resulting in the backwash being formed very quickly after the wave has broken. The interaction of the backwash and the incoming breaker half way along the surf zone leads to the formation of a standing wave (see figure 5.21) being driven by the incoming wave and the reflection off the near-vertical face of the scarp. This interaction causes a greater than normal return flow which prevents the formation of plunging breakers, by forcing the wave to break lower down its face in the region where the backwash meets the

incoming wave. This general method of breaking is adopted by all three waves, although the smallest, Wave 3, does show a degree of overturning, as can be seen in Photograph 5.20, but this is still confined to the bottom of the wave. Recalling Profiled Beach 1, which has a relatively long surf zone, the increased length of run-up gives time for the incoming wave to break before the backwash is completely formed, resulting in the observed plunging breakers.

The formation of a "standing wave" in the surf zone will be affected greatly by multi-frequency waves, not only because they all, by definition, have different periods but also because they will break in different positions.

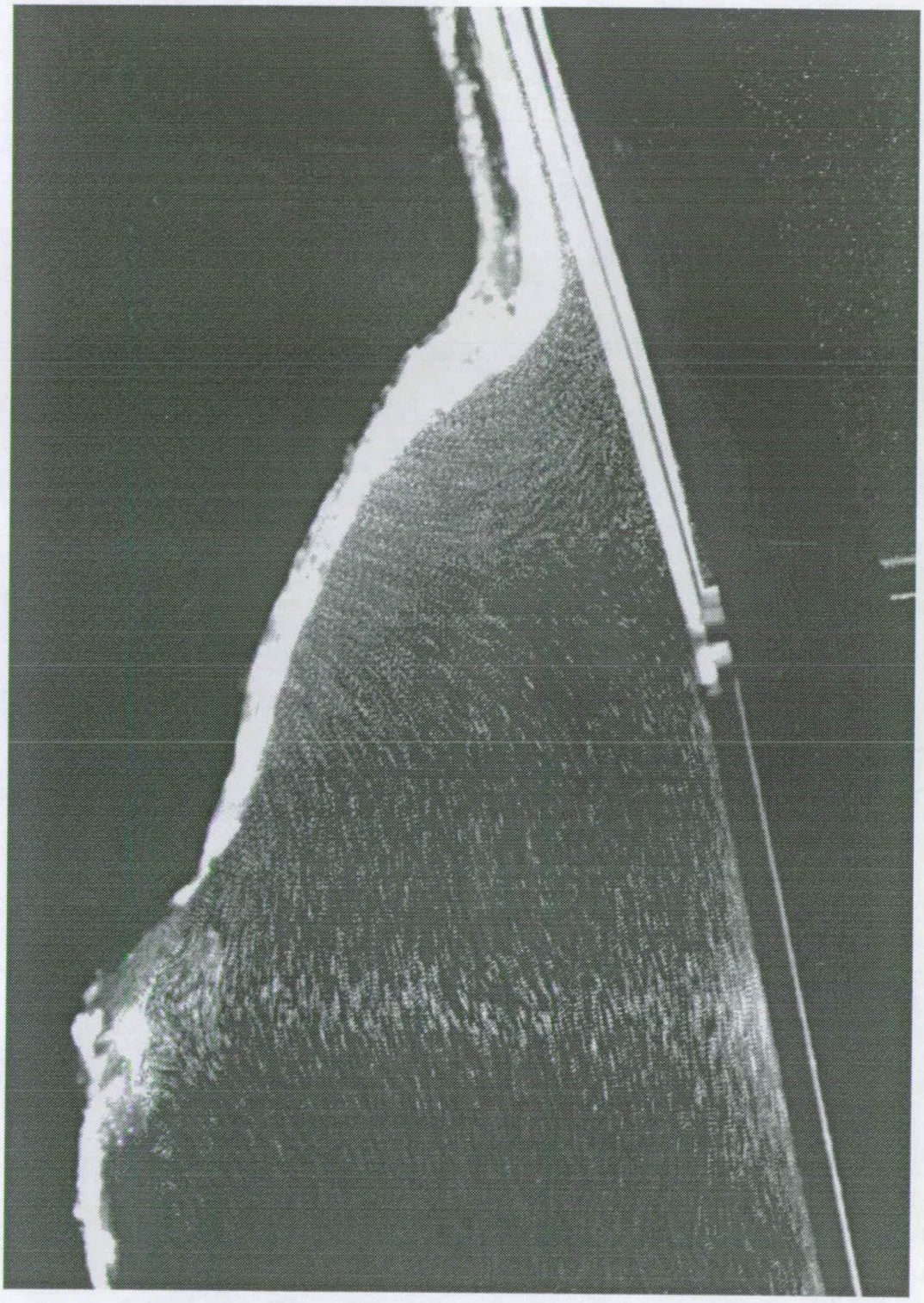

Figure 5.18: Wave 1 Breaking on Profile 2: f=0.655 Hz, H=0.063m

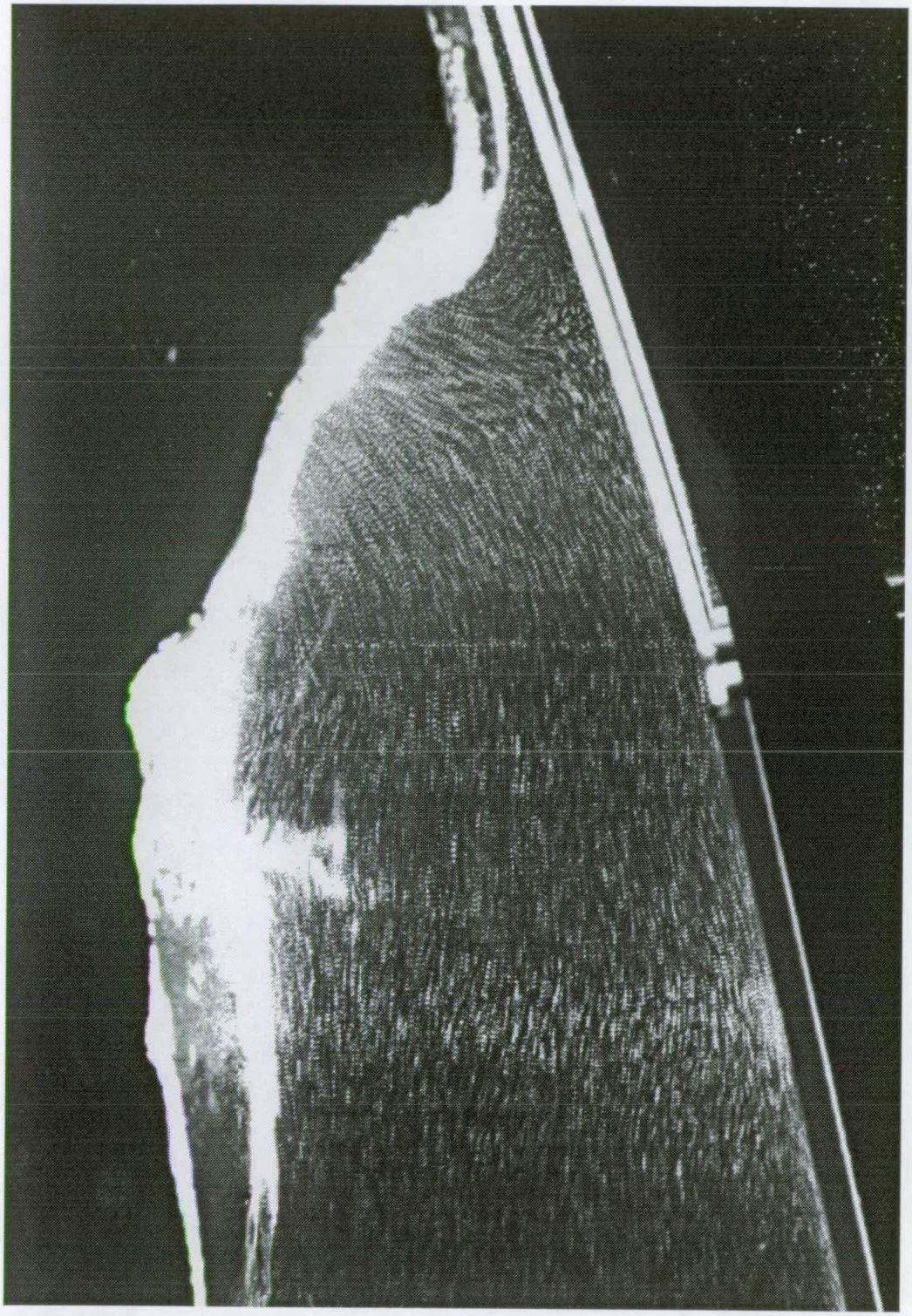

Figure 5.19: Wave 2 Breaking on Profile 2: f=0.66 Hz, H=0.050m

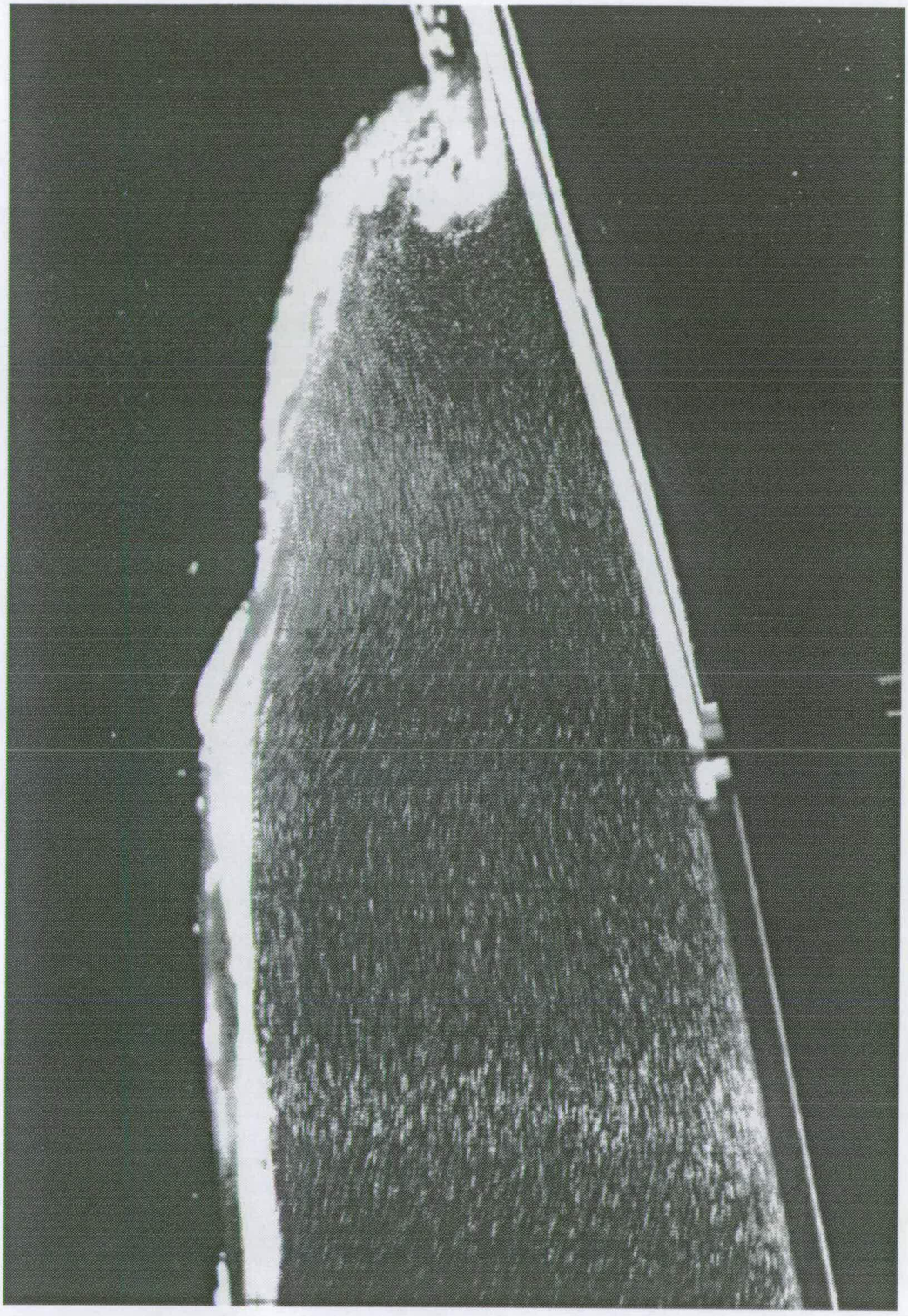

Figure 5.20: Wave 3 Breaking on Profile 2: f=0.64 Hz, H=0.040m

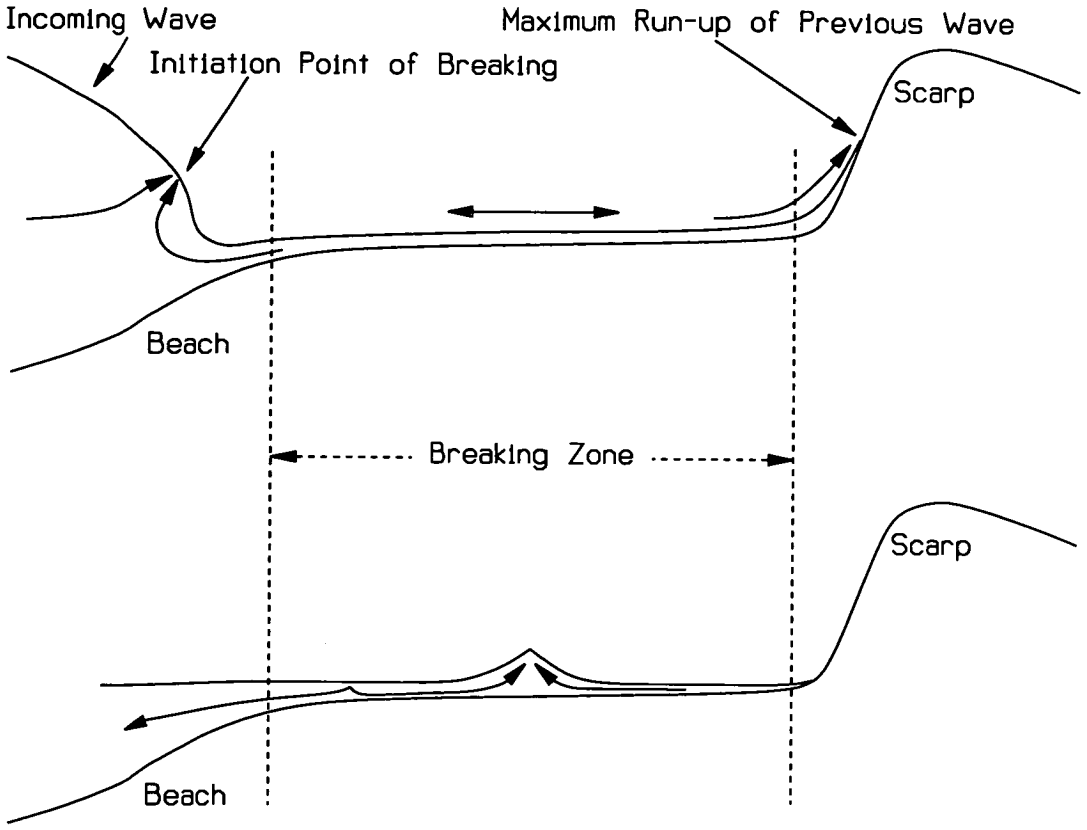

Figure 5.21: "Standing Wave" formation in the Surf Zone

5.3.2 Velocity maps for Profiled Beach 2

Once again only a small selection of the sixty vector maps available are presented; four from each wave. Apart from the crest and backwash at breaking, there are two others representing different phases at different positions on the beach. Dealing first with Wave 1, figure 5.22 shows the crest phase near the foot of the beach.

In figure 5.23 the crest has just passed through the measurement zone and the rear face of the wave is shown. The transition from the dominant negative vertical velocity, under the zero-down-crossing, to the negative horizontal velocity in the trough can be seen clearly.

Figure 5.24 shows Wave 1 breaking in the surging manner described in section 5.3.1. As on Profiled Beach 1, the very high accelerations, where the thin

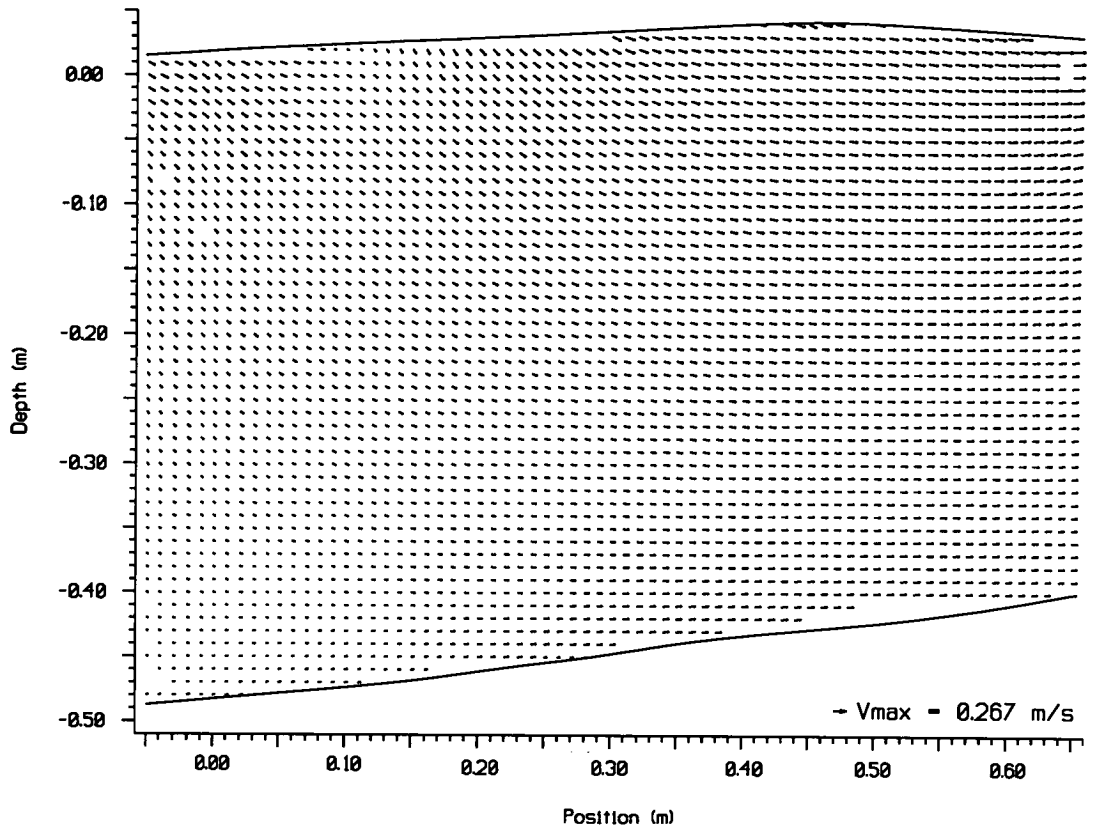

Figure 5.22: Wave 1: Position 1: Phase 3

layer of fast-flowing backwash meets the in-coming wave, create a velocity gradient which is too high for PIV to resolve; consequently there are no measurements in this area.

The backwash from this wave is shown in figure 5.25 and the reflected turbulence can be seen as a smoothly varying fluctuation superimposed on the main returning flow.

Turning our attention to Wave 2, we can see the crest phase at the foot of the beach in figure 5.26. One can see evidence of a reflected wave from the deformation of the free surface around $x = 0.42$m and the orientation of the group of vectors below.

The rear face of the wave at position three is shown in figure 5.27.

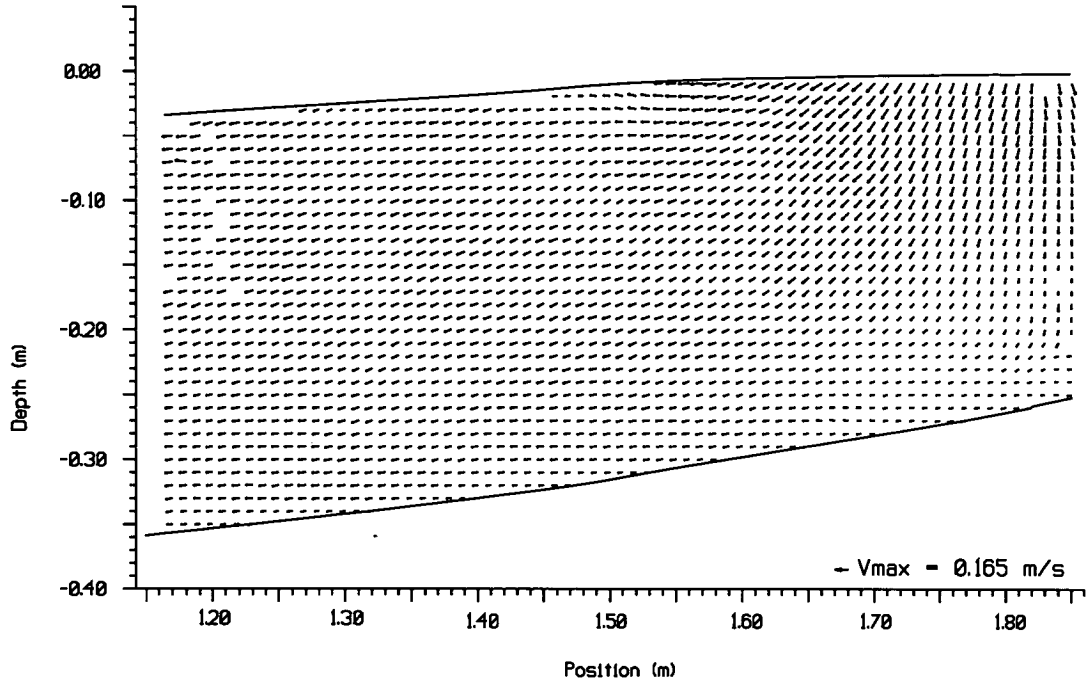

Figure 5.23: Wave 1: Position 3: Phase 2

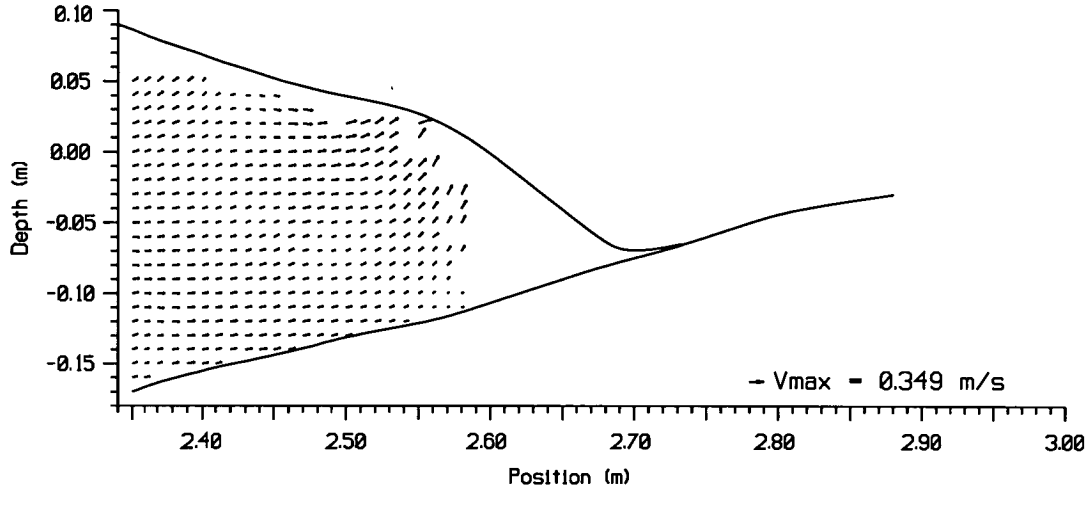

Figure 5.24: Wave 1: Position 5: Phase 2

The breaking wave is shown in figure 5.28. Although the form of the wave is similar to that of Wave 1 it breaks slightly further up the beach in shallower water, as would be expected considering it has a smaller wave height than Wave 1.

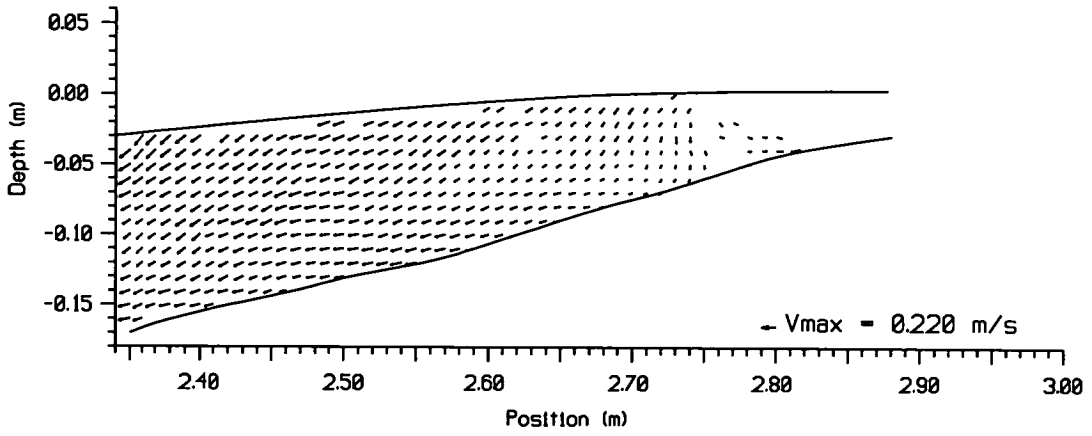

Figure 5.25: Wave 1: Position 5: Phase 4

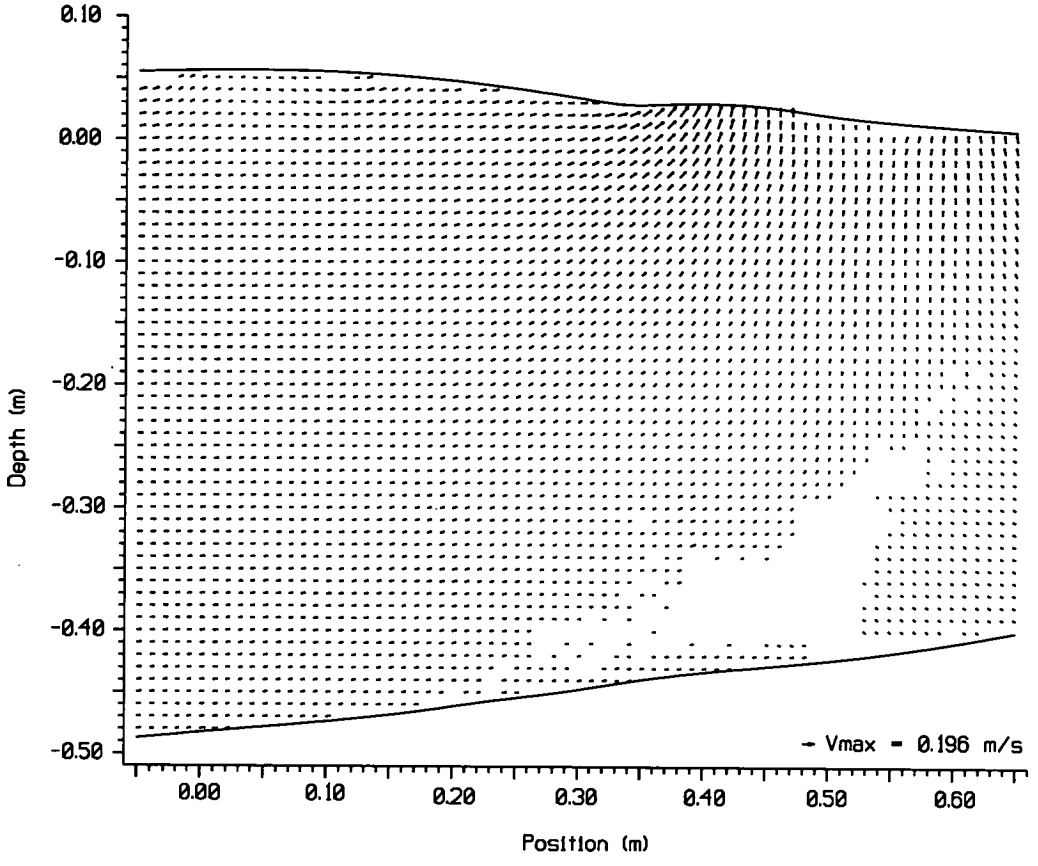

Figure 5.26: Wave 2: Position 1: Phase 2

The corresponding return flow at Position 5 can be seen in figure 5.29, once again showing the turbulence caused by breaking being returned back into the flow.

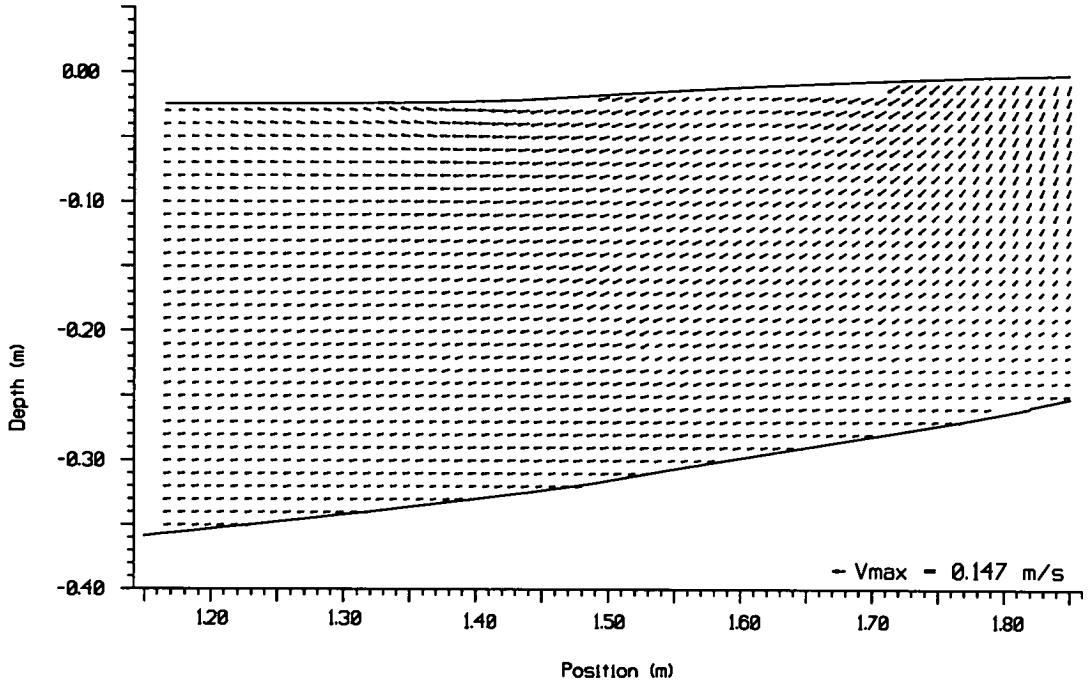

Figure 5.27: Wave 2: Position 3: Phase 2

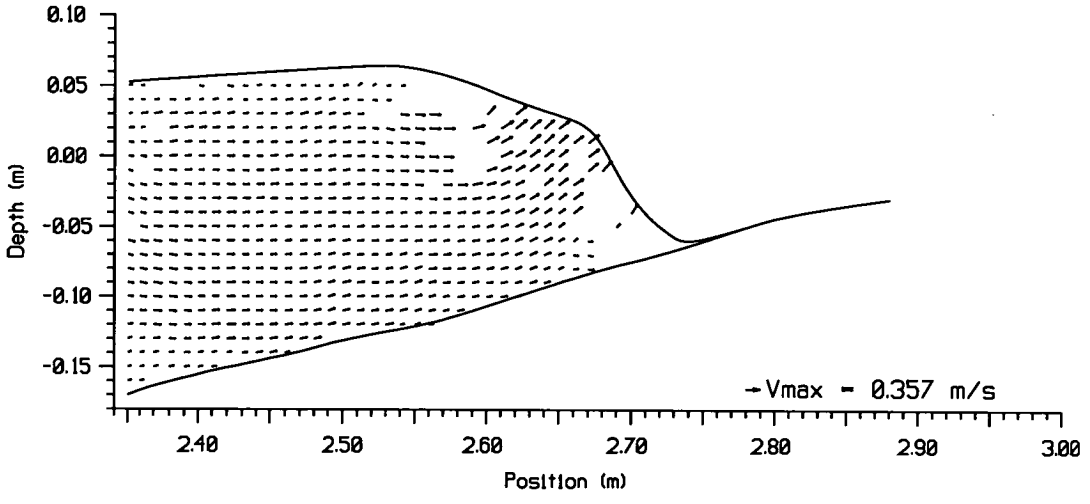

Figure 5.28: Wave 2: Position 5: Phase 2

Finally we consider Wave 3. Figure 5.30 shows the crest phase at Position 2 and figure 5.31 shows the front face of the wave at Position 4. Here one can see the transition from strongly negative horizontal flow, through a region of dominant positive vertical velocity, to the positive horizontal velocity associated with the incoming crest.

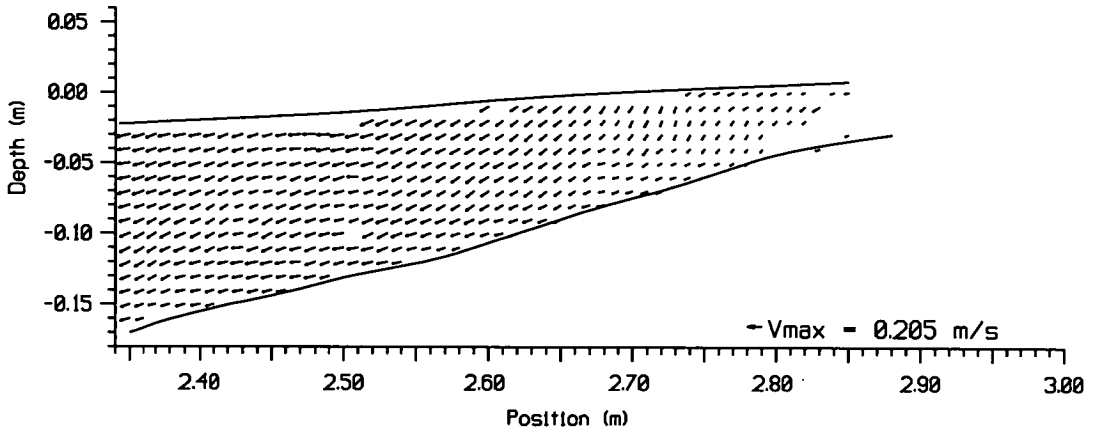

Figure 5.29: Wave 2: Position 5: Phase 4

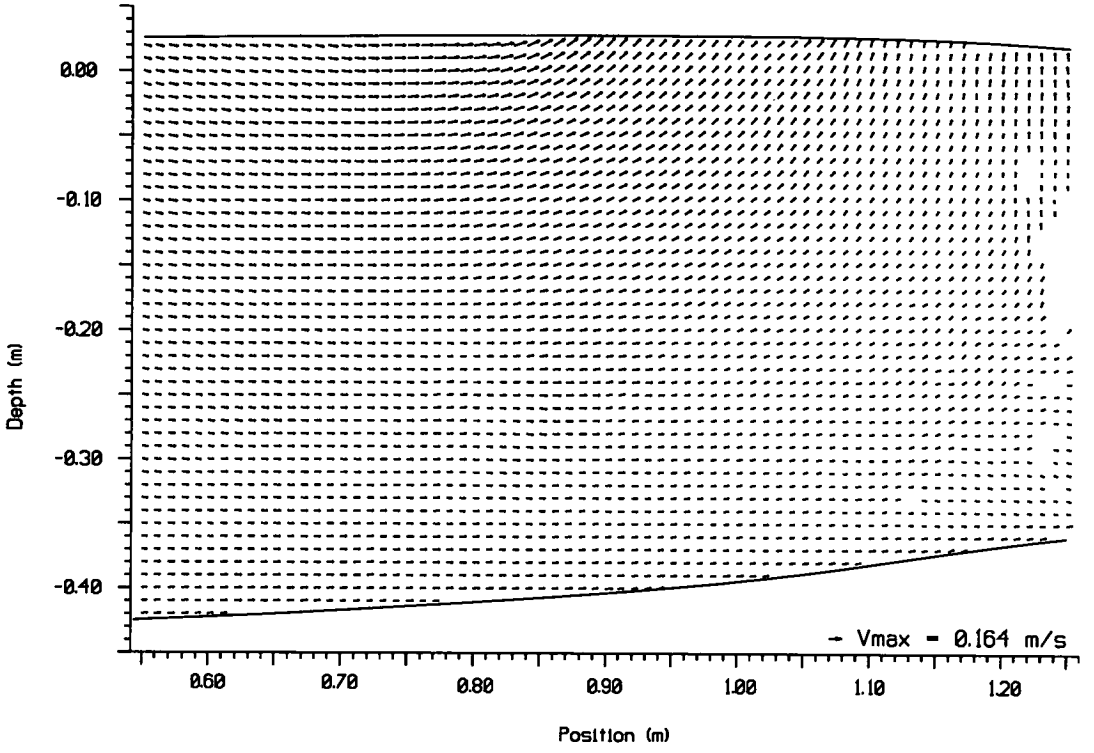

Figure 5.30: Wave 3: Position 2: Phase 4

Figures 5.32 & 5.33 show the breaker and backwash respectively in Wave 3. This is the only one of the three waves which displays any significant overturning of the front face. One must assume that this is due to the weaker backwash component from this smaller wave.

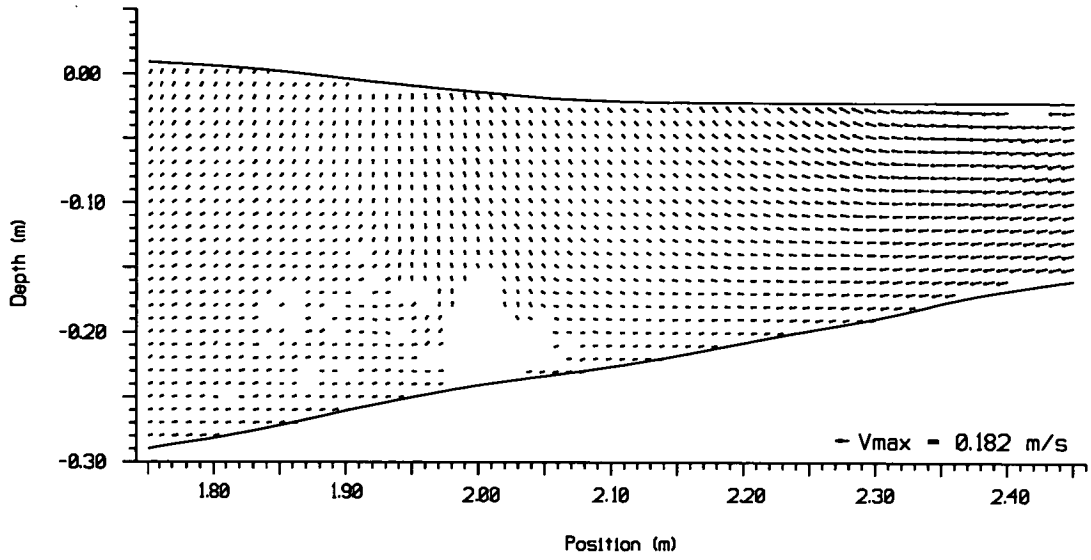

Figure 5.31: Wave 3: Position 4: Phase 1

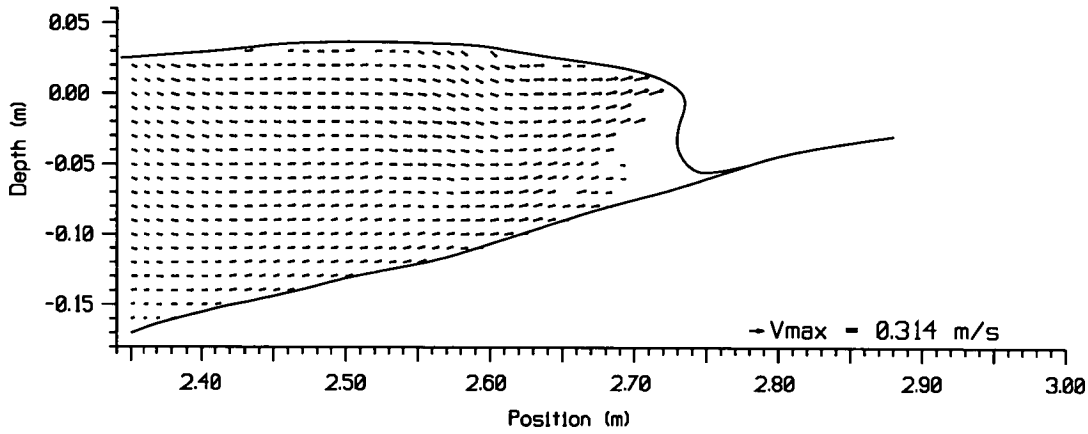

Figure 5.32: Wave 3: Position 5: Phase 3

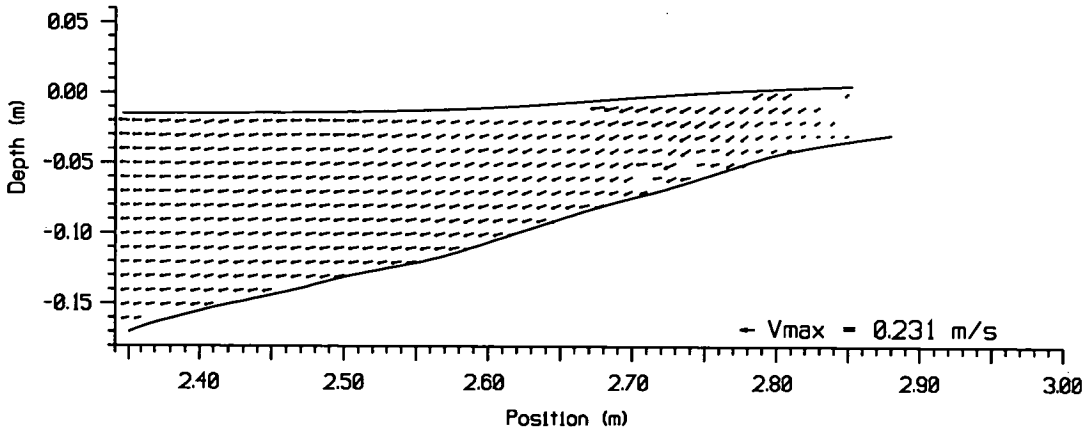

Figure 5.33: Wave 3: Position 5: Phase 1

5.4 Near-bed Velocity Inter-comparisons

The actual movement of sediment by the wave kinematics is determined by the bed shear stress τ (Simons et al., 1992, Sleath, 1987) which is given in equation 5.40 (Sleath ,1987,1991),

$$\tau = \rho\epsilon\frac{dU}{dy} \tag{5.40}$$

where ϵ is the eddy viscosity given in equation 5.41 (for the case of no current) and U is the horizontal component of velocity at the bed.

$$\epsilon = v'l \tag{5.41}$$

In equation 5.41, v' is the root mean squared (rms) fluctuation of the vertical velocity component and l is the turbulence mixing length. In the vicinity of the bed $l \propto y$, however, the constant of proportionality can vary. The normally quoted value is 0.4 in clear water, even in combined waves and currents (Kemp & Simons (1982, 1983). However, Sleath (1990) found that for oscillatory flow the constant was between 0.1 and 0.2 over most of the boundary layer. Given that the velocities closest to the bed in the vector maps shown in this and the previous chapter, start near the top of the boundary layer *not* at the bed itself, τ cannot be calculated accurately. A further point to consider is the nature of the boundary layer itself. As the experiments to measure the velocities have been carried out on a smooth beach the boundary layer is most likely to be laminar. However, the experiments which generated the profiles modelled (Powell (1988)) were carried out on a movable beach with relatively large material sizes; this could easily create a turbulent boundary layer and would definitely create a thicker one. For these two reasons the calculation of bed shear stresses is not appropriate, however, one could look at the near-bed maximum magnitudes of velocity, *above the boundary layer*, to give an indication of the differences which give rise to beach movement.

The approach here is to examine the maximum and minimum velocities which occur under the crest and the trough respectively, for the three waves measured. This is really only possible because the frequencies of the waves are so close together that the crests and troughs of all three waves occur in approximately the same place. There is, however, occasionally a slight mismatch and so to minimise this effect and to reduce the influence of any localised turbulence present, a horizontal average is carried out for each row of vectors, throughout the vertical profile of each wave, over 5 to 10 columns of vectors. For example, to provide the profile from Wave 3 in figure 5.36, each row of vectors in figure 5.15 is averaged from $x = 2.00$m to $x = 2.10$m.

The figures are split into four separate graphs; the first shows the average profiles of the horizontal component of velocity for all three waves. The other three graphs show the individual average profile for each wave $\pm$ 1 standard deviation (eg. figure 5.35). The latter gives an idea of the local uniformity of the flow and, in some cases, helps indicate the top of the boundary layer, as the flow above it tends to have less fluctuation: see, for example, Wave 2 in figure 5.44. The influence of the boundary layer can be clearly seen in a number of the figures where the velocity reduces sharply near the bottom of the profile: eg. figures 5.36, 5.44 & 5.47.

Once again we shall give the comparisons from the two beach profiles separately and then comment on both at the end.

5.4.1 Near-bed Velocity Inter-comparisons for Profiled Beach 1

The locations on the beach where the intercomparisons are carried out are shown in figure 5.34.

Figures 5.35 to 5.41 are given with reference to the positions shown in figure 5.34.

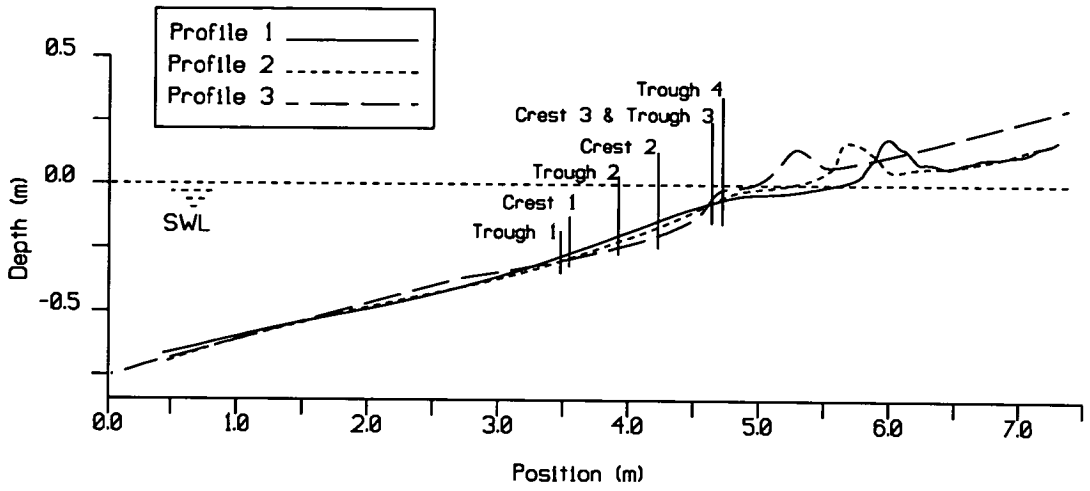

Figure 5.34: The Positions of the Velocity Intercomparisons on Beach 1.

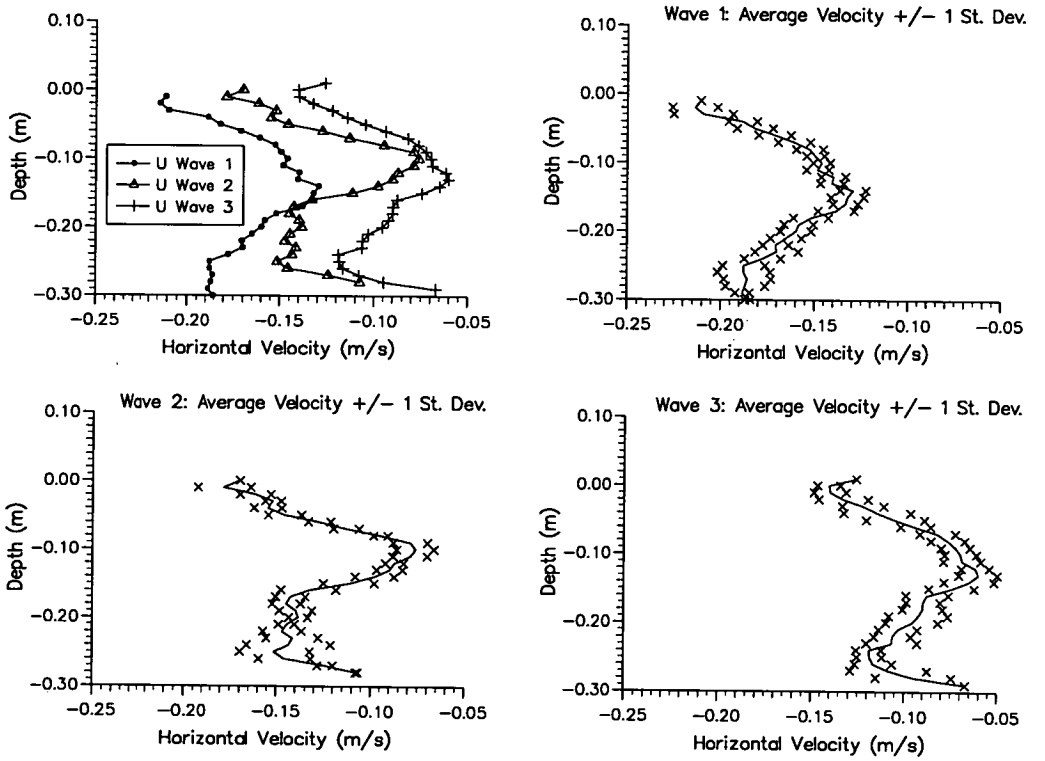

Figure 5.35: Velocity comparison on Beach 1. Position: Trough 1 ($h = 0.28$m)

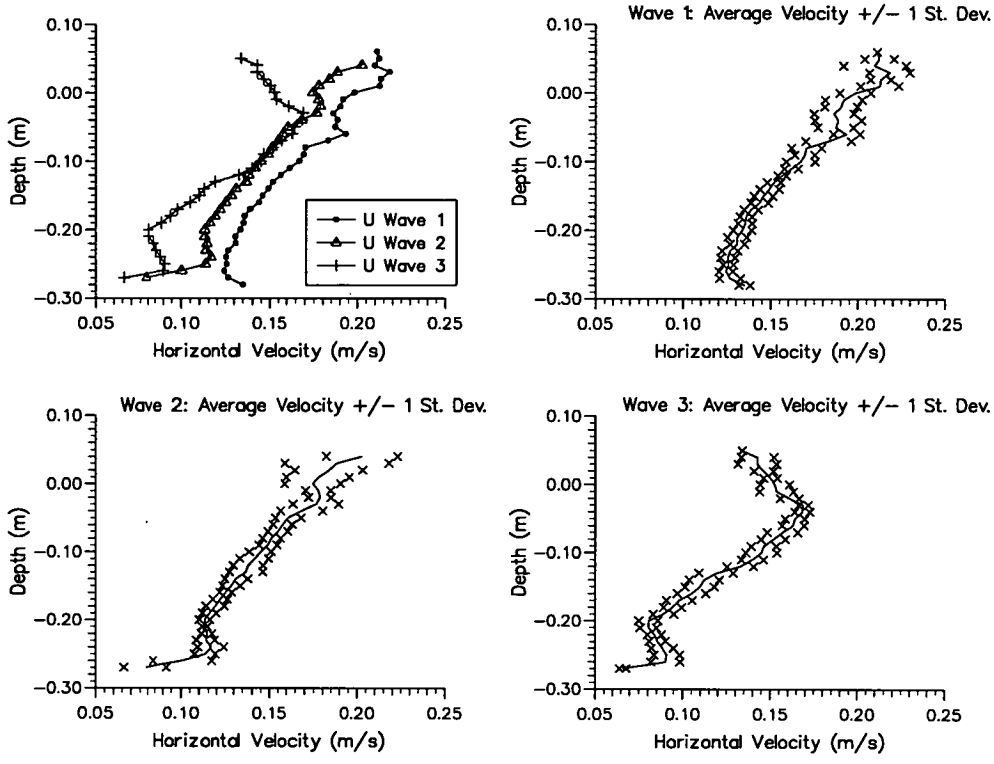

Figure 5.36: Velocity comparison on Beach 1. Position: Crest 1. ($h = 0.27$m)

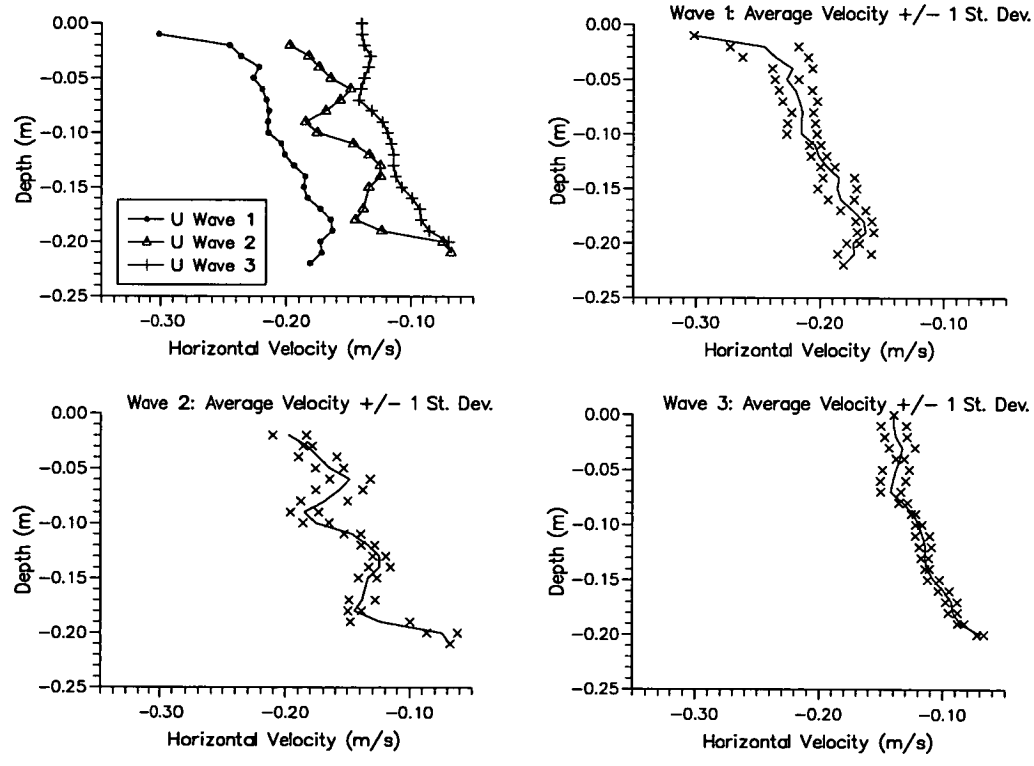

Figure 5.37: Velocity comparison on Beach 1. Position: Trough 2. ($h = 0.20$m)

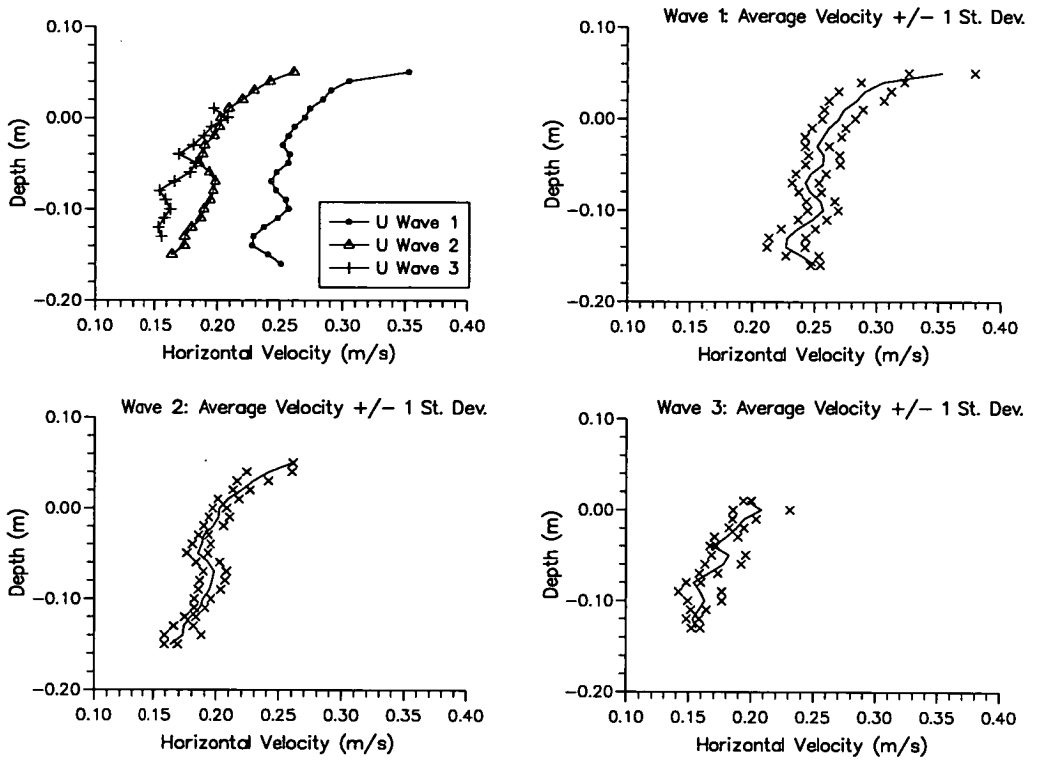

Figure 5.38: Velocity comparison on Beach 1. Position: Crest 2. ($h = 0.14$m)

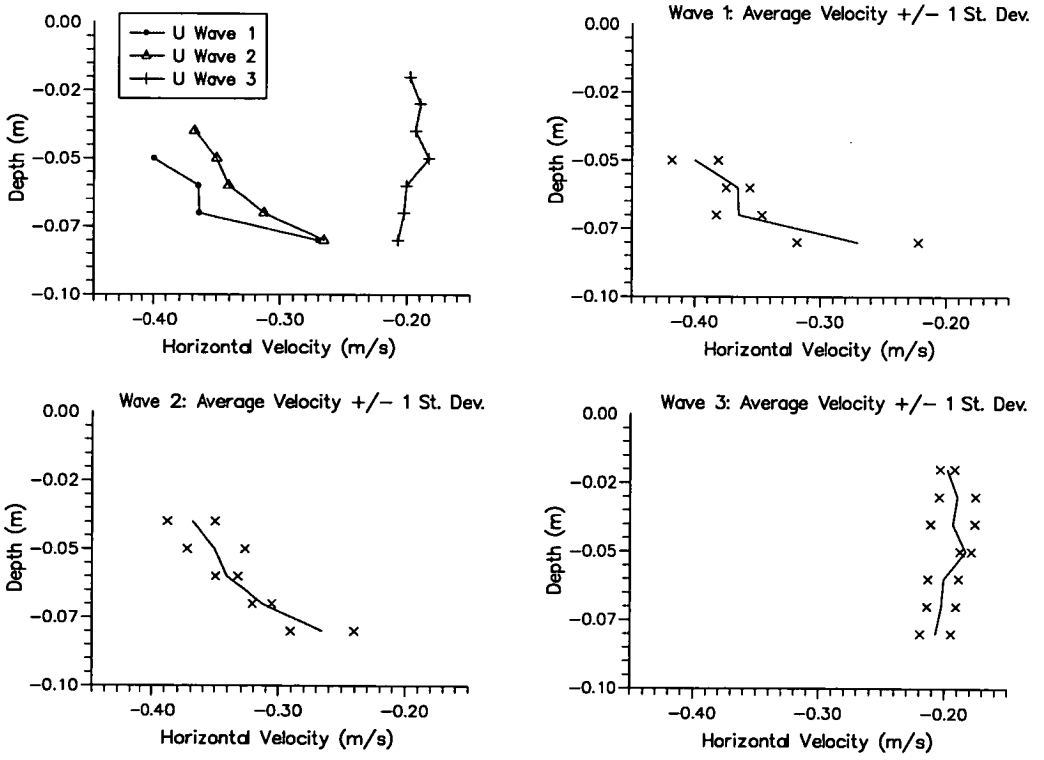

Figure 5.39: Velocity comparison on Beach 1. Position: Trough 3. ($h = 0.07$m)

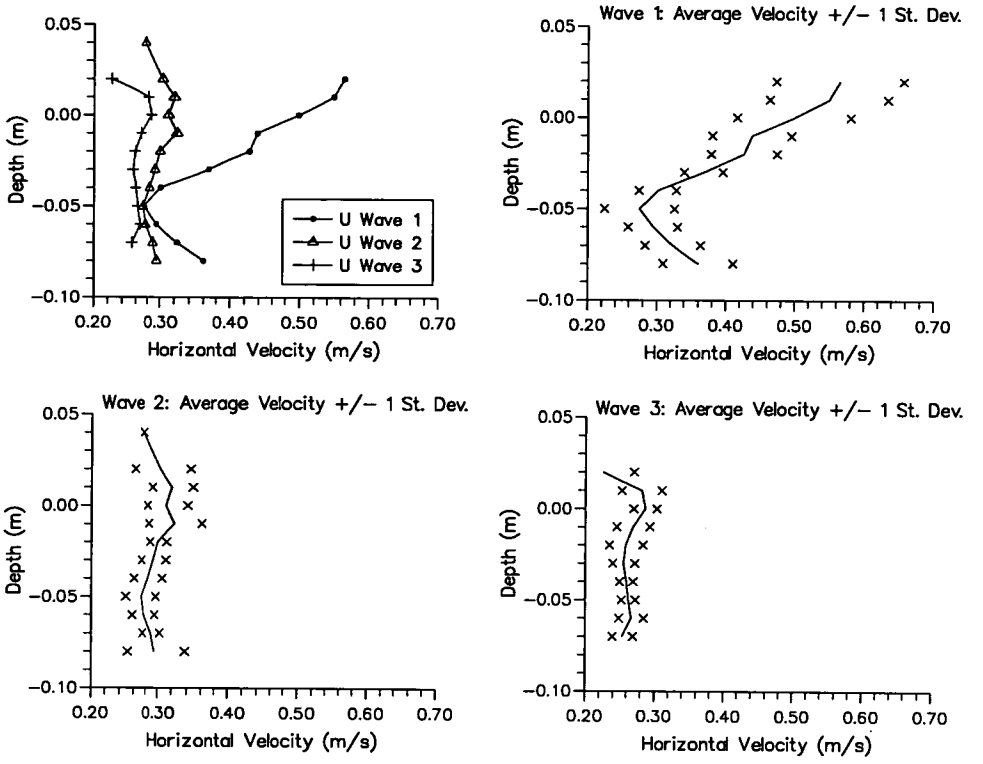

Figure 5.40: Velocity comparison on Beach 1. Position: Crest 3. ($h = 0.07$m)

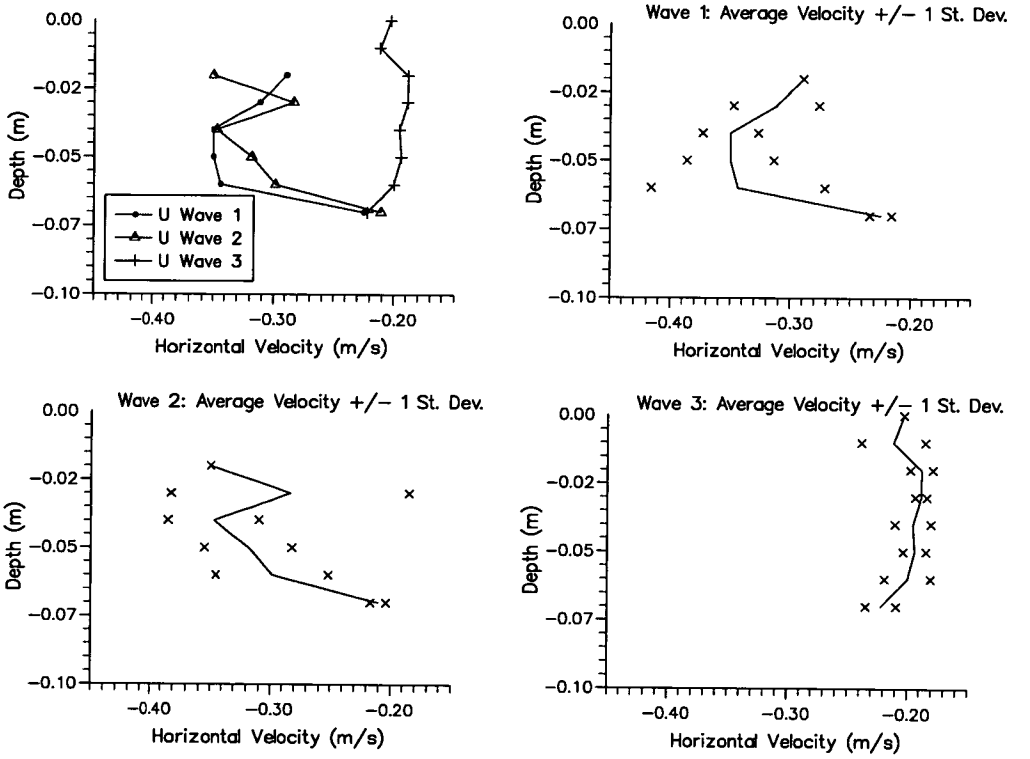

Figure 5.41: Velocity comparison on Beach 1. Position: Trough 4. ($h = 0.06$m)

5.4.2 Near-bed Velocity Inter-comparisons for Profiled Beach 2

In the same way the velocity comparisons from the positions marked on figure 5.42, are shown in figures 5.43 to 5.48.

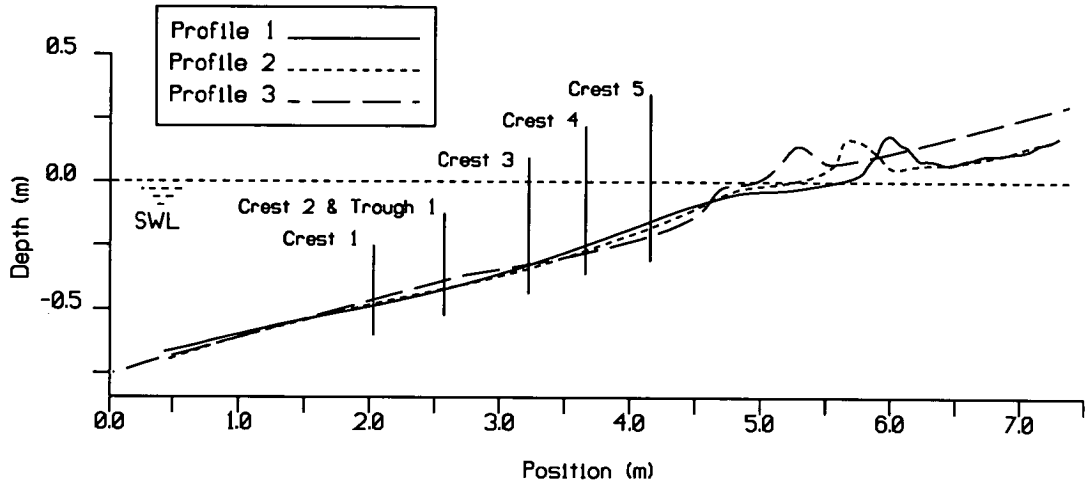

Figure 5.42: The Positions of the Velocity Intercomparisons on Beach 2

5.4.3 Comments on the Near-Bed Velocity Intercomparison

Dealing first with the general features observed for both beaches, one can see that where the beach height is almost identical for the three profiles (See Crest 1 in figure 5.34 and Crest 3 in figure 5.42), the near bed velocities under the crest are remarkably similar for all three waves: see figures 5.40 & 5.46. The same is also true for Trough 3 on figure 5.34 shown in figure 5.39. As one might expect, the maximum differences between the three waves occur where there is a distinct difference in height of the three beach profiles; for example, figure 5.48, at Crest 5 shown in figure 5.42.

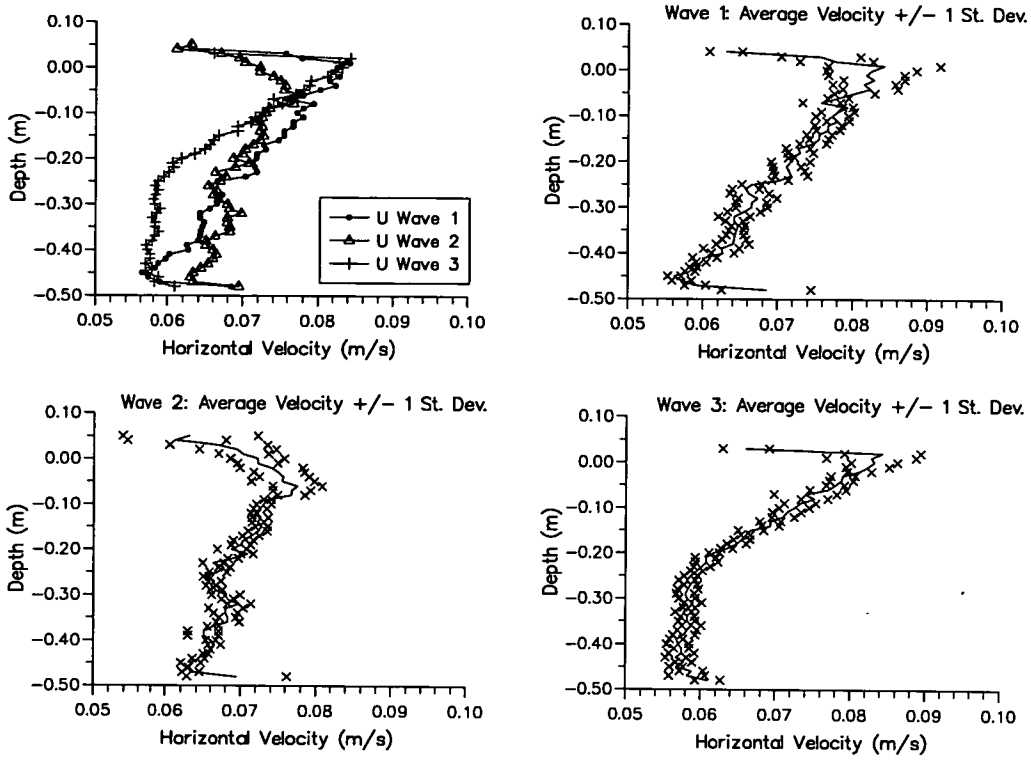

Figure 5.43: Velocity comparison on Beach 2. Position: Crest 1. ($h = 0.48$m)

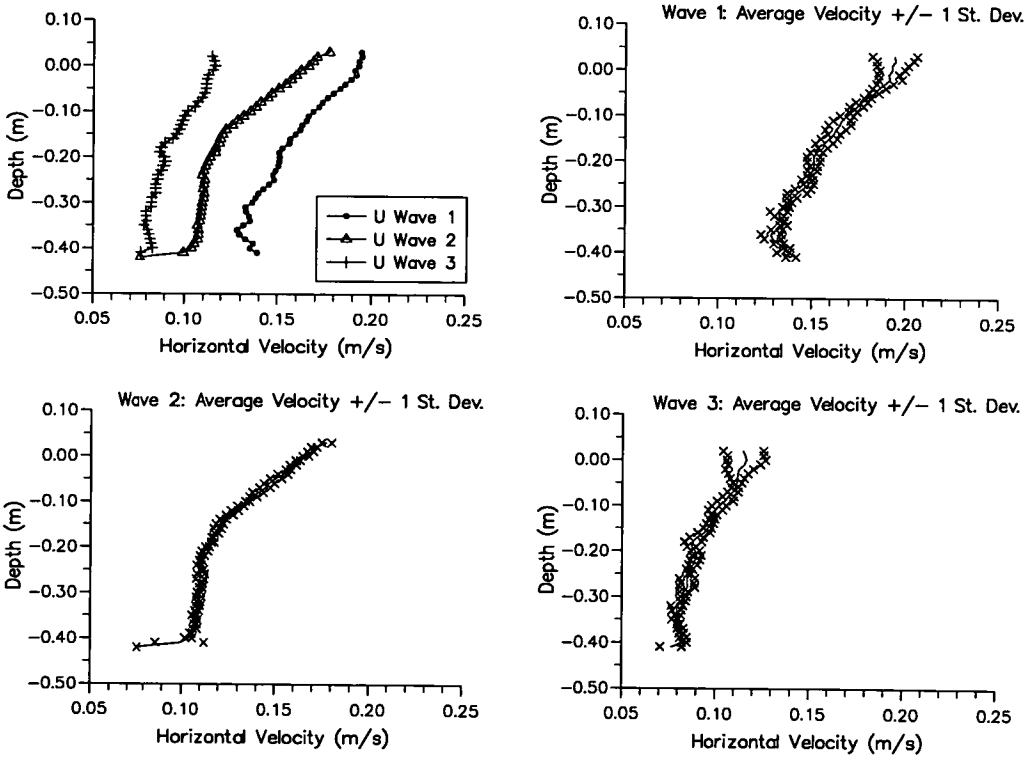

Figure 5.44: Velocity comparison on Beach 2. Position: Crest 2. ($h = 0.42$m)

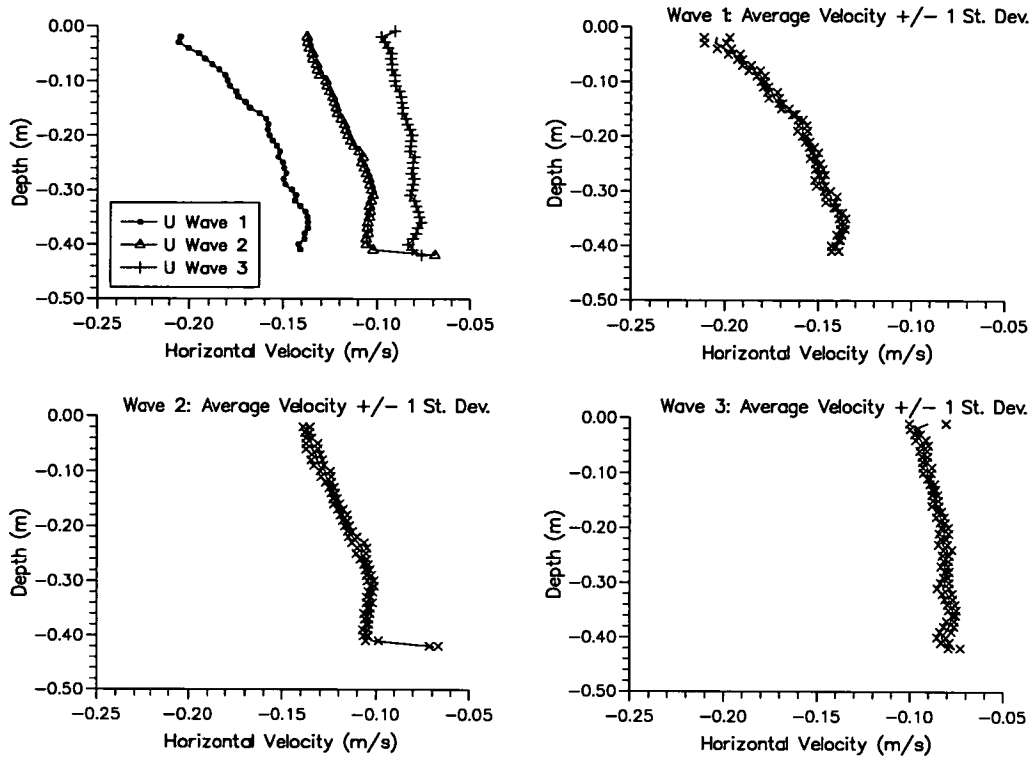

Figure 5.45: Velocity comparison on Beach 2. Position: Trough 1. ($h = 0.42$m)

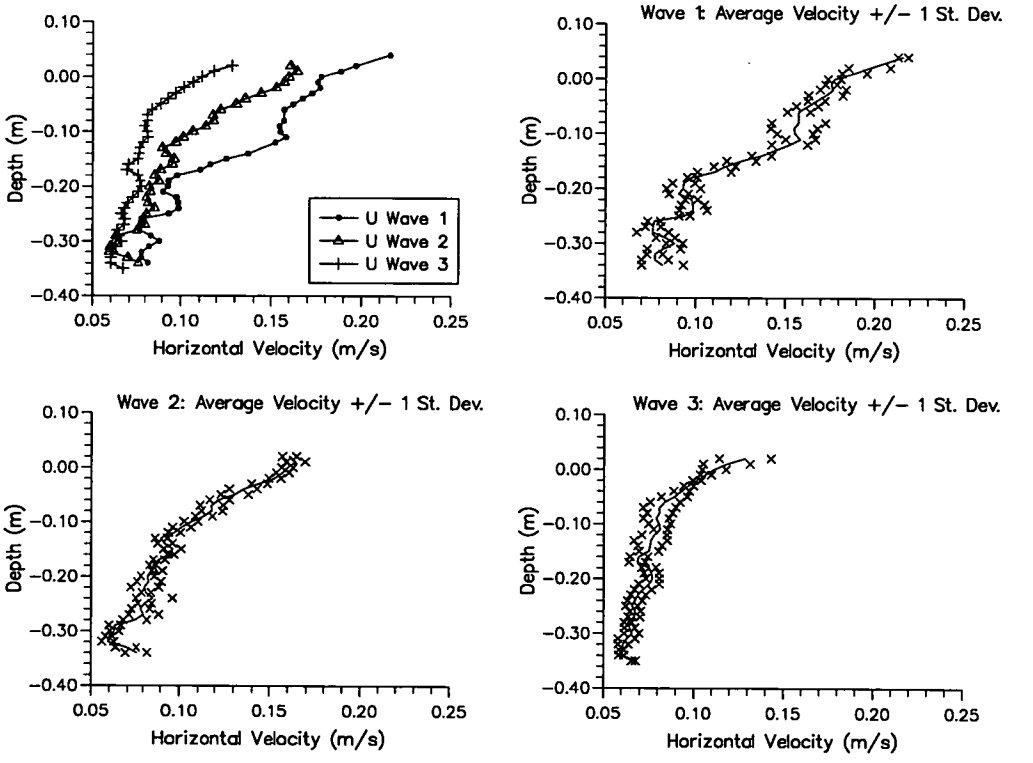

Figure 5.46: Velocity comparison on Beach 2. Position: Crest 3. ($h = 0.34$m)

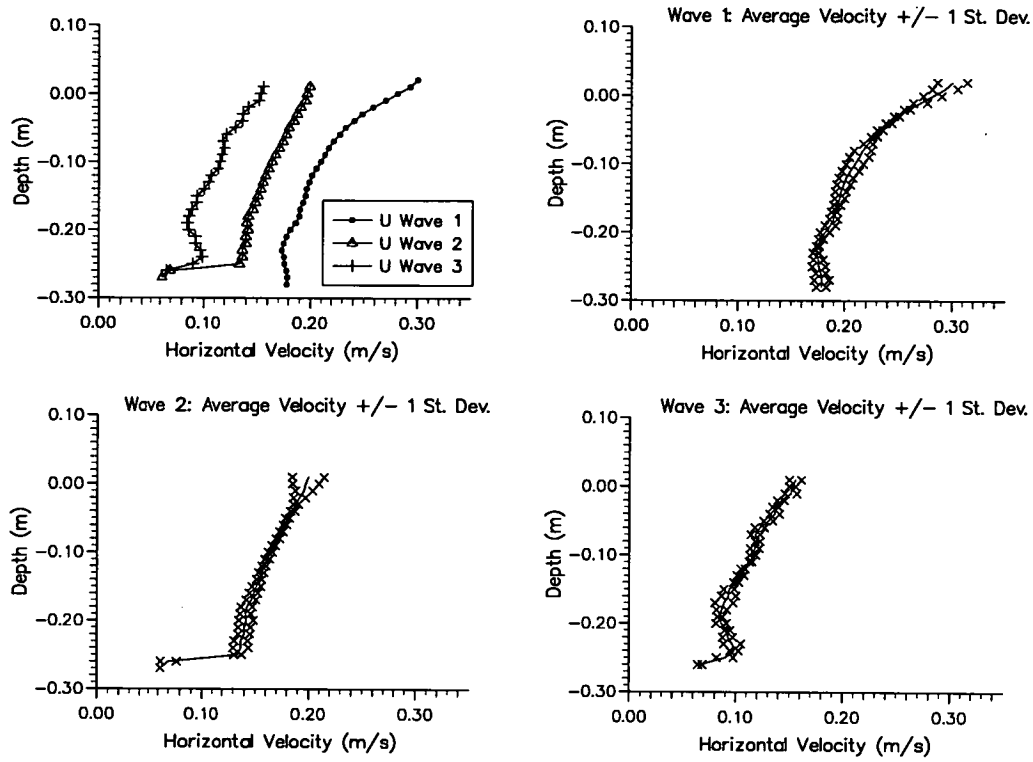

Figure 5.47: Velocity comparison on Beach 2. Position: Crest 4. ($h = 0.27$m)

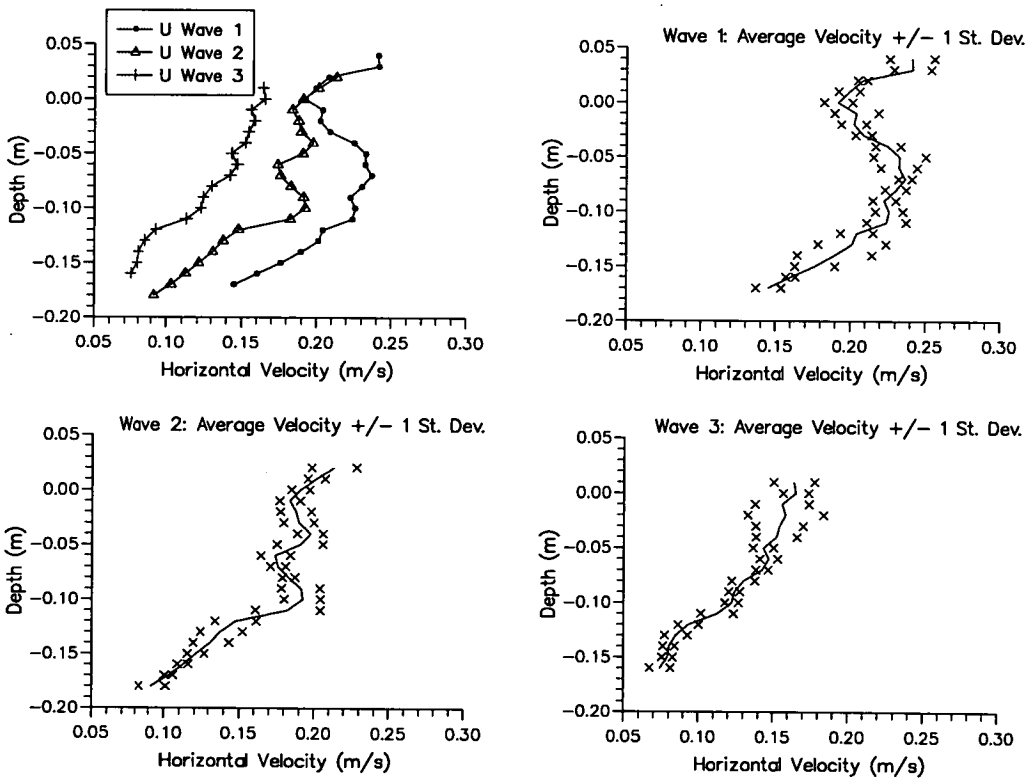

Figure 5.48: Velocity comparison on Beach 2. Position: Crest 5. ($h = 0.18$m)

If one tries to examine the relative magnitudes of the positive and negative horizontal velocities, associated with the crest and trough phases of the wave, with the purpose of trying to describe the on-shore and off-shore movement of sediment, one runs into the problem that it is easier to move sediment down the slope, in the offshore direction, than it is to move it on-shore. The degree to which this is true depends on the local slope of the beach and consequently varies along its length. An equilibrium profile is reached when the relative on-shore and off-shore sediment motions balance all along the beach. Looking at Crest 2 and Trough 1, which occur at identical positions on Beach 2 (in figure 5.42), one can see that the magnitudes of the positive and negative near-bed velocities for each wave match almost identically. If we assume that the relative on-shore and offshore motions of Wave 2 (which is matched to Beach 2) balance then one can interpret the smaller velocities of Wave 3 as being below the threshold to induce sediment movement one way or the other and the larger velocities of Wave 1 to cause offshore sediment motion because, although the relative magnitudes of positive and negative horizontal velocity are about the same, it is easier to move sediment down the slope than it is to move it up.

An interesting factor of the formation of surging breakers on Beach 2 due to the very thin, fast-flowing backwash is that the near-bed velocity at breaking (Crest 5 on figure 5.34) is lower than the previous position (Crest 4 on the same figure) because of this interaction with the backwash. As the surf zone on Beach 1 is wider and plunging breakers are formed, the horizontal near-bed velocity increases to a maximum at breaking (figure 5.40). Another point to note here is that the maximum magnitude of the backwash, at Trough 4 in figure 5.34, is once again almost exactly the same as under Crest 3.

One can also compare the velocities from the same waves at similar horizontal positions on the two different beaches. Examining the crest and trough positions shown in figures 5.34 & 5.42 one can see that Crests 1 and 2 on Beach 1 are at the same positions as Crests 3 and 5 on Beach 2, respectively: these comparative positions will now be termed Locations 1 and 2 respectively. The first thing to notice is that at Location 2 on Beach 2, the waves are approaching breaking;

which is not the case for this location on Beach 1. One would therefore expect significantly different velocities for the waves at this location on the two beach profiles; indeed, all the waves show a significantly smaller near-bed velocity on Beach 2 due to the larger backwash component. The velocities in the near-surface region are also smaller on Beach 2 although, with the exception of Wave 1, these differences are not as marked as in the near-bed region. One may infer from this that the breaking evident on Beach 2 is triggered by the interaction with the fast-flowing backwash of the previous wave rather than directly from the beach shape. Going further offshore to Location 1, one can still find a smaller near-bed velocity component for Beach 2 suggesting that the backwash is still having an effect on the incoming wave, however, the near-surface velocities are very similar for all three waves.

Chapter 6

Conclusions

6.1 Main Conclusions

With reference to the aims set out in section 1.2, the following conclusions have been made:

1. *General:* The ability of PIV to obtain accurate and detailed velocity measurements of waves breaking on beaches has been clearly shown. The only real problems which arose in this study, were from areas of near-zero velocity and/or high acceleration; both of these problems can be dealt with using image shifting techniques or adjusting the photographic magnification. In larger-scale waves, the increased aeration of the water during breaking, may limit the extent of the measurement region.

2. *Theoretical Comparisons on Mildly Sloping Beaches:* An examination of the way that the Boussinesq and Serre models deal with the vertical profile of the horizontal component of velocity has been carried out on 1:30 and 1:100 plane, sloping beaches. In general the parabolic equation governing the velocity profile was found to be satisfactory, especially near the bed. However, the near-surface velocities were consistently over-estimated in the crest region. The discrepancy between the profiles of measured and modelled

values, in this near-surface region, increased logarithmically as the wave travelled up the beach; ie. with increasing wave non-linearity.

3. *Boussinesq and Serre Model Velocity Predictions:* The spatial distribution of the depth-averaged horizontal velocity has been predicted, at two positions on the 1:30 beach, by the Boussinesq and Serre Models (developed by Brocchini & Drago of Snamprogetti SpA, Italy). The predictions agree quite well with the measured values. However, the sensitivity in calculating the second spatial derivative of the depth-averaged velocity, as required to produce a vertical profile of velocity, means that even a small difference in the prediction of the depth-averaged velocity can cause a large difference in the calculated near-surface velocity.

4. *Integral Property Calculations from PIV Measurements:* The calculation of the radiation stress, mean energy flux and mean momentum flux from PIV velocity data has been carried out. The mean momentum flux decreases linearly up the beach. There is some scatter evident in radiation stress and mean energy flux distributions, although the magnitude and general trends for both are in agreement with Stive & Wind (1982). It is proposed that this scatter is due mainly to the discrete "step-like" representation of the free surface caused by analysing the PIV negatives on a regular grid of points. This introduces a relatively large error in the calculation of the potential energy.

5. *Wave Kinematics on the Profiled Beaches:* The two beach profiles produced two different types of breakers, namely surging and plunging, from the same initial wave conditions. The proposed reasons for this are discussed in some detail, with the length of the surf zone, the impermeability of the beach and the fact that regular waves were used, being the main factors involved. A number of velocity vector maps are shown from both beaches for all three waves and the magnitudes of their near-bed maxima are compared at several positions. It was found that the near-bed velocities were very similar at positions where the height of all three beaches were approximately the same, and there were significant differences at other locations. The influence these

differences might have on the local area of the beach, ie. whether erosion or accretion is occurring or not, is discussed.

6.2 Future Recommendations

6.2.1 PIV Considerations

1. *Image Shifting:* This technique, which was briefly mentioned in the text, should be used to resolve zero and near-zero velocities (effectively improving the measurable dynamic range); and to overcome the problem of directional ambiguity. Indeed, the author has already used such a system in the measurement of waves breaking over a submerged breakwater (Petti et al., 1994).

2. *Video/Digital PIV:* The next major step forward will be the transition from film-based to video-based PIV, when one can capture and store full-field PIV images at a high frame rate. Only recently has a CCD video camera been available with a resolution capable of imaging very small seeding particles in the scale of flow measured here. This camera has a 2048 x 2048 pixel CCD array, which is suitable for this scale of PIV, however, the fact that it produces such large images (in terms of computer memory – each frame is approximately 4.5 Mbytes) still limits the temporal resolution of the system at the moment. Fast computers installed with video-cards having large amounts of memory would seem to be the best way of addressing this problem. The advent of digitised PIV images, formed either directly from a CCD camera or scanned into a computer from a photograph or negative, has already realised software capable of analysing an image at 18 points per second, which compares rather favourably with the 2s per point system described in this thesis. The ability to obtain a higher temporal resolution while maintaining the same spatial resolution would certainly be a major advantage.

6.2.2 Hydrodynamic Considerations

1. *Beach Roughness and Impermeability:* Whilst the main effect on the incoming wave field is the shape of the beach, the effects of beach roughness and permeability need to be examined, particularly when considering shingle beaches.

2. *Irregular Waves:* The use of bi-chromatic or tri-chromatic waves, on both types of beach, would seem a logical next step to provide a more realistic wave field; indeed this is already being undertaken. If the limited temporal resolution of taking PIV pictures can be overcome then irregular wave spectra could also be measured. In the mean time it has been shown that for the calculation of the integral properties more phase positions need to be recorded in order to reduce the horizontal domain over which averaging is carried out; this would enable the spatial derivative of the radiation stress to be calculated.

3. *Bottom Boundary-layer Measurements:* As was pointed out in section 5.4.3 the bed shear stress could not be calculated from the PIV measurements made because penetration into the boundary layer could not be determined. However, at a much larger magnification it should be possible to measure the boundary layer velocity distribution with PIV. Care should be taken to make sure the characteristics of the boundary layer to be measured are representative of the boundary layer at full scale.

Chapter 7

Bibliography

1. Adrian, R.J. (1991) *Particle Imaging Techniques for Experimental Fluid Dynamics.* Ann. Rev. Fluid Mech., 23:261-304.

2. Basco, D.R. (1985)*A Qualitative Description of Wave Breaking.* J. Waterways, Ports & Coastal Engineering, 111(2):171-199.

3. Basco, D.R., Bellomo, D.A. & Pollock, C. (1992) *Statistically Significant Beach Profile Changes With and Without the Presence of Seawalls.* Proc. Int. Conf. Coastal Eng., 148:1924-1937.

4. Battjes, J.A. (1974) *Surf Similarity* Proc. Int. Conf. Coastal Eng., pp 466-480.

5. Battjes, J.A. (1988) *Surf-Zone Dynamics.* Ann. Rev. Fluid Mech., 20:257-293.

6. Beji, S. & Battjes, J.A. (1993) *Experimental Investigations of Wave Propagation over a Bar.* Coastal Engineering, 19(2), 151-162.

7. Brocchini, M., Drago, M. & Iovenitti, L. (1992) *The Modelling of Short Waves in Shallow Waters: Comparison of Numerical Models Based on Boussinesq and Serre Equations.* Proc. Int. Conf. Coastal Eng., 4:76-89.

8. Bruce, T. & Easson, W.J. (1992) *The Kinematics of Wave Induced Flows Around Near-Bed Pipelines.* Proc. Int. Conf. Coastal Eng., 229:2990-2998.

9. Chaplin, J.R. (1980) *Developments of Stream Function Wave Theory.* Coastal Engineering, 3:179-205.

10. Cokelet, E.D. (1977) *Steep Water Waves in Water of Arbitrary Uniform Depth.* Phil. Trans. R. Soc. A 286:183-230.

11. Copeland, G.J.M. (1985) *Practical Radiation Stress Calculations Connected with Equations of Wave Propagation.* Coastal Engineering, 9:195-219.

12. Creed, C.G., Dalrymple, R.A., Kriebel, D.L. & Kaihatu, J.A. (1992) *Equilibrium Beach Profiles with Random Seas.* Proc. Int. Conf. Coastal Eng., 152:1973-1986.

13. Dally, W.R. & Dean, R.G. (1984) *Suspended Sediment Transport and Beach Profile Evolution.* J. Waterways, Ports & Coastal Engineering, 110(1):15-33.

14. Dally, W.R., Dean, R.G. & Dalrymple, R.A. (1985) *Wave Height Variation Across Beaches of Arbitrary Profile.* J. Geophys. Res., 90:C6:11,917-11927.

15. Dean, R.G. (1965) *Stream Function Representation of Non-Linear Ocean Waves.* J. Geophys. Res., 70(18):4561-4572.

16. Dean, R.G. & Perlin, M. (1986) *Intercomparison of Near-Bottom Kinematics by Several Wave Theories and Field and Laboratory Data.* Coastal Eng. 9: 399-437.

17. Dean, R.G., Srinivas, R. & Parchure, T.M. (1992) *Longshore Bar Generation Mechanisms.* Proc. Int. Conf. Coastal Eng., 154:2001-2014.

18. Dingemans, M.W. (1994a) *Comparison of Computations with Boussinesq-like models and Laboratory Measurements.* MAST-G8M note: Report H1684.12, Delft Hydraulics.

19. Dingemans, M.W. (1994b) *Water Wave Propagation over Uneven Bottoms.* PhD Thesis, Technical University of Delft. *To be published under the same title by World Scientific, Singapore.*

20. Dold, J.W. & Peregrine, D.H. (1984) *Steep, Unsteady Water-waves: an Efficient Computational Scheme.* Proc. Int. Conf. Coastal Eng., 955-967.

21. Dold, J.W. & Peregrine, D.H. (1986) *An Efficient Surface-Integral Algorithm for Unsteady Water Waves.* Numerical Methods for Fluid Dynamics *II*, Morton, K.W. & Baines M.J. (Eds), Oxford University Press, 671-679.

22. Draper, L. (1963) *Derivation of a "Design Wave" from Instrumental records of Sea Waves.* Proc. Inst. Civil Eng. 26:291-304.

23. Earnshaw, H.C. (1993) Private Communication.

24. Fenton, J.D. (1979) *A High-Order Cnoidal Wave Theory.* J. Fluid Mech., 94:129-161.

25. Fenton, J.D. (1989) *Nonlinear Wave Theories. The Sea,* Vol. 9; Ocean Engineering Science. Le Mehaute, B. & Hanes, D.M. (Eds.) Wiley, New York.

26. Galvin, C.J. (1968) *Breaker Type Classification on three Laboratory Beaches.* J. Geophys. Res. 73:3651-3659.

27. Galvin, C.J. (1972) *Wave Breaking in Shallow Water.* In *Waves on Beaches and Resulting Sediment Transport.* Ed. R.E. Meyer, pp. 413-456. New York: Academic.

28. Gray, C., Skyner, D.J. & Greated, C.A. (1988) *The Measurement of Breaking Waves using Particle Image Velocimetry.* Proc. ICALEO Conf., Santa Clara, California.

29. Gray, C. & Greated, C.A. (1988) *The Application of Particle Image Velocimetry to the Study of Water Waves.* Optics and Lasers in Engineering, 9.

30. Gray, C. (1989) *The Development of Particle Image Velocimetry for Water Wave Studies.* PhD Thesis, University of Edinburgh.

31. Gray, C., Greated, C.A., McCluskey, D.R. & Easson, W.J. (1991) *An Analysis of the Scanning Beam PIV Illumination System.* Journal of Measurement Science and Technology, 2.

32. Gray, C. (1992) *The Evolution of Particle Image Velocimetry.* Proc. IMechE Conf., City University, London.

33. Greated, C.A., Easson, W.J., Quinn, P.A., Skyner, D.J. & She, K. (1992a) *Velocity Measurements under 2-D and 3-D Breaking Waves using Particle Image Velocimetry.* Proc. EC-MAST G6-M Final Workshop, Pisa, Italy.

34. Greated, C.A., Skyner, D.J. & Bruce, T. (1992b) *Particle Image Velocimetry (PIV) in the Coastal Engineering Laboratory.* Proc. Int. Conf. Coastal Eng., 15:212-225.

35. Griffiths, M.W.P., Easson, W.J. & Greated, C.A. (1992) *Measured Internal Kinematics for Shoaling Waves with Theoretical Comparisons.* J. ASCE, 118(3):280-299.

36. Guza, R.T. & Thornton, E.B. (1981) *Wave Set-up on a Natural Beach.* J. Geophys. Res., 86:C5:4133-4137

37. Hamm, L. (1992) *Directional Nearshore Wave Propagation over a Rip Channel: An Experiment.* Proc. Int. Conf. Coastal Eng., 16:226-239.

38. Hansen J. Buhr, & Svendsen, I.A. (1984) *A Theoretical and Experimental Study of Undertow.* Proc. Int. Conf. Coastal Eng., 151:2246-2262.

39. Hedegaard, I.B., Roelvink, J.A., Southgate, H., Pechon, P., Nicholson, J. & Hamm, L. (1992) *Intercomparison of Coastal Profile Models.* Proc. Int. Conf. Coastal Eng., 162:2108-2121.

40. Jakobsen, M.L., Hossack, W.J., Greated, C.A. & Easson, W.J. (1992) *PIV Analysis Using an Optically Addressed Spatial Light Modulator.* Proc. Applied Optics and Opto-Electronics, Leeds, U.K.

41. Keane, R.D. & Adrian, R.J. (1990) *Optimization of Particle Image Velocimeters. Part I: Double Pulsed Systems.* Meas. Sci. & Tech. 1:1202-1215.

42. Keane, R.D. & Adrian, R.J. (1991) *Optimization of Particle Image Velocimeters. Part II: Multiple Pulsed Systems.* Meas. Sci. & Tech. Vol. 2.

43. Kemp, P.H. & Simons, R.R. (1982) *The Interaction between Waves and a Turbulent Current: Waves Propagating with the Current.* J. Fluid Mech., 116:227-250.

44. Kemp, P.H. & Simons, R.R. (1983) *The Interaction between Waves and a Turbulent Current: Waves Propagating against the Current.* J. Fluid Mech., 130:73-89.

45. Klein, M.V. & Furtak, T.E. (1986) *Optics* John Wiley & Sons, Inc., New York.

46. Klopman, G. (1988) *Numerical Simulation of Gravity Wave Motion on Steep Slopes.* Delft Hydraulics Report H195.

47. Klopman, G. (1990) *A Note on the Integral Properties of Periodic Gravity Waves in the case of a Non-Zero Eulerian Velocity.* J. Fluid Mech., 211:609-615.

48. Liberatore, G. & Petti, M. (1992) *Wave Transformations over a Submerged Bar: Experiments and Theoretical Interpretations.* Proc. Int. Conf. Coastal Eng., 32:447-459.

49. Longuet-Higgins, M.S. & Stewart, R.W. (1960) *Changes in the form of Short Gravity Waves on Long Waves and Tidal Currents.* J. Fluid Mech., 8:565-583.

50. Longuet-Higgins, M.S. & Stewart, R.W. (1961) *The changes in amplitude of Short Gravity Waves on Steady Non-uniform Currents.* J. Fluid Mech., 10:529-549.

51. Longuet-Higgins, M.S. & Stewart, R.W. (1962) *Radiation Stress and Mass Transport in Gravity Waves with Application to Surf Beats.* J. Fluid Mech., 13:481-504.

52. Longuet-Higgins, M.S. & Stewart, R.W. (1964) *Radiation Stress in Water Waves: a Physical Discussion with Applications.* Deep Sea Research, 11:529-562.

53. Longuet-Higgins, M.S. (1974) *On the Mass, Momentum, Energy and Circulation of a Solitary Wave.* Proc. R. Soc. Lond. A. 337:1-13.

54. Longuet-Higgins, M.S. & Fenton, J.D. (1974) *On the Mass, Momentum, Energy and Circulation of a Solitary Wave. II* Proc. R. Soc. Lond. A. 340:471-493.

55. Longuet-Higgins, M.S. (1975) *Integral Properties of Periodic Gravity Waves of Finite Amplitude.* Proc. R. Soc. Lond. A. 342, 157-174.

56. Longuet-Higgins, M.S. & Cokelet, E.D. (1976) *The Deformation of Steep Surface Waves in Water. A Numerical Method of Computation.* Proc. R. Soc. Lond. A. 350:1-26.

57. Longuet-Higgins, M.S. (1983) *Wave Set-up, Percolation and Undertow in the Surf Zone.* Proc. R. Soc. Lond. A. 390, 283-291.

58. McCluskey, D.R. (1992a) *An Optical Investigation of Air-Particle Flows* PhD Thesis, University of Edinburgh.

59. McCluskey, D.R. (1992b) Private Communication.

60. McCluskey, D.R., Elgaard, C., Easson, W.J. & Greated, C.A. (1993) *The Application of PIV to Turbulent Two-phase Flows.* In *Flow Visualization and Image Analysis* Ed. F.T.M. Nieuwstadt. Kluwer Academic Publishers, Dordrecht, The Netherlands.

61. Mizuguchi, M. (1986) *Experimental Study on Kinematics and Dynamics of Wave Breaking.* Proc. Int. Conf. Coastal Eng., 45:589-603.

62. Moraitis, C.S. (1988) *Optical Processing.* Proc. 5th Lecture Series on Particle Image Displacement Velocimetry, von Karmen Inst. for Fluid Dynamics, Belgium.

63. Morrison, I.G. & Greated, C.A. (1992) *Oscillating Water Column Modelling.* Proc. Int. Conf. Coastal Eng., 37:502-511.

64. Nairn, R.B. & Southgate, H. (1993) *Deterministic Profile Modelling of Nearshore Processes. Part 2. Sediment Transport and Beach Profile Development.* Coastal Engineering 19:57-96.

65. Nielsen, P. (1992) *Coastal Bottom Boundary Layers and Sediment Transport.* World Scientific, Singapore.

66. Nielsen, P. (1994) *Suspended Particle Motion in Coastal Flows.* Proc. 24th Int. Conf. Coastal Eng., Kobe, Japan.

67. Nieuwstadt, F.T.M. (ed) (1993) *Flow Visualization and Image Analysis* Kluwer Academic Publishers, Dordrecht, The Netherlands.

68. Pedersen, C., Deigaard, R., Fredsoe, J. & Hansen, E.A. (1992) *Numerical Simulation of Sand in Plunging Breakers.* Proc. Int. Conf. Coastal Eng., 180:2344-2357.

69. Peregrine, D.H. (1967) *Long Waves on a Beach.* J. Fluid Mech., 27:815-827.

70. Peregrine, D.H. & Svendsen, I.A. (1978) *Spilling Breakers, Bores and Hydraulic Jumps.* Proc. Int. Conf. Coastal Eng., 540-550.

71. Peregrine, D.H. (1983) *Breaking Waves on Beaches.* Ann. Rev. Fluid Mech., 15:149-78.

72. Petti, M., Quinn, P.A., Liberatore, G. & Greated, C.A. (1994) *Wave Velocity Field Measurements over a Submerged Breakwater.* Proc. Int. Conf. Coastal Eng., Kobe, Japan.

73. Powell, K.A. (1988) *The Dynamic Response of Shingle Beaches to Random Waves.* Proc. Int. Conf. Coastal Eng., 130:1763-1773.

74. Powell, K.A., Quinn, P.A. & Greated, C.A. (1992) *Shingle Beach Profiles and Wave Kinematics* Proc. Int. Conf. Coastal Eng., 181:2358-2369.

75. Quinn, P.A., Skyner, D.J., Gray, C., Greated, C.A. & Easson, W.J. (1993) *A Critical Analysis of the Particle Image Velocimetry Technique as Applied to Water Waves.* in *Flow Visualization and Image Analysis* Ed. F.T.M. Nieuwstadt. Kluwer Academic Publishers, Dordrecht, The Netherlands.

76. Quinn, P.A., Petti, M., Drago, M. & Greated, C.A. (1994) *Velocity Field Measurements and Theoretical Comparisons for Non-Linear Waves on Mild Slopes.* Proc. Int. Conf. Coastal Eng., Kobe, Japan.

77. Rapp, R.J. & Melville, W.K. (1990) *Laboratory Measurements of Deep-water Breaking Waves.* Phil. Trans. R. Soc. Lond. A 331:735-800.

78. Rienecker, M.M. & Fenton, J.D. (1981) *A Fourier Approximation Method for Steady Water Waves.* J. Fluid Mech., 104:119-137.

79. Roelvink, J.A. (1993) *Surf Beat and its effect on Cross-shore Profiles.* PhD Thesis. Technical University of Delft, The Netherlands.

80. Roelvink, J.A., & Stive, M.J.F. (1989) *Bar-Generating Cross-Shore Flow Mechanisms on a Beach.* J. Geophys. Res., 94:C4:4785-4800.

81. Roelvink, J.A., Petit, H.A.H. & Kostense, J.K. (1992) *Verification of a 1-D Surfbeat Model Against Laboratory Data.* Proc. Int. Conf. Coastal Eng., 72:960-973.

82. Sakai, S., Hirayama, K. & Saeki, H. (1988) *A new Parameter for Wave Breaking with Opposing Current on a Sloping Sea Bed.* Proc. Int. Conf. Coastal Eng., 77:1035-1044.

83. Salter, S.H. (1982) *Absorbing Wave Makers and Wide Tanks.* Proc. Directional Wave Spectra Applications, ASCE, 185-200.

84. Sarpkaya, T. & Isaacson, M. (1981) *Mechanics of Wave Forces on Offshore Structures.* Published by Van Nostrand Reinhold Company, New York. ISBN 0-442-25402-4.

85. Schwartz, L.W. (1974) *Computer Extension and Analytic Continuation of Stoke's Expansion for gravity Waves.* J. Geophys. Res., 63:553-578.

86. Simons, R.R., Grass, A.J. & Mansour-Tehrani, M. (1992) *Bottom Shear Stresses in the Boundary Layers Under Waves and Currents Crossing at Right Angles.* Proc. Int. Conf. Coastal Eng., 45:604-617.

87. Sinha, S.K. (1988) *Improving the Accuracy and Resolution of Particle Image or Laser Speckle Velocimetry.* Experiments in Fluids, 6:67-68.

88. Skyner, D.J., Gray, C. & Greated, C.A. (1990) *A Comparison of Time-stepping Numerical Predictions with Whole-Field Flow Measurement in Breaking Waves.* In *Water Wave Kinematics*, pp491-508, A.Torum & O.T. Gudmestad (Eds), Kluwer Academic Publishers, The Netherlands.

89. Skyner, D.J. (1992) *The Mechanics of Extreme Water Waves.* PhD Thesis, The University of Edinburgh.

90. Skyner, D.J. & Easson, W.J. (1992) *The Effect of Sheared Currents on Wave Kinematics and Surface Parameters.* Proc. Int. Conf. Coastal Eng., 46:618-629.

91. Sleath, J.F.A. (1987) *Turbulent Oscillatory Flow over Rough Beds.* J. Fluid Mech., 182:369-409.

92. Sleath, J.F.A. (1990) *Sea Bed Boundary Layers.* In *The Sea,* Vol. 9; Ocean Engineering Science. Le Mehaute, B. & Hanes, D.M. (Eds.) Wiley, New York.

93. Sleath, J.F.A. (1991) *Velocities and Shear Stresses in Wave-Current Flows.* J. Geophys. Res., 96 (C8): 15237-15244.

94. Southgate, H. & Nairn, R.B. (1993) *Deterministic Profile Modelling of Nearshore Processes. Part 1. Waves and Currents.* Coastal Engineering 19:27-56.

95. Stive, M.J.F. (1980) *Velocity and Pressure Fields of Spilling Breakers.* Proc. Int. Conf. Coastal Eng., 34:547-566.

96. Stive, M.J.F. & Wind, H.G. (1982) *A Study of Radiation Stress and Set-up in the Nearshore Region.* Coastal Eng., 6:1-25.

97. Stive, M.J.F., DeVriend, H.J., Nicholls, R.J. & Capobianco, M. (1992) *Shore Nourishment and the Active Zone: A Time Scale Dependent View.* Proc. Int. Conf. Coastal Eng., 189:2464-2473.

98. Su, C.H. & Gardner, C.S. (1968) *Derivation of the Korteweg- de Vries Equations and Burgers Equations.* Journal of Mathematical Physics, Vol 10:3.

99. Svendsen, I.A., Madsen, P.A. & Hansen, J.B. (1978) *Wave Characteristics in the Surf Zone* Proc. Int. Conf. Coastal Eng., 520-539.

100. Svendsen, I.A. & Jonsson, I.G. (1980) *Hydrodynamics of Coastal Regions* Pubs. Den Private Ingeniorfond, Technical University of Denmark, DK-2800, Lyngby.

101. Swan, C. (1990) *An Experimental Study of Waves on a Strongly Sheared Profile.* Proc. Int. Conf. Coastal Eng., pp 489-502.

102. Swan, C. (1992) *A Stream Function Solution for Waves on a Strongly Sheared Current.* Proc. Int. Conf. Coastal Eng., 51:684-697.

103. Thomas, G.P. (1990) *Wave-Current Interactions: an Experimental and Numerical Study, Part 2: Non-Linear Waves.* J. Fluid Mech., 216:505-536.

104. Thornton, E.B. & Guza, R.T. (1983) *Transformation of Wave Height Distribution.* J. Geophys. Res., 88:C10:5925-5938.

105. Tucker, M.J. (1963) *Analysis of records of Sea Waves.* Proc. Inst. Civil Eng. 26:305-316.

106. Van Rijn, L.C. & Kroon, A. (1992) *Sediment Transport by Currents and Waves.* Proc. Int. Conf. Coastal Eng., 200:2613-2629.

107. Villaret, C. & Latteux, B. (1992) *Entrainment and Transport of Fine Sand by Combined Waves and Current: An Experimental Study.* Proc. Int. Conf. Coastal Eng., 192:2500-2512.

108. Vinje, T. & Brevig, P. (1981) *Breaking Waves on Finite Water Depths.* Ship Res. Inst. of Norway, Report R-111.81.

109. Watson, G. & Peregrine, D.H. (1992) *Low Frequency Waves in the Surf Zone.* Proc. Int. Conf. Coastal Eng., 61:818-831.

110. Watson, G., Barnes, T.C.D. & Peregrine, D.H. (1994) *The Generation of Low Frequency Waves by a Single Wave Group Incident on a Beach.* Proc. EC MAST G8-M Workshop, Gregynog, Wales.

111. Wang, J.D. & LeMehaute, B. (1980) *Breaking Wave Characteristics on a Plane Beach.* Coastal Engineering, 4:137-149.

112. Yariv, A. (1985) *Optical Electronics* Publs. Holt-Saunders International.

Appendix A

List of Publications

Refereed papers

1. Quinn, P.A., Skyner, D.J., Gray, C., Greated, C.A. and Easson, W.J. (1993) *A Critical Analysis of the Particle Image Velocimetry technique as applied to Water Waves.* In **Flow Visualization and Image Analysis**, Ed. F.T.M. Nieuwstadt. Kluwer Academic Publishers, Dordrecht, The Netherlands.

Conference Papers: Refereed abstracts

1. Powell, K.A., Quinn, P.A. & Greated, C.A., *Shingle Beach Profiles and Wave Kinematics.* 1992. Proc. 23rd Int. Conf. Coastal Eng. 181:2358-2369.

2. Quinn, P.A., Petti, M., Drago, M. & Greated, C.A. *Velocity Field Measurements and Theoretical Comparisons for Non-linear Waves on Gentle Slopes.* Proc. 24th Int. Conf. Coastal Eng., Kobe, Japan.

3. Petti, M., Quinn, P.A., Liberatore, G. & Easson, W.J. (1994) *Wave Velocity Field Measurements over a Submerged Breakwater.* Proc. 24th Int. Conf. Coastal Eng., Kobe, Japan.

4. Quinn, P.A., Barnes, T., Lloyd, S.T., Greated, C.A. & Peregrine, D.H. (1995) *Velocity Measurements of Post-Breaking Turbulence Generated by Breaking Waves.* Accepted for presentation at Coastal Dynamics '95, Gdansk, Poland.

Workshop Proceedings: Extended abstracts

1. Greated, C.A., Quinn, P.A. & Easson, W.J. (1991) *The Measurement of the Velocity Field of Breaking Waves on a Plane 1:30 Beach, Using Particle Image Velocimetry.* Proc. EC-MAST G6-M Mid-term Workshop, Edinburgh, UK.

2. Greated, C.A., Easson, W.J., Quinn, P.A., Skyner, D.J. & She, K. (1992) *Velocity Measurements Under 2-D and 3-D Breaking Waves Using Particle Image Velocimetry.* Proc. EC-MAST G6-M Final Workshop, Pisa, Italy.

3. Quinn, P.A., Petti, M., Greated, C.A., Aminti, P., Liberatore, G. & Easson, W.J. (1993) *Wave Measurements on a 1:100 Beach.* Proc. EC-MAST G8-M Annual Workshop, Grenoble, France.

4. Earnshaw, H.C., Greated, C.A., Easson, W.J. & Quinn, P.A. (1993) *PIV Measurement of Oscillatory Flow over a Rippled Bed.* Proc. EC-MAST G8-M Annual Workshop, Grenoble, France.

5. Quinn, P.A., Petti, M., Drago, M. & Greated, C.A. (1994) *Velocity Field Measurements and Theoretical Comparisons for Non-Linear Waves on Mild Slopes* Proc. EC-MAST G8-M Annual Workshop, Gregynog, Wales.

6. Petti, M., Quinn, P.A., Liberatore, G. & Easson, W.J. (1994) *Wave Velocity Field Measurements over a Submerged Breakwater.* Proc. EC-MAST G8-M Annual Workshop, Gregynog, Wales.

7. Quinn, P.A., Lloyd, S.T., Greated, C.A. & Easson, W.J. (1994) *Velocity and Vorticity Measurements in Deep Water Plunging Breakers.* Proc. EC-MAST G8-M Annual Workshop, Gregynog, Wales.